Experimental investigation into the flow characteristics of a stationary blown heavy-duty cylinder head

Verdaasdonk, P.

Award date:
2011

P. Verdaasdonk
Augustus 2011

Experimental investigation into the flow characteristics of a stationary blown heavy-duty cylinder head

P. Verdaasdonk

Graduation Thesis
WVT 2011.09

Supervisors:
R.P.C. Zegers Msc.
Dr. ir. L.M.T. Somers

Professor:
Prof. dr. L.P.H. de Goey

Technical University Eindhoven
Fac. Mechanical Engineering
Division Thermo Fluids Engineering
Section Combustion Technology

August 25, 2011

Abstract

Premixed Charge Combustion Ignition (PCCI) promises good prospects for cleaner diesel combustion. PCCI is based on the idea of early diesel injection during the compression stroke. This early injection, allows for better mixing between the diesel and entrained air, creating more homogeneous and leaner mixtures. These lean homogeneous mixtures produce less harmful emission such as NO_x and particle matter during combustion.

To increase the mixing between the early injected fuel and entrained air, in-cylinder flow structures are of importance. Intake manifolds are designed to create a rotational motion of the air charge around an axis parallel to the cylinder axis (swirl) and/or a rotational motion around an axis normal to the perpendicular the cylinder (tumble).

To investigate the in-cylinder flow structures a flowbench setup was constructed, which is a stationary blown Proteus cylinder-head with a glass dummy-cylinder and cyclone mounted on top. This glass dummy-cylinder allows for Particle Image Velocimetry measurements (PIV) to visualize the flow structures present.

The flowbench is capable of providing engine intake flows and pressures. The setup is adequate to perform stationary flowbench test. All parts are modular to allow for easy access and maintenance. The subframe allows for easy removal of the cylinder-head. The modularity allows for other cylinder-heads to easily be installed. Although the setup was build to obtain PIV data, pressure drop over the cylinder-head, absolute pressure in the tubing and mass flow are also measured. The flows and pressures can easily be tuned manually.

The dummy-cylinder and glass window in the cyclone allow for PIV measurements inside the dummy-cylinder (axial and tangential). An incorporated optical inlet tube should allow for flow visualization in the inlet tubing.

A seeding device has been constructed to seed the flow with DEHS particles. The particles were illuminated using a 10 Hz Quantel Twins BSL50 laser with 50 mJ pulse energy. The PIV images were obtained with a Kodak Megaplus 1.0 CCD camera with a resolution of 1008 x1018 pixels and a Nikon AF-Nikkor 50mm 1:1.4D lens.

The data was correlated using PIVview software and the obtained velocity data was exported for further analysis in MATLAB. Although a very stringent outlier definition was applied to the data, on average 10% of the obtained vectors were rejected. Average velocity fields were constructed for the various measurement points as well as Reynolds decompositions and instantaneous fields. The obtained data was used to calculate the normalized fluctuations, normalized turbulent kinetic energies and angular velocities. These variables gave more insight in the actual flow structures present in the cylinder at valve-lifts under investigation. A proper orthogonal decomposition was preformed on the data to visualize different structures within the flow. These new results give an increased understanding of the in-cylinder flows and can be used for future CFD validation.

Samenvatting

Premixed Charge Combustion Ignition (PCCI) belooft goede vooruitzichten voor schonere verbranding. PCCI is gebaseerd op het idee van vroege diesel injectie tijdens de compressie slag. Deze vroege injectie zorgt voor een betere vermenging van de diesel en de lucht in de cilinder, wat leidt tot meer homogene en armere mengsels. Deze meer homogene en armere mengsels leiden tot afname van schadelijke emissies zoals NO_x en roet, die ontstaan tijdens de verbranding. Om de vermenging van brandstof en lucht te verhogen zijn lucht-stromingen in de cilinder van belang. Inlaat-stukken worden ontworpen om een draaiende beweging te genereren rondom een as parallel aan de cilinder-as (swirl) of loodrecht daarop (tumble).

Een blaas-opstelling is ontworpen om deze lucht-stromingen te onderzoeken. Deze blaas-opstelling is in feite een Proteus cilinderkop met daarop een glazen buis (als cilinder) en een afvang-cycloon gemonteerd. Door deze glazen buis kunnen Particle Image Velocimetry (PIV) metingen worden gedaan aan de lucht-stromingen die aanwezig zijn in de cilinder.

De blaas-opstelling kan motor-stromingen en drukken nabootsen. De opstelling is geschikt om stationair doorgeblazen experimenten uit te voeren. Alle delen van de opstelling zijn modulair, wat zorgt voor makkelijke toegang en onderhoud. Het subframe zorgt ervoor dat de cilinderkop makkelijk verwijderd kan worden. De modulariteit van de opstelling zorgt er ook voor dat andere cilinderkoppen makkelijk kunnen worden bevestigd. Hoewel deze opstelling gebouwd is voor PIV metingen worden ook de drukval over de cilinderkop, de absolute druk in het inlaatkanaal en de luchtmassastroom gemeten. De stromingen en drukken zijn eenvoudig handmatig te wijzen.

De glazen buis en het glazen raam in de afvangcycloon, maken het mogelijk om zowel axiale als tangentile PIV metingen te doen in de cilinder. Een optische toegankelijk inlaatstuk geeft de mogelijkheid om de inlaatstroming in de aanvoerbuis te meten.

Een deeltjes-generator is gebouwd om DEHS deeltjes toe te voegen aan de stroming. Deze deeltjes zijn belicht met een 10 Hz Quantel Twins BSL50 laser met 50 mJ pulse energie. De PIV plaatjes zijn verkregen met een Kodak Megaplus 1.0 CCD camera met een resolutie van 1008 x1018 pixels en een Nikon AF-Nikkor 50mm 1:1.4D lens.

De data verkregen is gecorreleerd met PIVview software en de daaruit verkregen vectoren zijn verder verwerkt met MATLAB. Ondanks een erg strenge outlier-detectie werd gemiddeld maar 10% van de vectoren afgekeurd. Gemiddelde snelheidsvelden zijn verkregen voor verschillende meetpunten, evenals instantane velden en Reynolds decomposities. De verkregen data is gebruikt om genormaliseerde schommelingen in de stroming te berekenen evenals genormaliseerde turbulente kinetisch energien en hoeksnelheden. Deze variabelen geven meer inzicht in de stromingen die aanwezig zijn in de cilinder. Een Proper Orthogonal Decomposition (POD) is toegepast op de data om de verschillende structuren in de stroming te visualiseren. Deze nieuwe resultaten geven een betere begrip van de in-cilinder stromingen en kunnen gebruikt worden voor toekomstige CFD validatie.

Contents

Chapter 1

Introduction

The most efficient internal combustion engine (ICE), to power road-vehicles is the diesel engine. Hence most heavy duty vehicles, like trucks, ships and trains, are equipped with diesel engines. The drawback of this engine is their harmful emissions like particle matter (PM) or soot and nitrogen oxides (NO_x). PM and NO_x are very unhealthy to humans and nature. Governments are therefore actively regulating the emissions of PM and NO_x. These restrictions are major impediments to diesel engines meeting future emissions standards and are the focus of extensive current research.

The main problem in assuring cleaner emissions lies within the working principle of a diesel engine. The engine works by the compression ignition method, meaning that air is entrained in the cylinder, during the compression stroke this air is compressed by the piston. When the piston reaches Top Dead Center (TDC), diesel is injected. Due to the high temperature and pressure of the compressed air inside the cylinder the diesel spray will ignite instantly, and combustion is achieved. The problem with this type of combustion is the lack of premixing between the diesel and air. When the spray is injected near TDC it penetrates the air and slightly later it burns from the outside inwards by diffusional combustion as seen in picture 1.1. This type of combustion produces numerous soot particles, since the fuel is not able to burn conventionally due to the locally shortcoming of oxygen. High combustion-temperatures inside the cylinder result in nitrogen oxides formation.

There are two ways to deal with this problem, the first being after-treatment systems like the Diesel Particle Filter (DPF) which is installed in many trucks at the moment. This filter retains the soot particles emitted by the engine. To deal with the nitrogen oxides a selective catalytic reduction (SCR) is implemented. This is chemical process which takes place inside to the exhaust pipe to rid the exhaust gasses of NO_x. While these systems are currently used, they are very complex systems and are very costly to implement.

Emissions can also be reduced by altering the combustion process itself. Exhaust Gas Recirculation (EGR) is currently used, to lower the combustion temperature inside the cylinder and thus reduce the emissions of NO_x. Although EGR reduces NO_x emissions it has the tendency to increase soot emissions [18] [27]. These problems could be solved by a new combustion process currently researched. This combustion process, Premixed Charge Compression Ignition (PCCI), has the potential to combine low emissions with high efficiency.

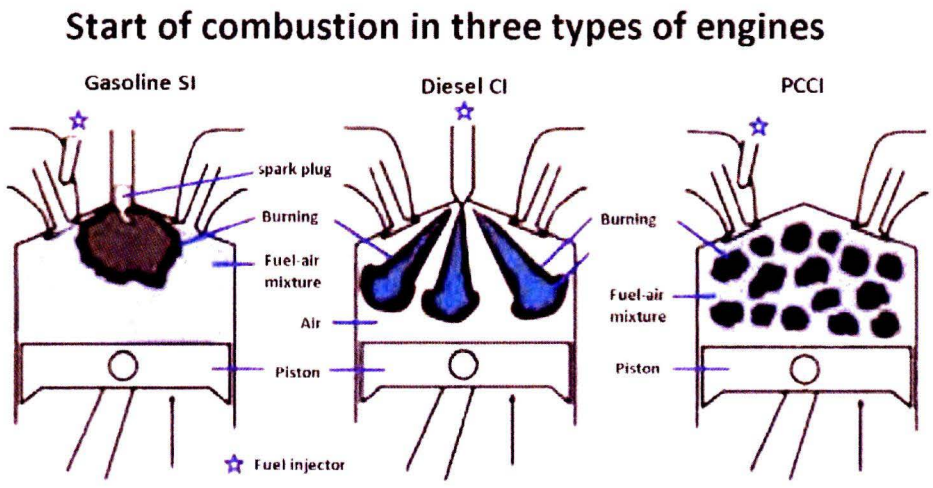

Figure 1.1: Schematic illustration of SI, CI and PCCI combustion [35]

1.1 Premixed Charge Compression Ignition

The basic difference between a gasoline engine and a diesel engine, lies in their combustion processes. In a gasoline engine the fuel and air is premixed in the intake manifold before it enters the cylinder. Inside the cylinder the charge is compressed and finally ignited by a sparkplug, as can been seen in picture 1.1. This type of combustion is know as Spark Ignition (SI) combustion. SI engines tend to have less particle matter emissions due to the good premixing of air and fuel, which starts in the intake manifold. The mixture prior to combustion inside a SI engine is more or less homogenous.

In a diesel engine the charge is self-ignited by the pressure and temperature near TDC, this is known as compression-ignition (CI). This method does not allow for any premixing between the diesel and air, and thus gives rise to harmfully emissions like soot.

Premixes Charge Compression Ignition (PCCI) of Homogenous Charge Compression Ignition (HCCI) as it is sometimes referred too, combines the combustion processes of both SI and CI-engines. By injecting diesel early in the compression stroke the diesel has time to mix with the air present in the cylinder. During compression the pressure will rise till it reaches the ignition pressure for diesel, at which point the diesel will ignite. Ideally the ignition of the mixture starts multiple spots (or instantaneously) over the entire mixture, so no (or less) propagation of the flame front is needed. Figure 1.1 illustrates this process. Most importantly the diesel and air should be mixed homogenously in order to obtain homogenously combustion of the charge over the cylinder, resulting in complete combustion of the diesel and a significantly reduction in soot emissions. PCCI engines can have efficiencies as high as compression-ignition, direct-injection (CIDI) engines (an advanced version of the commonly known diesel engine), while producing ultra-low emissions nitrogen oxides (NO_x) and particulate matter (Soot). PCCI engines can operate on gasoline, diesel fuel, and most alternative fuels [11].

1.1.1 Advantages of PCCI combustion

PCCI combustion has several advantages over conventional engines. Relative to SI gasoline engines, PCCI engines are more efficient than SI engines, approaching the efficiency of a CIDI engine. This improved efficiency results from three sources[11]:

- **The elimination of throttling losses**, SI engines are regulated by a throttle valve which induces losses, PCCI engines work by limiting the amount of fuel injected.
- **The use of high compression ratios**, similar to a CIDI engine.
- **Shorter combustion duration**, since it is not necessary for a flame to propagate across the cylinder. Combustion starts at multiple point, instead of centrally at the spark-plug.

PCCI engines have lower engine-out NO_x than SI engines, although the overall emissions NO_x emissions of SI engine vehicle are lower, since SI-engines allow for a three-way catalysts in the tailpipe to remove NO_x from the exhaust gasses.

Relative to CIDI engines, PCCI engines have substantially lower emissions of soot and NO_x this is a result of the dilute homogeneous air and fuel mixture in addition to low combustion temperatures [11]. The charge in an PCCI engine can be made dilute using excess air, Exhaust Gas Recirculation (EGR) or a combination. Because the mixture will auto-ignite, flame propagation is not required and thus dilution levels of the mixture can be much higher than the levels tolerated by either SI or CIDI engines. In a PCCI engine, the mixture will start to ignite when the temperature is around 800 to 1000 K (depending on the type of fuel). During combustion this temperature will rise but complete combustion can be achieved at temperature below those at which significant NO_x are produced [11]. In contrast, in CIDI engines, minimum flame temperatures are 1900 to 2100 K, high enough to make unacceptable levels of NO_x [14]. Additionally, the combustion duration in PCCI engines is much shorter than in CIDI engines since it is not limited by the rate of fuel/air mixing [11]. The mixing takes place during compression of the mixture. This shorter combustion duration gives the PCCI engine an additional efficiency advantage.

Finally, PCCI engines may be more economical to produce than current CI engines since they would likely use lower-pressure fuel-injection equipment and require a less complex and rigorous emission control system. Current CI engine use high-pressure injection systems such as common-rail diesel injection to obtain better air-fuel mixing.

However for PCCI to work, the mixing between fuel and air during compression needs to be optimized. A promising solution is to use in-cylinder air structures to enhance the mixing. Therefore engineers are trying to visualize and optimize the airflow into the cylinder as well as injection timings and techniques to optimize PCCI combustion.

1.2 In-cylinder air structures

Heavy-duty diesel engines are usually turbocharged, this implicates that the air is slightly pressurized when it enters the cylinder through the intake manifold and intake runners. The intake manifold and in particular the intake runners are designed to give the air a certain momentum and direction upon entering the cylinder. Three main in-cylinder air structures are of importance.

Swirl is the organized rotation of the air charge about the cylinder axis or an axis parallel to this axis. Swirl is created by directing the intake flow into the cylinder with an initial angular momentum [18]. This momentum is created by the mold of the intake runners. While some decay in swirl occurs during the engine cycle, due to friction with the cylinder wall, the intake generated swirl usually persists throughout the compression, combustion and expansion processes [18]. A graphical representation of swirl is given in picture 1.2 .

Squish is the motion of air which is generated when the upwards moving piston reaches the cylinder head towards the end of the compression stroke. Air is forced into the bowl-in-piston chamber. Squish enhances the swirl during compression since the angular momentum is conserved, and as the moment of inertia of the air is decreased its angular velocity must increase [18] [46]. A graphical representation of squish is given in picture 1.3.

Tumble is the motion which is induced the air moves over the valve. Basically the valve is an obstruction in the intake stream, air collides with the valve and tumbles into the cylinder. Tumble is produced in the early stage of the compression stroke and distorted in the late stage of the stroke [30]. A graphical representation of tumble is given in picture 1.4 .

Of these three structures swirl and tumble can be altered by the intake manifold setup. Both swirl and tumble can store kinetic energy during the intake and compression strokes and the energy is converted into turbulence near top dead center; thus, faster burning can be achieved from the higher turbulence levels [44]. Though it is clear that the primary effect of swirl and tumble on combustion rate is due to turbulence enhancement, the quantitative relationship between the two is not easy to establish because of the difficulties of quantifying the transient rotational mean motion and especially of evaluating turbulence intensity within the cylinder [19]. However, velocity field measurements and numerical simulations both show rapid decay of tumbling motion accompanied by significant turbulence enhancement before

Figure 1.2: Swirl

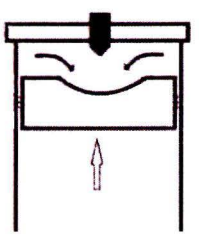

Figure 1.3: Squish

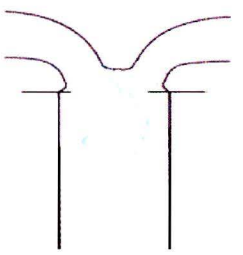

Figure 1.4: Tumble

TDC. According to Heywood, tumble vortices persist until about the end of the intake stroke and then become unstable and break down into three-dimensional turbulent motions [18]. In general, with both swirl and tumble, turbulence tends to be roughly homogeneous and isotropic near TDC [19]. Fluctuation near TDC could be increased by 25-50% due to swirl or tumble, their combined effects not being simply additive[19] [31].

Around TDC swirl is the most dominant air structure [18] [29]. Swirl can significantly increase mixing between fuel and air during compression. This in turn can lead to a reduced burning period and increased thermal efficiency. The swirl (possibly in combination with squish) can be particularly important for combustion of lean mixtures. Lean mixtures reduces the combustion temperature and thus the NO_x emissions. In general swirl improves flame propagation speed, reduce cyclic variations, and expand the lean limit, though excessive rotational motion can have deleterious effects on induction system flow resistance and also on heat transfer and thermal efficiency [19].

1.3 Test methods

Currently car and truck manufactures tune their intake runners to obtain good in-cylinder swirl. The problem manufactures face is how to test there cylinder heads for swirl. This is usually done in a so called flowbench [28] [51], which is basically a setup in which a cylinder-head is stationary blown through with air. The cylinder-head is usually provided with pressurized air, and a dummy cylinder, usually just a tube with the same internal diameter as the bore, is positioned on the cylinder head. A light-weight paddle wheel is positioned inside this dummy cylinder, pivoted on the centerline (with low friction bearings), mounted between 1 and 1.75 bore diameters down the dummy cylinder [18] as in figure 1.5. The rotation rate of the paddle wheel is used as a measure of the air swirl. Since this rotation rate depends on the location of the wheel and its design, and the details of the swirling flow, many manufactures

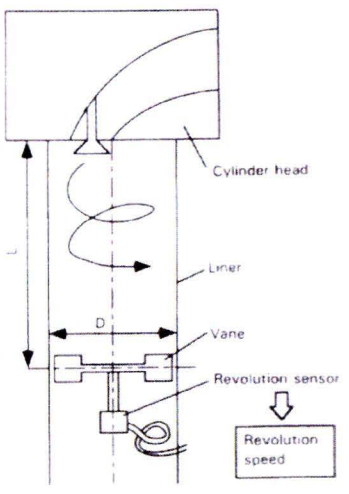

Figure 1.5: Paddle wheel method [25]

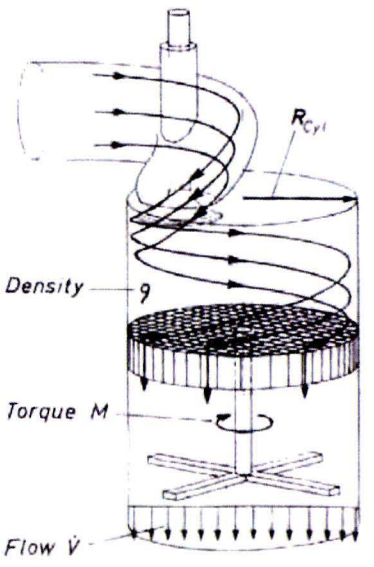

Figure 1.6: Swirl impuls method [45]

(Jaguar....etc) replaced this technique by the impulse swirl meter illustrated in figure 1.6. A honeycomb flow straightener replaces the paddle wheel: it measures the total torque exerted by the swirling flow [18].

Both of these measurement devices give an indication of the swirl, either in the form of a rotational speed or in the form of a torque. Although these measurement-methods are used throughout the industry, they lack to visualize the actual swirl present and, instead give a number corresponding to the momentum which the swirl is exerting. Swirl is a highly fluctuating phenomena both in time as in position in the cylinder. These methods lack the possibility to show these variation in swirls. These methods can only be used on an already manufactured cylinder head therefore the cylinder head can only be tuned for swirl by trail and error[46].

A more sophisticated model to analyse swirl is being investigated. The field of Computational Fluid Dynamics (CFD) offers very promising prospects to visualize swirl inside cylinders without manufacturing a cylinder head and testing it in a flowbench. CFD solves the Navier Stokes equations for a given flow problem. In order to solve these calculations certain boundary conditions are needed as well as reference measurements to validate the model. These reference measurements should visualize the actual behavior of the in-cylinder swirl as function of different variables (such as: valve lift, distance from the cylinder head and pressure difference over the valves). CFD has the potential to significantly reduce the research costs of cylinder heads and can improve the understanding of the intake-runner-swirl correlation, providing engineers the possibility to determine swirl ratios prior to manufacturing.

1.4 Focus of this report

In this project a stationary flowbench is build to investigate the in-cylinder flow as a function of distance from the cylinder head and valve-lift. The flow will be measured by Particle Image Velocimetry (PIV) in order to visualize the "smaller" structures inside the cylinder. The overall goal is to obtain an accurate swirl velocity field in order to be used as a benchmark in a yet to be developed CFD model of the cylinder head. The goal for this specific project is to obtain sufficient qualitative data to support the developed CFD model.

First this report will discuss the theory used to develop a flowbench and important variables used in these measurements. Secondly the theory behind swirl will be elaborated, key variables will be introduced and equations will be presented to estimate the swirl numbers. This will be followed by general theory on PIV together with the requirements to obtain qualitatively good results. It will also elaborate the software used to analyse the PIV images.

The following chapter will be devoted to the build test setup and the different design considerations that were deliberated, as well as the choices that were made during the PIV analyse. After this elaboration of the setup, problems that arose during the measurements will be discussed followed by the results and analyzes. Finally conclusions will be drawn and recommendations will be presented for future participants in this research.

Chapter 2

Theory

Flow field visualization has developed over the last few decades, mainly due to the rise of high power laser technology. In times prior to laser technology flow field visualization was mainly done by intrusive measurement devices, such as hot-wire anemometry. The main drawback of these intrusive methods is, that a measuring device needs to be probed inside the flow, thus disturbing the flow. This can lead to inaccurate flow measurements. Besides this problem, intrusive measurements usually only measure locally at the position of the probe.
Laser technology allows for non-intrusive measurement methods, such as Laser Doppler Anemometry (LDA), Particle Tracking Velocimetry (PTV) and Particle Image Velocimetry (PIV). These methods have the advantage that the do not disturb and are therefore more likely to produce more accurate measurements. Besides LDA, these techniques are able to visualize bigger volumes of the flow.

In this research the PIV approach was chosen to characterize the in-cylinder swirl motion. This was mainly done due to the nature of the flow investigated. Swirl is highly turbulent two-dimensional flow pattern that will occur perpendicular to the flow inside a cylinder. In case of turbulent flows, a whole spectrum of eddies occur with maximum dimensions related to the flow domain and minimum dimensions in the order of a few millimeters for laboratorium experiments. In order to observe these large ranges of eddy sizes, a high particle density is needed. This means that it is impossible to track the individual particles. Therefore, the mean displacement of particles in a small region of the image(s) (the interrogation area) has to be calculated, leading this research to the PIV approach.

This chapter will start by explaining how stationary flowbench setup are usually constructed and what important variables can be extracted. It will elaborate the swirl motion and give key variables to indicate this swirl as well as length scales used to range the eddies produced by the swirl. Furthermore it will explain the working principles of PIV and the considerations that need to made during flow field visualization using PIV software.

2.1 Flowbench measurements

A flowbench measurement currently is the most practical way of determining the flow-characteristics of any given cylinder head. The industry has implemented the flowbench measurement, to analyse their cylinder heads and compare them to each other. A flowbench setup operates without a moving piston, instead a dummy-cylinder is positioned to allow free flow of the air. At the exit of the dummy-cylinder a swirl measuring device is positioned to measure the swirl produced. A typical flowbench is depicted in figure 2.1

During Flowbench measurements, the valve is usually set at a certain valve-lift. Normally the pressure-drop over the cylinder head is kept constant, and the combination of pressure-drop and valve-lift produce a mass flow of air. Although it also possible to operate the flowbench with a set mass flow, and to measure the pressure-drop.

Historically two types of flowbench measurements were developed the AVL-method and the Ricardo-method. The main difference between these techniques lies within the operating principle. Ricardo considers the intake process to start at Intake Valve Opening (IVO) and end at Intake Valve Closing (IVC) and the total intake flow quantity is dependent of cam profile and valve open duration. AVL on the other hand assumes that the intake process takes place only between Top Dead Center (TDC) and Bottom Dead Center (BDC) for 180 crank angle degrees and the instantaneous flow velocity in the valve gaps is proportional to the instantaneous piston speed. AVL defines a 'standard lift curve' for the flow parameter integration. Therefore, a simple conversion between the Ricardo and AVL flow parameters is not possible. Furthermore Ricardo uses a blowing flowbench where air is blown through the cylinder head by a blower, whereas AVL uses a suction pump downstream of the dummy-cylinder, to suck through the cylinder head as summarized by Xu [51]. In this report the Ricardo method is used.

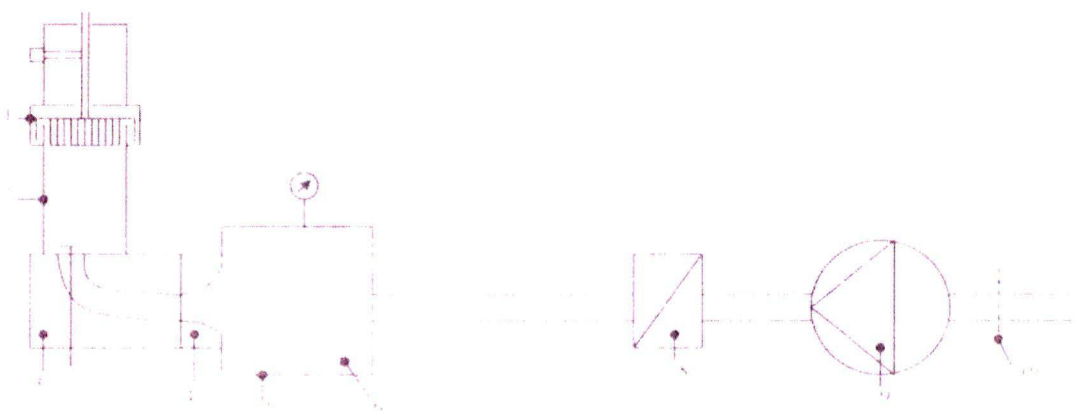

Figure 2.1: Stationary flowbench according to Ricardo [8], swirl-impuls-meter (1), dummy-cylinder (2), cylinder head (3), transition (4), air-tank (5), turbulence-filter (6), pressure-gauge (7), flow-measurement (8), blower (9), air-filter(10)

2.1.1 Pressure-drop

An important parameter in the Ricardo flowbench measurement is the pressure-difference (Δp) over the cylinder head. This Δp is defined as the difference between the pressure inside the intake-manifold and the pressure inside the dummy-cylinder. Although this Δp is freely to be chosen, Ricardo does dictate a Δp of 254 mm water column (2.5 kPa) to allow comparison between the different measurements. This Δp is chosen to assure fully turbulent flow in the intake-manifold so that the loss of velocity head is independent of the pressure drop or flow rate. In that case the swirl-properties are also independent of the used pressure-drop. To assure this fully turbulent flow in the intake, Xu [51] defines three different Reynolds-numbers:

$$Re_d = \frac{\rho \cdot V_d \cdot D}{\mu} \qquad \text{Reynolds-number in inner-seat} \qquad [-] \tag{2.1}$$

$$Re_L = \frac{\rho \cdot V_v \cdot L}{\mu} \qquad \text{Reynolds-number in valve-gap} \qquad [-] \tag{2.2}$$

$$Re_B = \frac{\rho \cdot V_c \cdot B}{\mu} \qquad \text{Reynolds-number in cylinder} \qquad [-] \tag{2.3}$$

Equation 2.2 is the smallest of the three equations stated above and, thus determines the pressure-drop which needs to be used. Partington [34] reports that the non-dimensional properties of the engine port flow become substantially independent of the pressure drop when the port Reynolds-number (Re_L) exceed 60.000 at low valve lifts and 90.000 at high valve lifts. Xu [51] on the other hand states that the Reynolds-number in the valve-gap (Re_L) should at least be 10.000. In most cases a Δp of 2.5 kPa is sufficient for these numbers. However experience showed that flow-properties become independent of pressure-drop, at a pressure drop of 10 kPa [8]. To allow comparison between measurements in literature and the measurements of this report the Δp in this report has been set at 10 kPa.

2.1.2 Flow-coefficients

A basic requirement of the port and valve assembly design is to enable the engine to have high volumetric efficiency (in the order of 90% for naturally aspirated diesel engines [18]) for achieving high torque and power. During the early stage of engine development, the performance of the port/valve assembly in terms of the air flow capacity is usually assessed under steady flow test conditions, using the ratio of the measured mass flow rate to the theoretically calculated flow rate through a reference flow area in the port/valve assembly.

If the flow is considered to be incompressible and isentropic, the theoretic velocity (V_{th}) which the flow should have after leaving the valve passage can be determined by equation 2.4. Note that after this passage the flow reaches the atmospheric end-pressure, assuming that the dummy-cylinder is connected to the atmospheric surroundings.

$$V_{th} = \sqrt{\frac{2 \cdot \Delta p}{\rho}}, \qquad \left[\frac{m}{s}\right] \tag{2.4}$$

where ρ is the density of air in the intake which can be determined with equation 2.5.

$$\rho_{in} = 1.293 \cdot \frac{T_{ref}}{T + T_{ref}} \cdot \frac{P}{P_{ref}}, \qquad \left[\frac{kg}{m^3}\right] \tag{2.5}$$

in this equation the reference-conditions are set at 273 K and 1013.25 mBar. Based on V_{th}, the flow area A and the density ρ_{in} the theoretical mass flow $\dot{m}_{th}$ through the reference passage can be determined by equation 2.6.

$$\dot{m}_{th} = \sqrt{\frac{2 \cdot \Delta p}{\rho}} \cdot \rho_{in} \cdot A \qquad \left[\frac{kg}{s}\right] \tag{2.6}$$

The real mass flow $\dot{m}$ is lower than the theoretical mass flow $\dot{m}_{th}$ due to compressibility-effects, the imperfect geometry of the intake manifold and the presence of valves. Using this mass flow, several key variables (explained in the following subsections) can be introduced. These variables scale the real and theoretic mass flow by the fraction $\frac{\dot{m}}{\dot{m}_{th}}$ and therefore to what extent the actual flow approaches the theoretical flow.

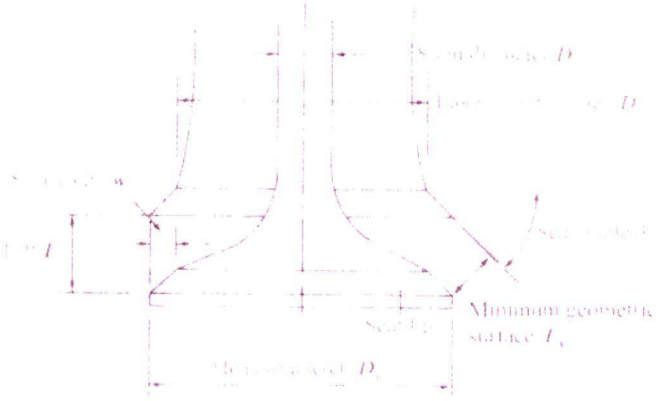

Figure 2.2: Scheme of valve geometry for calculating mean geometric area [18]

Flow coefficient C_F

The flow coefficient C_F, which increases with valve lift, reflects the restriction by the port geometry, when the gap area between the valve and seat lips becomes comparable to or beyond the port throat area. Since a large proportion of charge enters the cylinder at higher valve lifts, the influence of the flow coefficient to the engine breathing capacity is more important.

The flow coefficient, C_F, corresponds to the flow area in the port, either the minimum geometric area (port throat) or the valve inner seat area, in which the valve stem blocking effect can be included or neglected. Xu [51] chooses this flow area A as the inside of the valve-seat (inner-seat diameter D), as shown in figure 2.2. This flow area is independent of the valve-lift L, the area can be determined by equation 2.7.

$$A = n \cdot \frac{\pi}{4} \cdot D^2, \qquad [m^2] \tag{2.7}$$

with n the number of valves. The flow coefficient can accordingly be determined by equation 2.8.

$$C_F = \frac{\dot{m}}{A \cdot V_{th} \cdot \rho}. \qquad [-] \tag{2.8}$$

Using C_f only, however, will not reflect clearly the difference in the flow capacity at smaller valve lifts simply because the scale of C_f at low valve lift is too small. Therefore another coefficient is introduced the discharge coefficient C_D

Discharge coefficient C_D

The discharge coefficient C_D, which decreases with valve lift, reflects the flow restriction produced by the valve and seat lips at low valve lifts which then determine the flow orifice area. In fact, the geometry of valve and seat lip are critical to the flow at lower valve lifts [51] [18].

To determine the discharge coefficient C_D, the passage of the valve gap is set as the reference surface. However this surface is ambiguous. Partington [34] defines the reference surface as:

$$A_V = n \cdot \pi \cdot D^2 \cdot \cos\beta \left[1 + \frac{L}{D} \cdot \sin\beta \cos\beta\right] \cdot \frac{L}{D}. \qquad [m^2] \qquad (2.9)$$

Equation 2.9 represents the minimum geometric surface with dimension L_V, taking into account the seat angle β. Also used is:

$$A_P = n \cdot \pi \cdot D \cdot L. \qquad [m^2] \qquad (2.10)$$

In equation 2.11 the passage is modeled as a cylinder with diameter D and height L. Surface A_P is also referred to as the valve curtain. The discharge coefficient can be determined by:

$$C_D = \frac{\dot{m}}{A \cdot V_{th} \cdot \rho}, \qquad [-] \qquad (2.11)$$

with A either A_V or A_P.

2.1.3 Compressibility effects

The methods for characterizing the intake flow under steady flow conditions are based on a basic assumption that the flow is incompressible because the flow velocity in the port is relatively low and the pressure drop is relatively small. Note that in the steady flow test, when the Reynolds number or pressure drop increases, errors in the measured static flow coefficient due to the assumption of incompressible flow also increase. Using the calculations of compressible flow the error can be estimated [51]. At 10 kPa of pressure drop the speed V_{th} is 128 $\frac{m}{s}$ or Mach 0.37. Equation 2.12 describes the theoretical mass flow through a passage accounting for compressibility effects [51] [48].

$$\dot{m}_{th} = A \cdot p_{in} \sqrt{\frac{2 \cdot \gamma}{R \cdot T_{in} \cdot (\gamma - 1)} \cdot \left[\left(\frac{1}{\gamma}\right)^{\frac{2}{\gamma}} - \left(\frac{1}{\gamma}\right)^{\frac{\gamma+1}{\gamma}}\right]}. \qquad \left[\frac{kg}{s}\right] \qquad (2.12)$$

With this mass flow $\dot{m}_{th}$ a flow coefficient can be expressed according to:

$$C_F = \frac{\dot{m}}{\dot{m}_{th}}. \qquad [-] \qquad (2.13)$$

In equation 2.12 γ can be replaced by 1.4, since the medium used in the flowbench is air. Accordingly when the small difference between stagnation temperature and ambient temperature are neglected, it appears that the theoretical mass flow is overestimated by 4.5% [51]. Therefore the flow- and discharge coefficient will be underestimated by 4.5%.

2.2 Swirl characteristics

Cylinder heads and intake manifold are specifically designed to increase the swirling motion of the intake air. The importance of port design and to some extend the general lack of understanding its operation. is reflected by the multiplicity of different configurations which have been employed throughout the history of intake-manifold design. A few of them are sketched in figure 2.3 Figure 2.3a shows the simplest possible arrangement. which is axisymmetric and

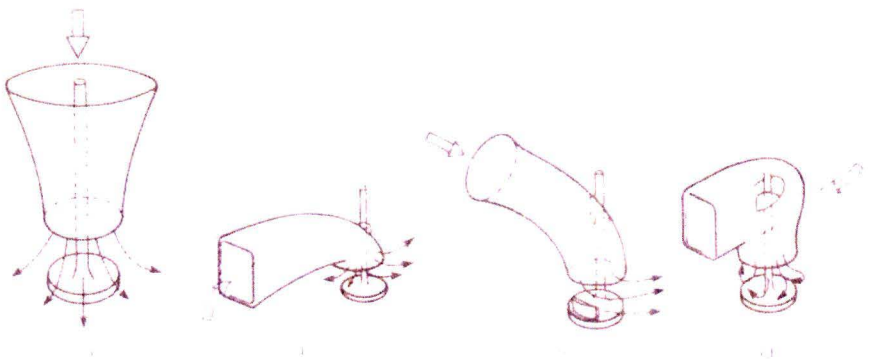

Figure 2.3: Illustrations of typical inlet port designs. (a) idealized axisymmetric port, (b) directed or tangential port. (c) deflector or shrouded valve, (d) helical port [22].

consist of a valve in the coaxial passage; the passage may contain vanes to impart rotation to the incoming flow. sometimes termed *pre-swirl*[22]. This is scarcely a practical design, although it is sometimes approached in racing engines.

Figure 2.3b. shows are more practical design. the directed or tangential ports which have curved passages of generally variable and non-circular section, although without protuberances apart from the valve guide. Their main feature is that they are deliberately arranged to cause the flow to exit non-uniformly from the valve orifice in preferred directions[22]. The experimental Proteus cylinder-head used in this research is equipped with tangential intake ports as can been seen in figure 2.4.

The configuration shown in figure 2.3c resembles a tangential port but it has a deflector or shroud embodies either to the exit of the port or on the valve itself. again this is designed to impart a preferential direction to the outgoing flow [22]. The concept of the valve shroud is very useful for research or development purposes because it is easy to implement. but in practical applications it suffers from excessive pressure losses (reduced volumetric efficiency) at high flow rates associated with higher engine speeds. and from the need to retain the valve from rotation.

Finally figure 2.3d is a representative of the helical class of ports. differing from the directed design in having a helical trough cast into the inner surface. the function of which is to provoke rotation about the cylinder axis [22]. The flow performance of the helical intake port has great influence on Dl diesel engine combustion and performance and so the helical port is usually an important. well-designed and sophisticated engine part [39]. A great advantage of helical ports is that the need for the relatively long straight section in the directional port is

obviated and it is sometimes preferred in situations where the directional port, which if fairly shallow, would interfere with the head cooling passages [46] The drawback this design is that many errors or deviations may occur during the casting and machining processes, which can lead to severe deviations in produced swirl [39].

2.2.1 Proteus Cylinder head

The Proteus cylinder head is designed with tangential inlet runners, which are oriented in the same direction, meaning the channels both contribute to establishing a swirl motion inside the cylinder. Shroudless valves are installed in the cylinder head, so the swirl is generated by the intake runners only. Figure 2.4 shows how the tangential intake runners are casted within the cylinder head.

Figure 2.4: Section (from the valves inwards) of the Proteus cylinder head with the position of the dummy-cylinder indicated in yellow and the air flow direction indicated in red.

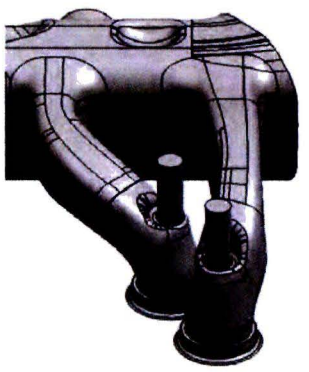

Figure 2.5: Cast of the Proteus intake manifold for one cylinder

The flow generated by this intake manifold is complex. Initially the flow will be directed into the cylinder. Figure 2.5 shows steep bend just before the valves. This bend is incorporated in the design to accommodate for the valves. This bend guides the intake air over the valves into the cylinder creating in-cylinder air structures. As the air is guided over the valves it is likely that a jet will appear in the valve passage, this jet will directed into the cylinder, but still have a tangential component imposed by the tangential port. Therefore at some distance from the cylinder head, this jet will collide with the cylinder wall and cause a global rotation (swirl) around an axial axis within the cylinder. The jet in the valve passage might also experience tumble as a result of the geometry of the valve passage and the valve design.

The three-dimensional in-cylinder flow pattern, the degree of swirl and tumble, largely depends on the mass flow of air and the valve lift. In general the swirl center does not line up with the center of the cylinder and varies in time and position from the cylinder head. At low valve lifts and mass flows the impuls of the jet is insufficient to create global rotations and the flow pattern is complex. At a large enough distance from the cylinder head though, the

flow will become one-dimensional again, due to dissipation of the swirl and tumble vortexes.

2.2.2 Analysis of Swirl patterns

Evaluating swirl or tumble strength in engine cylinders is far more difficult than assessing the engine breathing capacity. The main issues concerned are the techniques for measuring the flow, and the method to calculate the data, which involves the definitions of Swirl Ratio' and 'Tumble Ratio. The process to define the tumble ratio is actually 'borrowed' from the conventional way of defining the swirl ratio [51].

The most often used swirl parameter is the engine swirl ratio, which has been broadly defined as:

$$R_s = \frac{\text{Charge vortex rotation speed}\,(\omega_s)}{\text{Engine speed}\,(\frac{\pi \cdot N}{30})}, \qquad [-] \qquad (2.14)$$

Where N is the crankshaft revolution speed in Revolution Per Minute (RPM).

Under steady flow test conditions, the charge vortex rotation speed is commonly calculated assuming that the charge motion is a solid-body rotating flow which, at the end of induction process, has momentum equal to the sum of the angular momentum introduced during the whole induction process. The swirl ratio is calculated by integrating the rig or stationary swirl numbers (N_{sr}) as a function of crank angle during the induction process and then divided by the fictitious engine speed. Omitting the derivation of the equations, the Ricardo Swirl Ratio (R_{SR}) is:

$$R_{SR} = \frac{tangentialswirlvelocity}{idealvelocity} = \frac{B \cdot S}{n \cdot D^2} \cdot \frac{\int_{\alpha 2}^{\alpha 1} C_F \cdot N_{SR} d\alpha}{\left(\int_{\alpha 2}^{\alpha 1} C_F \cdot d\alpha\right)^2} \qquad [-] \qquad (2.15)$$

Where $\alpha 1$ and $\alpha 2$ are the inlet valve open and close position crack angles respectively and N_{SR} is the Rig Swirl Number defined as:

$$N_{sr} = \frac{8}{\dot{m} \cdot B \cdot V_{th}} \cdot \dot{I}. \qquad [-] \qquad (2.16)$$

The swirling flow is normally characterized by the moment of angular momentum about a chosen axis. The angular momentum flux in the engine cylinder, $\dot{I}$, is a function of crank angle during the induction process. In the steady flow test, it is a function of valve lift for a given flow rate or pressure drop. The linear ratio of this angular momentum flux to the fictitious engine speed corresponding to the test condition is called the Rig Swirl Number (N_{sr}) in the Ricardo system [51].

In equation 2.16 the angular momentum flux is still unknown. To determine the angular momentum flux, $\dot{I}$, the derivative of the inertia of the air mass is needed. Equation 2.18 gives the relation for the derivative of the solid-body inertia.

$$\dot{J} = \frac{1}{2} \cdot \dot{m} \cdot r^2 \qquad \left[\frac{kg \cdot m^2}{s}\right] \qquad (2.17)$$

The angular momentum flux, $\dot{I}$ correlates to equation 2.18 by:

$$\dot{I} = \dot{J} \cdot \omega. \qquad [Nm] \qquad (2.18)$$

Determining the angular momentum flux in the actual flow is less easy. For each axial position z a integral will have to be solved across the cylinder surface. Equation 2.19 shows this integral [45].

$$\dot{I} = \int_0^{2\pi} \int_0^r \rho \cdot V_{tan} \cdot V_{ax} \cdot r^2 \cdot dr \cdot d\phi \qquad [Nm] \qquad (2.19)$$

In equation 2.19 the axial and tangential velocities are still unknown, however the solid-body assumption implies that the tangential velocity of the flow is proportional to the radius of the flow eddy [6] according to equation 2.20 [45].

$$V_{tan} = \omega \cdot r. \qquad \left[\frac{m}{s}\right] \qquad (2.20)$$

The axial velocity is defined by equation 2.21 [6].

$$V_{ax} = \frac{4 \cdot \dot{m}}{\rho \cdot \pi \cdot B^2} \qquad \left[\frac{m}{s}\right] \qquad (2.21)$$

So if it possible to determine the tangential velocity component for each axial z position over all valve lift during IVO and IVC, one is able to calculate the corresponding Ricardo Swirl Ratio (R_{SR}). Corresponding measurements have been done at the flowbench in literature and data is available.

2.3 Particle Image Velocimetry

Particle Image Velocimetry (PIV) is a flow visualization technique which yields a two dimensional flow field of a given area of interest. PIV works by adding small particles (seeding) to the liquid or gaseous flow of interest (figure 2.6). These particles are carefully chosen to follow the flow they are seeded into perfectly. PIV works as follows:

- Two separate laser pulses are generated and are passed through lenses which converts the pulses into a two dimensional sheet.
- The seeded particles pass through these laser sheet and scatter light.
- A camera, which is synchronized with the laser records these scattering particles onto two separate frames.
- The two frames are divided into interrogation areas
- The interrogation areas of the two frames are digitally compared with each other, using a correlation-function, and small displacements between the two images are identified.
- A reference grid and the timing between the two consecutive frames provide the data to determine the velocity vector between two separate interrogation areas and a velocity field can be constructed by assembling the individual velocity components per interrogation area.

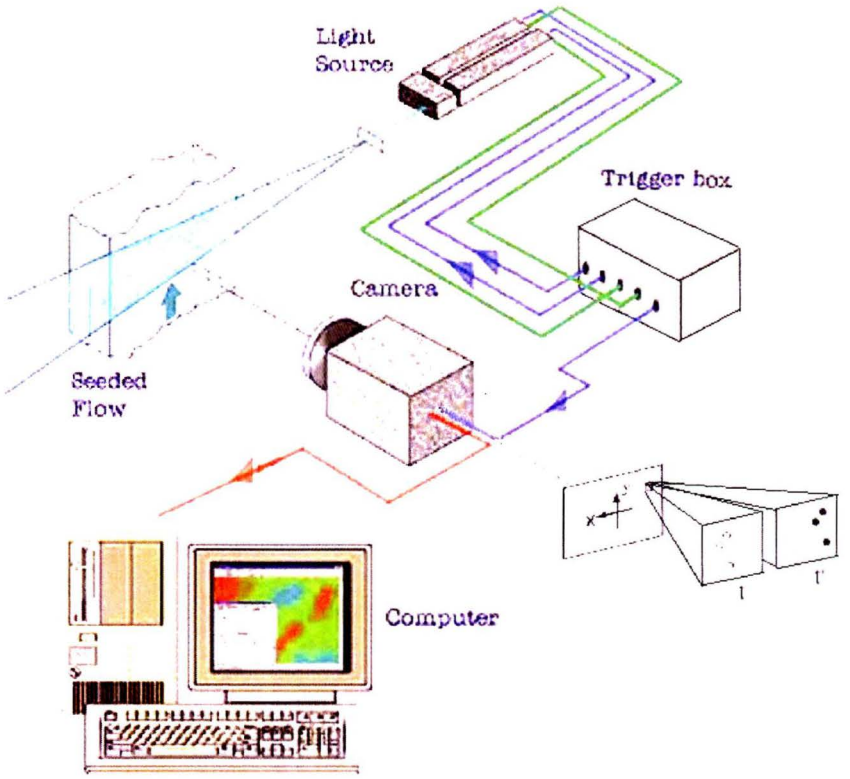

Figure 2.6: Graphical representation of Particle Image velocimetry [6]

In PIV measurements it is important to achieve small displacement of the particles to ensure accurate correlation of the interrogation areas by the correlation-function. The displacement of the particles should approximately by a quarter of the interrogation area. So in a 64 x 64 pixel interrogation area, particle-displacement may not exceed 16 pixels [2] [3].

Another frequently occurring problem is that in many in-cylinder measurements the out-of-plane velocity is higher than the in-plane velocity, resulting in the loss of particles over the two images. This is due to the thin laser-sheet in the out-of-plane direction to gain optimal light intensity, as can been seen in figure 2.6. To gain optimal result with PIV some conditions need to be met:

- An interrogation area chosen should at least contain 8 - 10 particles [5] [12]. This guarantees that at every interrogation area on the image plane there is a high probability of obtaining a velocity vector that represents the average motion of the particles in that spot [3], but not so high that the particles overlap to produce speckle.

- The timing chosen between the two laser pulses should be short enough for the particles to remain within the laser sheet [5] [12], thus reducing out-of-plane particle. Though the timing should be long enough to record displacement of particles between the two frames.

- The laser intensity should be high enough to gain enough scattering of the particles [38] to record frames with high a Signal-to-Noise-Ratio (SNR). Noise is present in the form of background light and other disturbances.
- The seeding should be carefully selected to obtain good flow tracking. This poses limitations to the weight and size of the chosen particles.

When these conditions are met, the PIV measurement is assumed to represent the flow characteristics at the region of interest. The PIV process is graphically expressed in figure 2.6.

2.4 Laser

The quality of PIV measurements depends, among other variables, on the laser used. To gain optimal PIV images, the laser source should have certain properties:

- A uniform beam profile so it can be shaped into a homogeneous 2D light sheet. Disturbances in the beam profile lead to disturbances in the light plane which can adversely affect the measurement [15] [23].
- High intensity to obtain enough particle scattering [38].
- The emitted light intensity should preferably be the same over the two consecutive frames to obtain optimal PIV results. In this way the scattering in both frames is identical which allows for better correlation [5].
- The two consecutive laser pulses need to be triggered, with little time between the them ($\sim$ 10 μs) [38].
- The light emitted source ideally be monochromatic with a wavelength in the visible spectrum in this way a regular camera can be used. Additionally monochromatic light implies that little light is lost when using optics, due to reflections (approximately 5% per lens).
- The repetition-rate of the laser should be reasonable, in order to do multiple measurements in a short time [38].
- The duration of laser pulse should be short enough to "freeze" the motion of the particles during the pulse exposure in order to avoid blurring of the image [38].

Although variety of lasers is available to meet the requirements above, a double-cavity Q-switched laser is the best choice for PIV measurements. Since this laser consists of two separate laser cavities, and can be externally triggered to shoot two consecutive laser pulses at any given interim between the pulses, although the repetition rate of the lasers might be low ($\sim$ 10 Hz). The Q-switch in these lasers allows for maximum charge of the laser medium and therefore the lasers are able to shoot at high intensities ($\sim$ 50 - 300 mJ per pulse). The pulses are produced in the order of 10 nanoseconds, which is enough to illuminate the particles, but still short enough to freeze the particles in a frame. The monochromatic nature of the laser implies little losses when using optics and allows for a regular camera to be used.

The laser beam exiting the laser is a two-dimensional round beam. This beam has to be converted into a two-dimensional laser sheet. For this conversion optics are needed. A spherical lens is placed in front of the beam to convert the beam to a point. Secondly, a negative cylindrical lens is used to stretch the sheet in one direction, thus creating a sheet (as can been seen in figure 2.7).

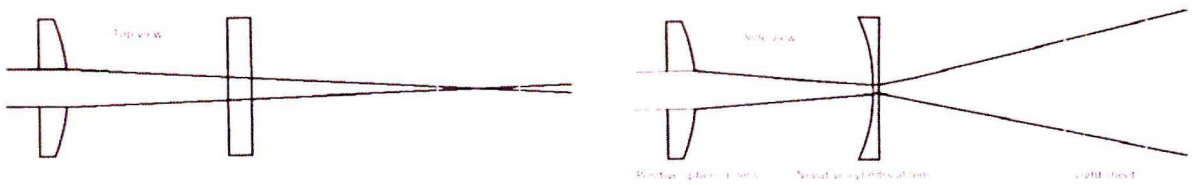

Figure 2.7: Creation of a light sheet by means of optics [47]

2.5 Seeding

One of the key components in PIV is the seeding particles. The technique depends heavily on the choice of the particles. These particles can be either solid particles or liquid droplets. Solid particles are difficult to disperse and tend to agglomerate while liquid droplets evaporate rather quickly [38]. In literature oil droplets are frequently used [24] [38] [26] these particles usually offer the advantage of not being toxic (depends on the sort of oil), they are able to stay in air at rest for hours and do not significantly change in size under various conditions [38].

Seeding oil droplets is usually done by atomization and condensation techniques. The challenge in seeding these particles is to obtain a homogeneous distribution of the particles within the airflow. This can be achieved by mixing using fluctuating or turbulent flows or by seeding the particles in several different places. The droplets are normally created by means of an aerosol generator which uses Lazkin nozzles, as shown in picture 2.8 and 2.9.

In the Laskin process compressed air flows through a submerged nozzle arrangement to create a high concentration of small liquid droplets in an polydisperse aerosol. The Laskin consists of a stainless steel tube with an outside diameter of 6 mm and an internal diameter of 4 mm. The end of this tube is plugged and four holes of 1 mm are drilled around the circumference just above this plug. The other end of the tube is connected to air-supply. Just above these holes a stainless steel disc is mounted around the tube as can been seen in figure 2.8 and 2.9. This disc contains four feed-holes located directly above the holes in the tube.

The Laskin Nozzle principle works as follows:
Compressed air if fed down a supply tube to four radial holes. Just above these holes a disc is secured with four adjacent holes above the air exits. The nozzle arrangement is immersed in the fluid to be nebulised. As the compressed air flows at high velocity out of the radial holes, oil is drawn in to the airflow and effectively atomized into the small air bubbles created, which then grow and move to the surface of the liquid where they burst, therefore releasing the generated particles they contain into the air above the liquid [13]. The over-pressure created in the unit vessel create an air outflow in which the atomized particles are entrained.

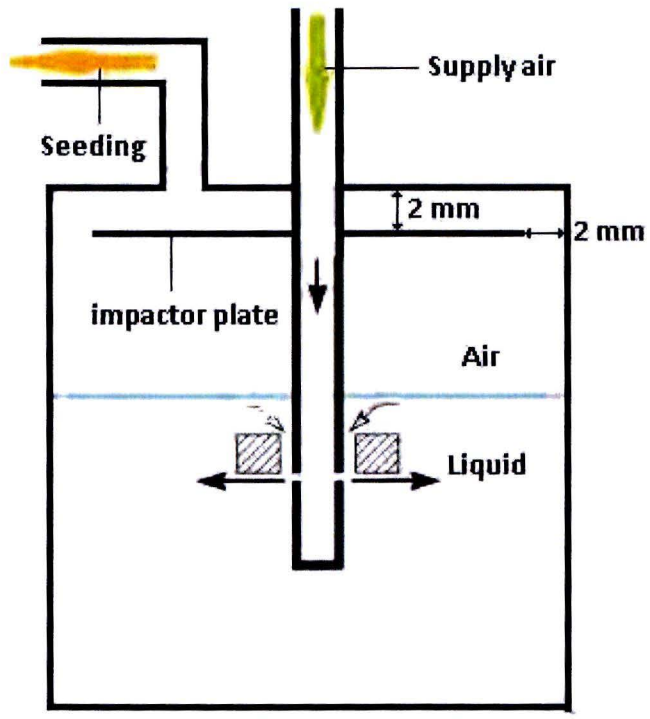

Figure 2.8: Schematic of a Laskin nozzle

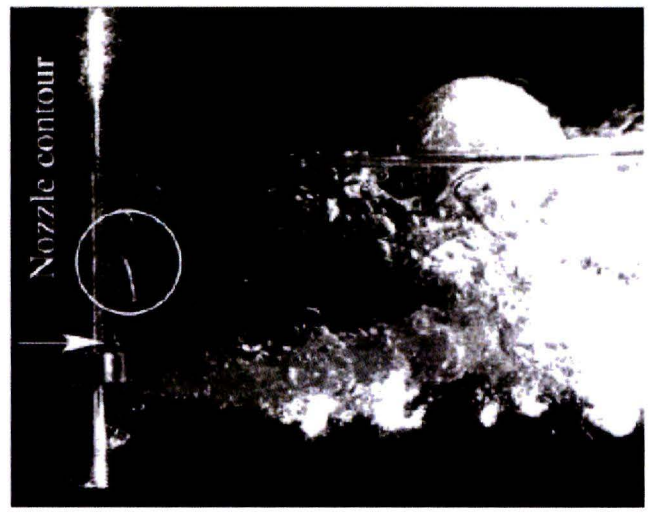

Figure 2.9: Visualization of an air jet emerging from a Laskin nozzle. The white circle and arrow indicate rising bubbles emerging from the liquid feed holes [24]

Just below the exit an impactor plate can be installed to retain the bigger particles. This impactor plate is a round stainless steel disc which leaves a gap of about 2 mm for the flow to exit.

The process is quite aggressive and aerosols with mean particle diameters in the range of 0.4 - 1.5 can be generated. To create larger mass flows multiple nozzles are required. Variations in air-supply pressure can allow for lower mass flows, these can be obtained by using a reducer [13].

2.5.1 Fluid Mechanical Properties

Ideally the density of the particles ρ_p would be the same as the density of the fluid under investigation ρ_f, in this way the influence of gravitational forces can be neglected. However this is seldom the case, since the density of fluids and gases tend to differ. The following characteristics of particles mainly depends on particle-mass, shape and dimensions. In order to investigate the following behavior of a particle the forces upon this particle need to be analyzed.

In general the forces exhibited on a particle in a cylinder head swirl are gravitational forces ($\vec{F}_g$) and frictional forces ($\vec{F}_w$) which are defined by:

$$\vec{F}_g = (\rho_p - \rho_f) \cdot \frac{\pi \cdot {d_p}^3}{6} \cdot \vec{g}. \qquad [N] \qquad (2.22)$$

$$\vec{F}_w = k \cdot (\vec{U}_p - \vec{U}_f), \qquad [N] \qquad (2.23)$$

$$\text{with } k = 3 \cdot \pi \cdot \mu \cdot d_p, \qquad \left[\frac{kg}{s}\right]$$

where d_p is the diameter of the particle, $\vec{g}$ is the gradational constant, μ is the dynamic viscosity of the fluid, $\vec{U}_p$ is the particle velocity, $\vec{U}_f$ is the fluid velocity and k is the viscous-drag-coefficient of a sphere in a Stokes flow. It is legitimate to use the Stokes approximation if spherical particles are observed in a viscous fluid at a very low Reynolds number.
Another important force in which is induced by swirl is the centripetal force, which is characterized by:

$$\vec{F}_c = (\rho_p - \rho_f) \cdot \frac{\pi \cdot {d_p}^3}{6} \cdot \omega^2 \cdot r. \qquad [N] \qquad (2.24)$$

The gravitational force and the centripetal force both scale with ${d_p}^3$, while the "driving" force ($\vec{F}_w$) in this motion scales only with d_p as can been seen from equations 2.22, 2.23 and 2.24. This imposes a limitation to the dimensions of the seeding particles used in PIV measurements and thus also to the mass of the particle [8].
The gravitational induced velocity U_g can be deduced from equation 2.22 and 2.23:

$$\vec{U}_g = (\rho_p - \rho_f) \cdot \frac{{d_p}^2}{18 \cdot \mu} \cdot \vec{g} \qquad \left[\frac{m}{s}\right] \qquad (2.25)$$

In analogy to equation 2.25, an estimate can be derived for the velocity lag of a particle in a continuously accelerating fluid:

$$\vec{U}_s = (\vec{U}_p - \vec{U}_f) = {d_p}^2 \cdot \frac{(\rho_p - \rho_f)}{18 \cdot \mu} \qquad \left[\frac{m}{s}\right] \qquad (2.26)$$

The step response of U_p typically follows an exponential curve if the particle density is much greater than the fluid density ($\rho_p \gg \rho_f$) [38]:

$$\vec{U}_p(t) = \vec{U}_f \left[1 - \exp -(\frac{t}{\tau_s})\right] \qquad \left[\frac{m}{s}\right] \qquad (2.27)$$

with relaxing time τ_s given by [38]:

$$\tau_s = {d_p}^2 \cdot \frac{\rho_p}{18 \cdot \mu} \quad (\simeq \frac{d^2}{\nu}) \qquad [s] \qquad (2.28)$$

Analyzing equation 2.28 yields that if d_p decreases, the relaxation time decreases and therefore the exponential term in equation 2.27 will approach zero. Equation 2.27 can than be deduced to $\vec{U_p}(t) \approx \vec{U_f}(t)$. Thus smaller the smaller the diameter of the particle the better the following characteristics are irrespective of the density of the particle compared to the density of the fluid. Note that the equations above only apply for Stokes' drag, which implies that the particle Reynolds number is smaller than unity.
In this experiment turbulence will play an important role, the airflow is most likely to exit the valves very turbulent, thus local Reynolds numbers can be very high. Therefore another solution, which describes spherical particles in turbulent flow will be given.
In literature [20] equations can be found to describe turbulent flow tracking of a spherical particle. They assume shear effects and centrifugal forces to be negligible if the density ratio is large ($\rho_p \gg \rho_f$). They reduce the equation of motion by Basset [20] to a solution for the amplitude ratio of the instantaneous particle and fluid velocities:

$$\left|\frac{\hat{U}_p}{\hat{U}_f}\right| = \left(1 + \frac{{\omega_c}^2}{C^2}\right)^{-\frac{1}{2}}, \qquad [-] \qquad (2.29)$$

$$\text{with } \omega_c = 2 \cdot \pi \cdot f_c \qquad [N]$$

Where $\hat{U}_p$ and $\hat{U}_f$ are the instantaneous particle and fluid velocity, f_c is the highest turbulence frequency and C is the characteristic frequency of particle motion. For Stokes'resistance, C equals the inverse of the relaxation time τ_s [33]:

$$C = \frac{18\mu}{\rho_p \cdot {d_p}^2} = \frac{18 \cdot \omega \cdot \rho_f}{Sk^2 \cdot \rho_p}. \qquad \left[\frac{1}{s}\right] \qquad (2.30)$$

ω is the angular frequency of the turbulent motion in equation 2.30 and Sk is the Stokes number, a characteristic non-dimensional frequency of the particle response, which is expressed as:

$$Sk = \left(\frac{\omega}{\nu}\right)^{\frac{1}{2}} \cdot d_p. \qquad [-] \qquad (2.31)$$

In order to obtain good flow tracking, the optimal particle diameter (d_p) has to be chosen. Using the equations in this section the maximum particle diameter can be specified. According to [20] equation 2.29 is often equaled to a maximum of 0.99 as criterion. When equation 2.29 is rewritten this yields:

$$d_p \leq \sqrt{0.4082 \cdot \frac{\mu}{f_c \cdot \rho_p}}, \qquad [m] \qquad (2.32)$$

Were f_c is the highest turbulence frequency. Equation yields a result, the diameter of the particles used in PIV measurements should be smaller than the calculated value of d_p when these particles are going to be used in highly fluctuating flows.

Another problem with seeding occurs in boundary layers, which are always present in realistic flow. In these boundary layers particles tend to spin due to the velocity gradient, this spinning induces a lift-force. From the Kutta-joukowsky theorem it follows that the spinning particle experience a lift-force:

$$\vec{F}_y = -\rho \cdot U \cdot \Gamma, \qquad [N] \tag{2.33}$$

with U the flow velocity, y the direction normal to the flow and

$$\Gamma = \oint_S \vec{u} \cdot \vec{t} ds, \qquad \left[\frac{m^3}{s}\right] \tag{2.34}$$

the circulation around the particle, with S the particle perimeter and $\vec{t}$ the tangential velocity on this perimeter. From equation 2.33 an analysis of the particle dynamics in the boundary layer can be drawn. In 2D approximation to the physical boundary layer, the particle spins with an angular velocity

$$\omega = \frac{\Delta U}{R} = \frac{dU}{dy}, \qquad \left[\frac{m}{s}\right] \tag{2.35}$$

meaning the circulation equals

$$\Gamma = -\omega \cdot R \cdot 2 \cdot \pi \cdot R = \frac{1}{2} \cdot \pi {d_p}^2 \cdot \frac{dU}{dy}. \qquad \left[\frac{m^3}{s}\right] \tag{2.36}$$

This readily leads to

$$F_{y,2D} = \frac{1}{2} \cdot \rho \cdot \pi \cdot {d_p}^2 \cdot U \frac{dU}{dy}, \qquad [N] \tag{2.37}$$

as the corresponding 2D lift-force. The velocity gradient in the boundary layer is positive, implying a lift-force directed away from the wall. Equation 2.37 shows that the lift-force is strongly particle diameter depended. This force removes particles from the direct vicinity of the wall and thus creates a zone close to the wall were no particles are present. Visualization in boundary layers is thus only possible if the particles experience no-appreciable lift-force: equation 2.36 and 2.37 imply that such particles must be light and small [47].

2.5.2 Optical Properties

The light scattered by particles, under illumination, is a function of the ratio of the refractive index of the particle to that of the medium it is dispersed into, the particles' size, their shape and orientation. Furthermore, the light scattering also depends on polarization and observation angle [38].

Rayleigh scattering from particles is too weak for PIV. For spherical particles with diameter d_p, which is larger than the wavelength of the incident light λ, Mie's scattering theory can be applied [38], these conditions are typical for PIV measurements. In this theory the relation between intensity of incident light and the intensity of the scattered light is given by [47]:

$$I_s \propto {d_p}^6 \cdot I_o, \tag{2.38}$$

with I_s is the intensity of the scattered light and I_o is the intensity of the incident light. Equation 2.38 once again shows that d_p is the crucial parameter in choosing seeding particles. When the particle diameter becomes too large however, much larger than the wavelength of the incident light, diffuse scattering occurs. For diffuse scattering the effective surface of the particle determines the relation between incident and scattered light intensity [38]:

$$I_{diff} \propto {d_p}^2 \cdot I_o, \tag{2.39}$$

Equation 2.38 and 2.39 illustrate that small particles are preferred. Figure 2.10 shows that Mie' scattering is also depended on the observation angle. In most PIV setups, the camera is positioned at a 90 degree angle towards the laser sheet, resulting in reduced Mie' scattering.

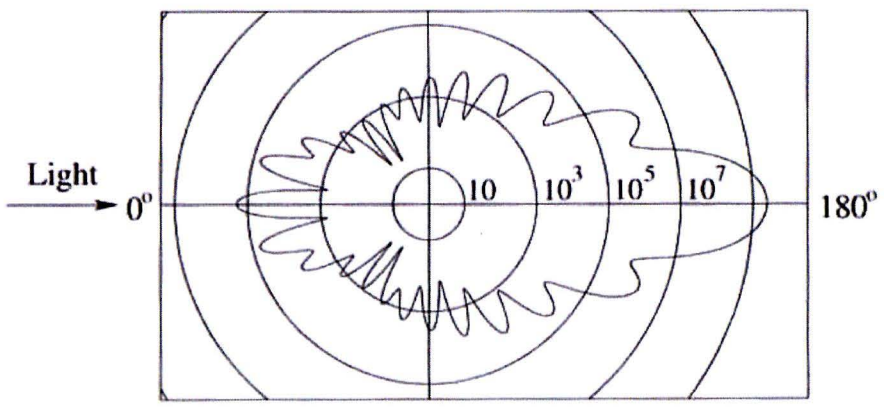

Figure 2.10: Light scattering of a 1 μm oil droplet in air, light intensity is given in logarithmic scale [38].

2.6 Camera

The camera plays an important role in PIV measurements. the camera provides the recorded images. from which the velocity profiles can be determined. PIV measurements definitely benefit from the technology of digital photography. Immediate image availability and thus feedback during recording as a complete avoidance of photochemical processing are a few of the apparent advantages brought with electronic imaging [38].

The most frequently used sensors in digital cameras is the Charge Coupled Device (CCD). When a photon enters a CCD sensor. this photon is converted to an electron. thus the CCD sensor converts light in to electric charge. These sensors are placed in an array of many individual CCD sensors. each sensor represents a pixel. and together these pixels form the total image displayed. The smaller the CCD sensors are. the more detail a picture can have. on the other hand the array of CCD sensors could also be extended in order to gain more detail. In general one can say. the more pixels a sensor has. the more detail it can display. Ideally a particle used in PIV should have the size of two pixels on the CCD array. This can either be done by carefully choosing the camera or by using lenses to enhance the picture before it reaches the CCD chip.

Over the past two decades. the CCD had found the most widespread use. However. rapid development of chip technology in the early 90s of the last century allowed manufacturing of Complementary Metal Oxide Semiconductor (CMOS) sensors with an improved SNR and resolution [38]. These State-of-the-art CMOS cameras have a good image quality. However. the image quality of state-of-the-art CCD cameras is still better. Thus. for high precision PIV measurements. which requires double frame cameras with high sensitivity and small pixels in order to avoid the peak-locking effect. a CCD camera should be applied [16]. To capture high speed events. a CMOS camera must be applied to get a sufficient frame rate[16].

The pixel size of the camera is also of importance. When the pixel size of the sensor is too large. it will be harder to distinguish the different particles and to meet the optimum criteria were 1 particle is depicted on about two pixels [38].

2.6.1 Diffraction Limited Imaging

Whenever plane light waves impinge on an opaque screen containing a circular aperture they generate a far-field diffraction pattern on a distant observing screen. By using a lens, for example an objective in a camera, the far field pattern can be imaged on an image sensor close to the aperture without changes [38]. However, if this image is a point, like the particles illuminated in PIV, the image does not appear as a point on the observing screen, but forms a circular diffraction pattern as seen in figure 2.11. These circular diffraction patterns are of interest since they represent the smallest particle image that can be obtained for a giving imaging configuration (camera and lenses). The diffraction limited minimum image diameter d_{dif} can be determined by:

$$d_{dif} = 2.44 \cdot F \cdot (M + 1) \cdot \lambda, \qquad [-] \qquad (2.40)$$

where F is the f-number of the lens, defined as the ratio between the focal length f and the aperture diameter D_a. In PIV, this minimum image diameter d_{dif} will only be obtained when recording small particles, of the order of a few microns, at small magnifications [38].
If lens aberrations can be neglected, the following equation can be used for an estimate of the particle image diameter d_τ:

$$d_\tau = \sqrt{(M \cdot d_p)^2 + d_{dif}^2}, \qquad [m] \qquad (2.41)$$

With equation 2.40 it is possible to estimate the depth of field of the image configuration:

$$\delta_Z = 2 \cdot F \cdot d_{dif} \cdot (M + 1)/M^2. \qquad [m] \qquad (2.42)$$

These aperture based properties can be used in PIV. Assuming that particle scattering is sufficient, the aperture diameter can be reduce in order to obtain more depth of field and a larger d_{diff}. This significantly enhances further PIV processing, since the particles tend to be depicted somewhat larger on the CCD camera and a thicker laser sheet (in the out-of-plane direction) can be used, reducing the loss of out-of-plane particles.

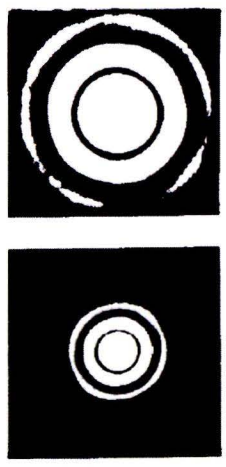

Figure 2.11: Airy patterns for a small (top) and larger aperture diameter (bottom) [38]

F	d_τ **[μm]**	δ_Z **[mm]**
1	1.387	0.648
1.4	1.941	0.907
2	2.772	1.296
2.8	3.881	1.815
4	5.544	2.592
5.6	7.761	3.629
8	11.087	5.185
11	15.244	7.129
16	22.173	10.370
22	30.487	14.258

Figure 2.12: Theoretical values for diffraction limited imaging of small particles ($\lambda = 532$ nm, M = $\left[\frac{1}{14.8}\right]$, $d_p = 1$ μm) [38]

2.7 Turbulence scales

The full complexity of in-cylinder flow can be characterized in terms of the average velocity U. the fluctuating velocity u. and the characteristic length or integral scale L.

To obtain the average velocity. the instantaneous velocity (U) is usually measured multiple times. These measurements are then averaged to obtain the average velocity. By subtracting the instantaneous velocities from the average velocity ($\bar{U}$) the fluctuating velocity is obtained (u) [44] . Equation 2.43 shows this relation, which is know as a Reynolds decomposition.

$$U = \bar{U} + u \qquad \left[\frac{m}{s}\right] \tag{2.43}$$

Similarly the turbulence intensity u' can be determined by:

$$u' = \sqrt{\frac{1}{N}\sum [U^2 - \bar{U}^2]} \qquad \left[\frac{m}{s}\right] \tag{2.44}$$

Where N is the number of times that the velocity is measured (number of measurements) Determining characteristic length L of the flow is considerably more difficult, since the velocity fluctuations in in-cylinder flows have a wide range of different length and time scales. In figure 2.13 this can be clearly seen, and represents the turbulent eddy structure prevailing in and around the jet-like flow issuing from the inlet valve during induction. A range of length scales is present. The largest eddies are those produced by the shearing action of the jet and have dimensions comparable or greater than the valve lift (within the jet) or valve diameter (in the surrounding fluid) [22]. These eddies are depicted as l in figure 2.13.
The integral length scale (l) of these large eddies is defined as the integral of the autocorrelation coefficient (R_x) of the fluctuating velocity at two adjacent points in the flow (R_x) with respect to a variable distance between the points and is a measure of the large scale structure of the flow field [44].

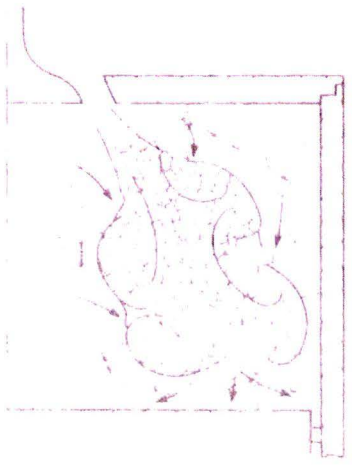

Figure 2.13: Turbulent eddy structure in the cylinder during induction [22]

$$l = \int_0^\infty R_x dx, \qquad [m] \qquad (2.45)$$

where

$$R_x = \frac{1}{N} \sum \frac{u(x_o) \cdot u(x)}{u'_0 \cdot u'_x}. \qquad [-] \qquad (2.46)$$

Adjacent to the integral scales a time scale was determined. The integral time scale of turbulence l_t is defined as a correlation between two velocities at a fixed point in space, but separated in time.

$$l_t = \int_0^\infty R_t dt, \qquad [s] \qquad (2.47)$$

where

$$R_t = \frac{1}{N} \sum \frac{u(\tau) \cdot u(\tau + 1)}{u'_\tau \cdot u'_{\tau+1}}, \qquad [-] \qquad (2.48)$$

However these large eddy are inherently unstable and break down in a cascade process to form ever smaller eddies. Finally they will dissipate in the thin shear layers interspersed throughout the flow in the form of spaghetti-like structures, due to viscous dissipation (as can been seen in figure 2.13).

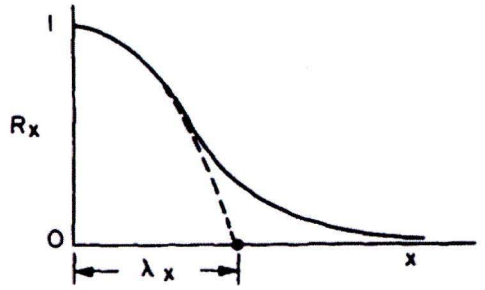

Figure 2.14: Variation of spatial correlation coefficient, with distance, and definitions of integral and micro length scales [22]

The Taylor microscale, indicated as λ in figure 2.13, is a measure for the distance between the smallest eddies or, equivalently, the magnitude of the turbulent strain field [22] [44]. The Taylor microscale is defined by the intercept with the abscissa of the parabola coinciding in level and curvature with the R_x function at x_0 i.e. as can been seen in figure 2.14. The corresponding length and time scales are:

$$\lambda = \frac{-2}{\left(\frac{\delta^2 \cdot R_x}{\delta x^2}\right)_{t=t_0}} \qquad [m] \qquad (2.49)$$

$$\lambda_t = \frac{-2}{\left(\frac{\delta^2 \cdot R_t}{\delta x^2}\right)_{t=t_0}} \qquad [s] \qquad (2.50)$$

Finally the smallest eddies, depicted as η in figure 2.13, are commonly referred to as the Kolmogorov microscale (ν) which, according to dimensional analysis, is related to the rate of turbulence dissipation per unit mass [22].

$$\eta = \left(\frac{\nu^3}{\epsilon}\right)^{\frac{1}{4}}, \qquad [m] \tag{2.51}$$

with ν, the kinematic viscosity of the gas. This quantity is of interest in connection with molecular mixing and reaction processes, which occur in the Kolmogorov eddies [22]. In engines η is in the order of 10 μm [32]. The turbulence dissipation or dissipation rate is defined formally as:

$$\epsilon = \nu \cdot \left(\frac{\delta \bar{u}_i}{\delta x_j}\frac{\delta \bar{u}_i}{\delta x_j}\right) \qquad \left[\frac{m^2}{s^3}\right] \tag{2.52}$$

The Kolmogorov time scale is defined as:

$$\eta_t = \left(\frac{\nu}{\epsilon}\right)^{\frac{1}{2}} \qquad [s] \tag{2.53}$$

It is a curious experimental fact that the amount of energy consumed in a fluctuating flow has nothing to do with the viscosity, but is determined entirely by the large turbulent scales (l). That is, the amount of energy taken from the average flow is determined by the process of creating the largest eddies [32]. This energy is passed on to the ever smaller eddies and finally dissipates by viscosity. If u is a turbulent velocity scale, the root mean square fluctuating velocity, and l is a length scale of the most energetic eddies, then it is an experimental fact that:

$$\epsilon = \frac{u^3}{l} \qquad \left[\frac{m^2}{s^3}\right] \tag{2.54}$$

In this case u can be calculated and l is defined as either the valve lift of valve diameter as stated before.

2.8 Correlation Techniques

In order to visualize the vector field with PIV, a correlation technique needs to be applied to the set of images. The images are divided into multiple interrogation areas and these are individually examined. In principle there are two correlation techniques which allow for this, auto-correlation and cross-correlation.

Auto-correlation is used whenever the two images are saved in one frame, this is a single photo frame which is illuminated twice. If correlation is applied to this picture three correlation peaks appear, the zero-displacement peak and two smaller displacement peaks, these peaks are equal in size, but not in direction. This technique allows for good correlation but is not capable of predicting the orientation of the flow. Especially in swirling flows this can cause problems.

Cross-correlation depends on two separate shot images, which are identified as being image one and two. The sequence of images is therefore fixed, and the correlation can now determine the displacement and direction of the particles. In this case only one correlation peak will appear and this will be the general displacement of the interrogation area. Cross-correlation is preferred if the camera has the option of shooting two separate image, due to the reliability of this technique.

Correlation is the most important step in the PIV process, however the total process can be divided in three clear steps: pre-processing, correlation and post-processing. These three steps and there importance will be briefly discussed.

2.8.1 Pre-processing

The final result of the PIV correlation process largely depends on the quality of the images used to correlate. The setup should be designed in such a way that the optimal pictures can be shot, however 100% clear pictures will never be obtained. Image pre-processing can be applied to achieve image contrast enhancement. The correlation scheme correlates pixels with the same intensity. Therefore brighter particles have more influence on the correlation peak than less bright particles. Imperfections in these correlation peaks can occur, when for instance the laser intensity between the two frames fluctuates or a reflection over-illuminates certain parts of the measurement area. These effects can impose negative outcomes since the correlation algorithm. The correlation algorithm will always correlate, but the question remains if the outcome of this correlation is the righteous. This correlation can be enhanced by means of pre-processing. Some of these technique will be briefly discussed below:

Mask appliance can be used to reduce the area which will be correlated, by applying a mask, parts of the measurement area can be eliminated. For instance a CCD sensor is normally square, when a cylinder is be observed a mask could mask the corners which are not of interest.

Background subtraction is useful when the background is dominant and disturbs the measurement. In this case a picture of the background is taken and is subtracted from each picture taken. However one needs to be aware that the background which is subtracted equals the background in the pictures for best results. This means that all reflections from the background should also be present. Therefore the background image can be recorded without tracer particles, but with laser-sheet or by the calculation of an average or minimum intensity image from a large number of images with tracer particles, at least about 35 [38].

Invert computes the negative of the image by turning bright pixels into dark ones and vice-versa. This is useful when the particles used are darker than the background. The detection algorithm requires bright data on a dark background [36].

Median filter applies a median filter to the area of pixels set. Effectively this filters out bright spots which are greater than a given area. This is especially useful for removal of large reflection spots.

Dynamic thresholding (Histogram clipping) performs a percentage-based thresholding of the image. This operation determines the minimum or maximum cut-off thresholds by summing up the individual bin-counts of the image histogram. The threshold is value is determined when the percentage of pixels in the sum exceeds the percentage specified by the user [36].

High-pass filter works by subtracting a lowpass-filtered version of the input image. The kernel size of the lowpass filter can be specified [36]. High-pass and low-pass filters are used to perform image modifications and noise reduction. It effectively makes the image sharper.

Binarize binarizes the the image data by setting pixel values above the specified threshold to white (255) and lower values to black (0) [36]. This way there is less intensity difference resulting in better correlation. The correlation scheme account for particle intensity. When the specified minimum intensity is too high. a lot of data will be lost; particle images with intensities lower than the minimum intensity are made black and do not play a role in the calculation of the average in-plane displacement.

Anti-alias This function is effectively a 2x2 pixel lowpass filter which damps out spurious noise in the image, effectively smoothing the graphics [36].

2.8.2 Correlation

Cross-correlation is normally used to correlate two separately shot PIV images as told in the introduction of section 2.8. However there are many different correlation techniques within the field of cross-correlation, each yields a slightly different correlation signal or peak. Changing the correlation technique could improve the measurement. Three of these correlation techniques are described below:

Phase-correlation (Phase-only Filtering) uses spectral filtering to eliminate amplitude information during the fast Fourier transform (FFT) based evaluation of the correlation map [36]. This increases the signal-to-noise ratio and reduces undesired influences due to e.g. wall reflections. This technique provides a contrast normalization effect due to the fact that the contribution of all sampled particle images is normalized.

Nyquist Frequency filtering removes the highest spatial frequency components in the cross-power spectrum (Fourier transform of the correlation function). This can be of use in the removal of camera noise artifacts (interlacing, multi-channel readout, etc.). The correlation plane window should be used in diagnosing the functions performance [36].

Multiple Correlation essentially calculates the correlation from at least two slightly spatially separated correlation planes. An approach based on multiplication of correlation planes was first proposed by Hart [17]. By calculating the product or sum of these correlation planes a new correlation plane results which ideally contains only the single displacement peak. Due to the random position of the noise peaks, which are present in all standard correlation planes, the final correlation plane will show no or strongly reduced noise peaks. Hence, this procedure effectively increases the detectability of the correlation peak associated with the particle shift[36].

The algorithm requires additional processing time depending on the number of additional correlations calculated and does not perform equally well on all images. A careful adjustment of the offset between the sample positions is sometimes necessary. If correlation planes are too far displaced from each other the correlation signal may be lost entirely in high gradient flows. The correlation plane window should be used in diagnosing the functions performance [36].

When the number of repeated correlations is higher (more than 3) then the averaging mode should be preferred to the multiplication, because this approach is less susceptible to loss of correlation in one of the repeated correlations [36].

These correlation techniques can further be improved by the use of digital interrogation schemes. These techniques further expand the correlation capabilities of the techniques described above. These techniques are:

Multi-pass interrogation The interrogation of the image is repeated at least once more. In the following passes the image sample positions are offset by the integer shift determined in the preceding pass. Once the residual shifts are less than one pixel a re-evaluation of the respective point is no longer necessary (e.g. convergence). The maximum number of interrogation passes can be specified. Two to three passes are generally sufficient for convergence [36].

Multiple pass interrogation not only increases the data yield due to the higher amount of matched particle images, but also reduces the so called bias-error [49]. Outlier detection is used to validate intermediate data sets. This is an addition to the correlation techniques before and differs from multiple correlation by not multiplying or averaging the correlation peak, but merely interrogates the interrogation shifts.

Grid refinement schemes - is set for a certain grid size which is bigger than the final grid size. The technique works by decreasing the grid till the desired grid size and correlating on each intermediate grid size. Intermediate results are used for the next interrogation. In this way particle displacements which are bigger than the chosen grid size can still be correlated. This technique increases the dynamic spatial range, which is the ratio of the largest observable length scale to the smallest observable length scale [33].

Iterative window deformation - deforms the interrogation areas to improve the correlation. The correlation technique normally works with rectangular interrogation areas, when flows are not uniformly and gradients are high many in-plane loss of pairs appear. To compensate for this the window deformation technique was introduced, it shapes the grid elements in such a way that the least particles are lost and thus the most correlation peaks appear. It is especially useful in highly sheared flows such as boundary layers, vortices and turbulent flows in general [38].

2.8.3 Post processing

The final step in the processing sequence is the post processing. The previous explained steps improve the correlation algorithm and therefore the obtained result. However the correlation algorithm will always correlate particles, whether this result is physically possible or not. Since the correlation is based on the statistical correlation of imaged subregions to determine local flow velocities, it is subject to inherent errors that arise from finite tracer particle numbers, sample volume size, and image resolution. These errors, in extreme cases, are relatively easy to detect as they tend to vary substantially from neighboring vectors in both magnitude and direction. Despite this, correcting these errors is often difficult as present computer algorithms lack the innate pattern recognition ability of humans. The human perceiver is very efficient in detecting these outliers [38]. Furthermore, such errors need not present themselves in obvious manners [1].

In post processing criteria can be given to detect which calculated vectors are physically righteous and which are false. Several algorithms are developed over the years and can be used to detect and replace these physically false vectors, which are called outliers:

Maximum displacement filter Any displacement vector exceeding the specified magnitude is considered to be an outlier [36].

Maximum displacement difference computes the magnitude of the vector difference between the vector in question and its eight surrounding neighbors. When this difference exceeds the specified value for more than 4 neighbors, then the analyzed vector is labeled to be an outlier [36].

Normalized median filter Applies a median filter to each vector along with its eight neighbors. A vector is an outlier if the difference to the median displacement value is greater than the given threshold [36].

Dynamic mean value filter In principle this filters works the same as a median filter but also checks the U and V component of the vector with its eight neighbors. Works especially well in shocks and high turbulence flows, since vectors tend to change instantaneously in these shock and turbulence flows [38].

Minimum Signal-to-noise filter Here the signal-to-noise ratio in the correlation plane, defined as the quotient of correlation peak height with respect to the mean correlation level, is used to validate the data. However its use is questionable because mismatched particle images or stationary background features can also produces high levels of correlation [38]. To use this outlier detection either the background features should be absent or they should removed by a preprocessing filter.

Ratio Peak 1 - Peak 2 Good correlation is defined by a high correlation peak, by setting a minimum ratio between the first and second peak, small (less correlating) peaks are regarded to be outliers. The main difference between Peak Ratio and Minimum Signal-to-noise filter is that the prior looks at the ratio between the highest and the second highest correlation peak. While the Minimum Signal-to-noise filter looks at the highest correlation peak with respect to the mean correlation level. Peak Ratio is therefore a stricter outlier detection scheme. Care has to be taken using this filter when seeding levels are low since high correlation coefficients may arise from mismatched areas.

Minimum correlation - Low correlation in a interrogation area is likely to be due to low correlation and thus loss of particles. Imposing a minimum correlation percentage could identify outliers. However it is of lesser importance for the actual validation of PIV data,a s low correlation values do not necessarily point to invalid displacement readings.

Global histogram filter - Uses the assumption that the difference in velocity between neighboring vectors must be lower than a certain threshold. With this filter a two-dimensional histogram is made by plotting the velocities or displacements, recovered from the correlation peaks, of all vectors in a single plane. A rectangular or circular box is calculated circumscribing the highest accumulation of the correlation peaks [38].

Outliers can either be completely removed from the data set or they can be interpolated. This interpolation applies a bi-linear interpolation over its eight neighbors to estimate the replacement vector. When several of the immediate neighbors are also outliers then a Gaussian-weighted interpolation scheme is used [36]. Another possibility is to try a lower order peak, but this is discutabel, since the lower peak might be noise or a mismatched area. Finally in the multi-grid technique it is possible to check if the outlier can be replaced by a vector which arises from a greater interrogation area. If none of the alternative correlation peaks fulfill the validation criteria, the image can be locally re-evaluated with the next largest interrogation sample in the multi-grid processing scheme.

Chapter 3

Test Setup & Data evaluation

This chapter explains how the setup is constructed and what design considerations are made. This information could be important for future participants in this research, this chapter will explain why certain components were chosen and will provide a greater insight in the design of the setup.

3.1 Design Considerations

The first concern in building a setup, is its placement. The requirements to install the setup and guarantee proper operation should therefore be identified. The requirements are:

- House a heavy duty cylinder-head
- Connection to a 983 m^3/h pressurized air-supply (maximum flow at maximum valve lift) This can be calculated using the formulas 2.6 and 2.7 from section 2.1.2:

$$\dot{m}_{th} = \sqrt{\frac{2 \cdot 10 \cdot 10^3}{1,293}} \cdot 1.293 \cdot 2 \cdot \frac{\pi}{4} \cdot 0.0374^2 = 0.3533 \qquad [\frac{kg}{s}] \tag{3.1}$$

$$Q_{th} = \frac{\dot{m}_{th} \cdot 3600}{\rho} = \frac{1.272 \cdot 10^3}{1.293} = 983.74 \qquad [\frac{m^3}{h}] \tag{3.2}$$

  Note that this is the maximum theoretical mass flow, disregarding C_D and C_F since these variables have yet to be determined.

- It should be placed in an enclosed room, due to safety requirements concerning pressurized setups and laser equipement.

The most obvious location to meet all of these requirements is inside the engine cells. An engine cell can be enclosed and each cell has a connection to the 1000 m^3/hour 8 bar(gauge pressure) air-supply.

Due to limited space the setup is rotated from a horizontal orientation to a vertical one as is indicated in figures 3.1. It is assumed that this orientation does not influence the measurements since the particles are chosen small enough (1 μm) to have good flow flowing

characteristics. This implies that any gravitational effects on the particles can be neglected. This orientation also means that the setup will be rather high. to maintain easy access to all components. a second story is added to the setup.

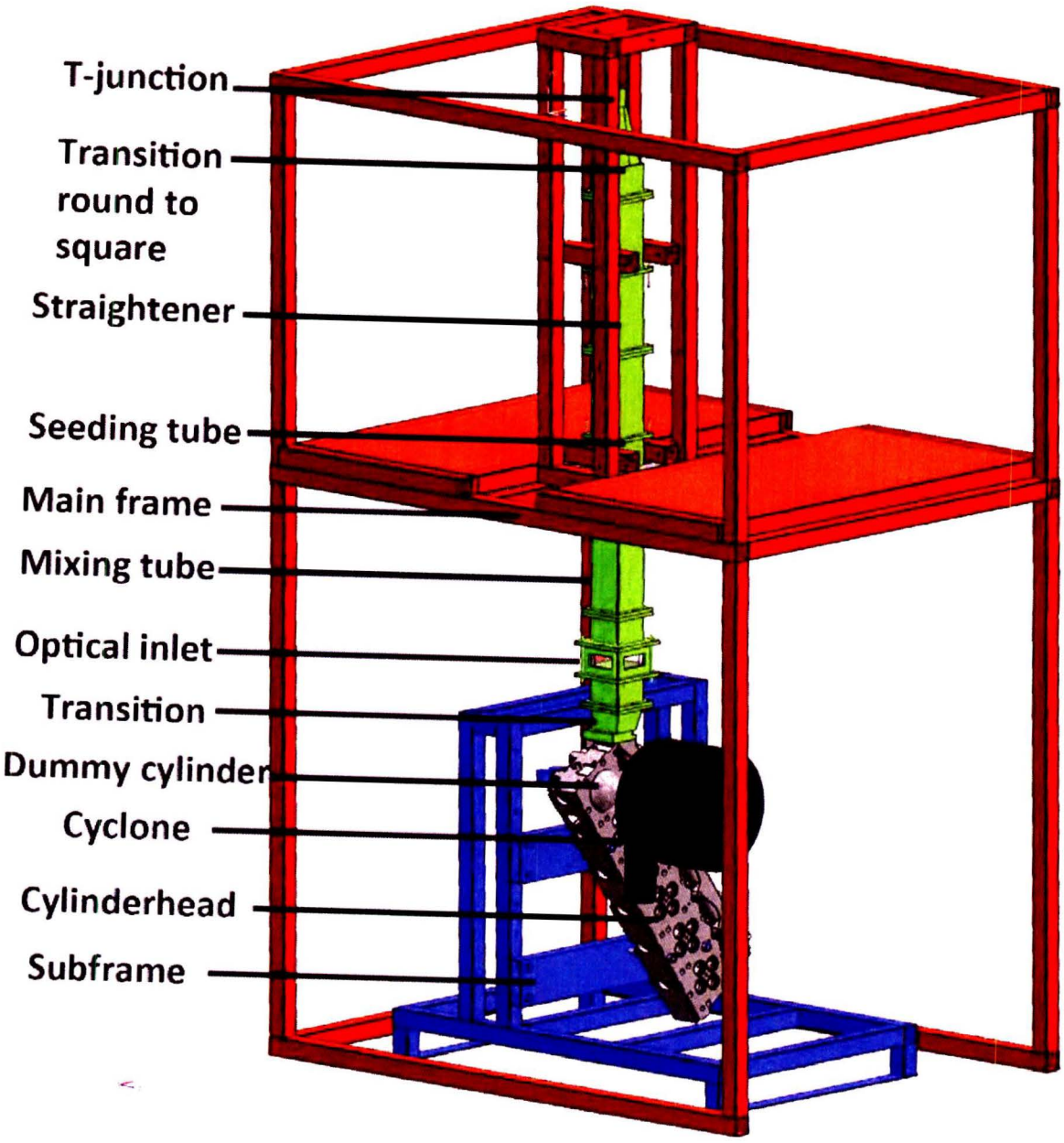

Figure 3.1: Schematic representation. Black: Cyclone; Blue: Subframe; Gray: Cylinder head; Green: Inlet piping; Red: Mainframe

3.2 Experimental setup

Although the construction of this setup seems very straightforward, some design issues need to be considered before building it. To optimize the compatibility of the setup to different cylinder heads it was decided to build the setup out of separate modules. In this way it is easy to replace and service all components. This also allows for easy alterations on the cylinder head. In essence the setup consists of two main constructions, the main frame with its piping and the subframe with the cylinder head as seen in figure 3.1. Both structures and their substructures will briefly be discussed in the next sections.

3.2.1 Optical access

To allow for PIV measurements the setup needs optical access for the laser sheet to pass through. Two flow patterns are of interest in this investigation, the inlet flow and the in-cylinder flow. Both flows are important in CFD analysis.

To allow for optical access in the cylinder, the dummy cylinder is composed entirely out of glass. This glass has the internal diameter of the bore of the cylinder (130 mm) and a wall thickness of 5 mm, this is chosen to allow for pressurized measurements inside the glass cylinder. Between the cylinder-head and the glass tube a rubber u-profile is positioned to seal the transition and to avoid contact between the glass cylinder and cylinder-head. The rubber ring also allows for some play, since the glass cylinder will be clamped between the cylinder-head and the cyclone. There is 2 mm of rubber between the glass and metal of the cylinder-head, the rubber ring is 5 mm high and puts 2 mm of rubber around and inside the circumference of the dummy cylinder as can been seen in figure 3.2.

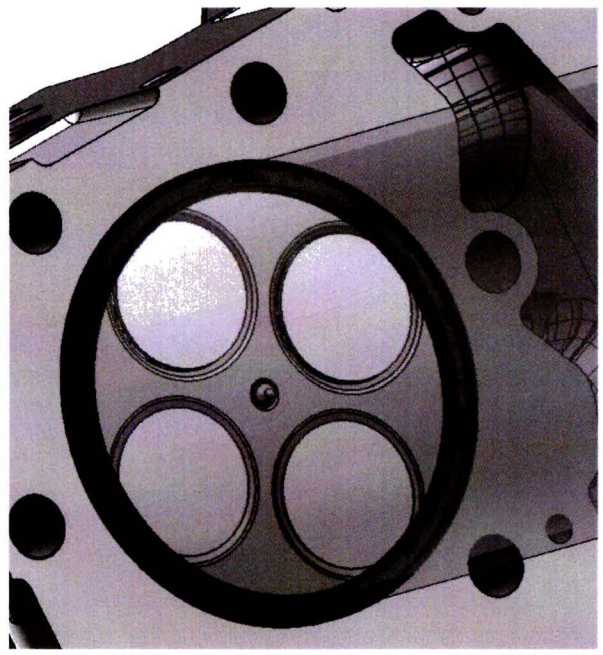

Figure 3.2: Dummy cylinder

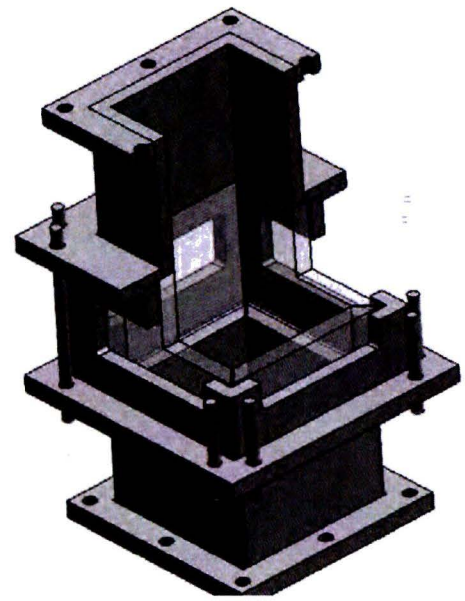

Figure 3.3: Optical inlet tube

The optical inlet channel allows for PIV measurements inside the inlet channel. The most difficult requirement to this part, was that it could not disturb the flow inside the inlet channel and the access was large enough to allow for good visualization of the flow. Therefore the glass is positioned in such a way that the internal dimensions of the channel are preserved and the slots in the channel are made as large as possible.

The optical inlet channel is a sandwich construction. In the sides of a bigger dimensioned rectangular stainless steel tube, gaps are milled. This tube allows for 15 mm thick miter-cut glass windows, while preserving the inner dimensions of the inlet channel as can been seen in figure 3.3. Small openings are kept between the glass windows and the rectangular tube to allow for sealing. The glass windows and rectangular tube have the same height dimensions. This assembly of glass and steel is clamped between to steel flanges with a rubber gasket in between to ensure sealing. The whole assembly can been seen in figure 3.3.

3.2.2 Main Frame and Piping

The mainframe is the basic structure of the setup, it houses the inlet piping and provides room for the subframe to be placed underneath. The piping is attached, by struts, to the second story of the main frame, in this way the piping can be hoisted from the cylinder-head to remove the subframe from underneath. The subframe is designed to be easily removed by means of a pallet wagon, whenever maintenance or alterations are needed to the cylinder-head.

The piping is made from square stainless steel channels which have outer dimensions of 120 millimeter and wall thickness ten millimeter. The piping is square since this allows easy optical access, due to straight walls. The inner dimensions of the channels are chosen in order to cope with the large airflow. The wall thickness is chosen to withstand an internal pressure of three bars, which is the maximum intended pressurize during measurements. Finally stainless steel is chosen as material due to its durability and strength.

The piping is composed out of several individual demountable parts which will be explained in table 3.1. The are joint by flanges with rubber gaskets in between them. Figure 3.1 shows all the components and their relative position in the piping system. All but one, which is the bleed valve it is positioned on top of the T-junction as can been seen in figure 3.5. The seeding channel is positioned after the straightener in order to keep the straightener clean. Preferably the straightener would be place directly after the seeding channel, since inhomogeneities in the flow improve mixing of the seeding as stated in section . However due to the nature of the seeding the straightener would be oil dogged and the straightening properties would deteriorate.

Table 3.1: Parts of piping system

Component	**Length**	**Function**
Bleed valve	3 inch	safety valve for pressuring the setup, prevent pressures inside exceeding 3 bar(g)
T-junction	2 inch	connection for supply hose to piping and bleed valve
Transition round to square	285 mm	allows for smooth transition of round 2 inch geometry to square 100 x 100 mm geometry
Straightener	500 mm	is fitted with a honeycomb to straighten out any inhomogeneities in the air flow. It is constructed from plastic plates, the channels of the straightener are 1 x 1 mm, the honeycomb is secured inside the piping using sikaflex kit
Seeding tube	300 mm	allow for a seeding nozzle to be inserted at different depths, to supply seeding to the flow
Mixing tube	800 mm	allows for the seeding particle to set in the flow and obtain a homogeneous distribution of seeding
Optical inlet	300 mm	allows for optical access as described in section 3.2.1
Transition	110 mm	converts the flow from a 100 x 100 mm rectangular flow area to the complex geometry of the cylinder-head inlet
Cyclone	400 mm	allows for free outflow of the air and allows optical access to the dummy cylinder.

3.2.3 Subframe and Cylinder head

The subframe houses the cylinder head as well as the pressure sensors used in the setup. The cylinder head is attached to the subframe by four M18 rods. The rods fit in the cylinder head bolt holes, spacers assure that the valves are still operational. Figure 3.1 shows the assembly of the subframe and cylinder head.

The first cylinder of the cylinder head is used for testing. The valves can be adjusted by two bolts, which have a center hole through which a dial gauge presses down on the valve stem. This allows for accurately measurement of the valve opening, since play is minimized. With this system the actual valve lift can be observed to an accuracy of 0,01 mm. This is important since the momentum of the flow might increase the valve lift during measurement.

The outlet cyclone is fastened to the cylinder-head by means of studs to the cylinder head, as can been seen in figure 3.4. The sealing between the cylinder-head and glass tube is assured by a rubber ring. While a rubber o-ring inside the cyclone ensure sealing between the outlet cyclone and glass dummy cylinder.

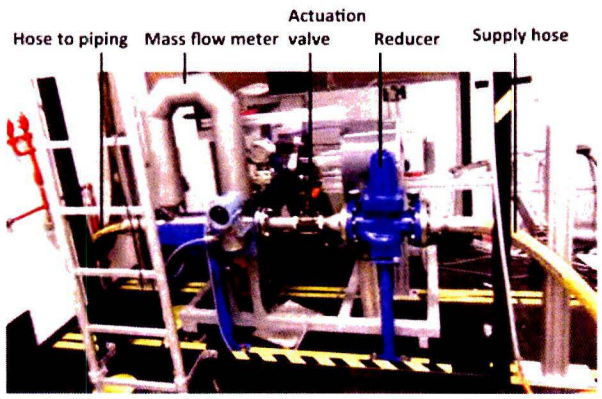

Figure 3.4: Air supply, ground level

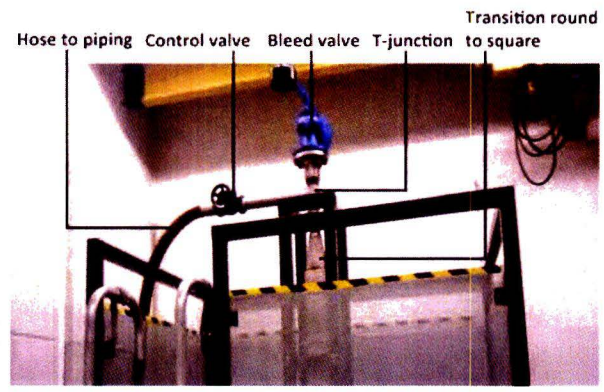

Figure 3.5: Air supply, first story

3.2.4 Air supply

The air connection point to the university air grid is situated underneath the engine cell. A high pressure 2 inch supply hose is used to connect the setup to this air supply. The hose guides the air to a reducing valve. Straight after this reducer valve an actuation valve is situated to easily cut off flow to the setup. This valve also allows for easy removal of the mass flow meter (see chapter 3.3.4). All piping used around the actuation valve consists of two inch easy attainable stainless steel pipes. Calculations show that this is capable of supporting the intended volume flow at 4.5 - 8 bar.

A second hose connects the mass flow meter the air flow to a control valve at the first story where it is connected to a control valve. This control valve allows for manually adjustments. The layout of the air supply can be seen in figures 3.4 and 3.5.

3.2.5 Seeding

In a flowbench mass flow will change with valve lift. In order to obtain good seeding density (8 - 10 particles per interrogation area) the seeding flow should therefore also increase with valve lift. The range in between which, the seeding device should work is approximately 0 - 983 $\left[\frac{kg}{s}\right]$. To allow for this range a Laskin device with 6 independently connectable Laskin nozzles was constructed. And a reducing valve is installed in the seeder air supply to allow for variations in pressure and thus seeding.

These Laskin devices usually use oil to disperse into seeding. The optimal particle diameter needed can be determined using formula 2.5.1 from section 2.5.1. The formula is repeated for completeness:

$$d_p \leq \sqrt{0.4082 \cdot \frac{\mu}{f_c \cdot \rho_p}}, \qquad [m] \tag{3.3}$$

The dynamic viscosity (μ) of air at room temperature is 1.85 $\dot{1}0^{-5}$ $\left[\frac{Pa}{s}\right]$. the density of oil ($\rho_p$) is normally in the order of 900 $\left[\frac{kg}{m^3}\right]$ and finally the highest turbulence scale f_c needs to be determined. The smallest scales in fluctuating flow is the Kolmogorov micro scales as mentioned in section 2.7 using formula 2.53 and 2.54 the time scale can be determined. Assuming

the characteristic length to be the valve lift (15 mm) and typical fluctuating velocities of 20 $\left[\frac{m}{s}\right]$, a Kolmogorov time scale of 5.30 μs can be calculated. This corresponds to a frequency of 188.6 kHz, which in terms solves equation 3.3, $d_p = 0.2$ μm. However this length is much smaller than the spatial resolution by PIV analysis, which is 2.13 mm in this experiment. Using this length and formula 3.4 the highest turbulence scale f_c can be calculated.

$$f_c = \frac{\omega_c}{2 \cdot \pi \cdot r} = \frac{V}{2 \cdot \pi \cdot r}, \qquad [Hz] \tag{3.4}$$

with r the smallest time scale and V the typical fluctuating velocities. The highest turbulence frequency using the spatial resolution is 1.49 kHz resulting in a d_p of 2.3 μm. Particles smaller than this size can follow the turbulent fluctuations of the flow up to 1.49 kHz at an accuracy of 95%. Since the method of Laskin is proven and capable of producing seeding with a particle diameter of 1 μm this d_p was chosen in this experiment. Note that with this data all variables in section 2.7 can be calculated.

The seeding medium initially chosen was silicon oil with a viscosity of 100 cSt. Using silicon oil in a Laskin device ensured 1 μm droplets to be produced [26] [24]. However the silicon oil is very adhesive and accumulated on the glass during operation thus disturbing the measurement.

Another frequently medium used for seeding medium is Di(2-ethylhexyl)sebacate (DEHS) [24] [42]. This oil has the same properties of silicon oil (see table 3.2, the only difference is that DEHS is less adhesive than silicon oil and therefore measurements can be prolonged. Less frequent cleaning of the glass surfaces is needed, which allows longer measurement sessions. Table 3.2 states the properties for silicon oil and DEHS. The volumetric particle size distribution of DEHS under different conditions can be found in appendix C.

Table 3.2: Properties of Silicon oil and DEHS [40]

Physical property	**Silicon oil**	**DEHS**
Chemical formula	$(-Si(CH3)2O-)n$	$C_{26}H_{50}O_4$
Density	965 $\left[\frac{kg}{m^3}\right]$	914 $\left[\frac{kg}{m^3}\right]$
Vapor pressure	7 hPa at 25 $^\circ C$	$5 \cdot 10^{-3}$ hPa at 37 $^\circ C$
Kinematic Viscosity	$1 \cdot 10^{-4}$ $\left[\frac{m^2}{s}\right]$	$2.52 \cdot 10^{-5}$ $\left[\frac{m^2}{s}\right]$
Refractive index	1.403	1.454
Surface tension	$2.09 \cdot 10^{-2}$ $\left[\frac{mN}{s}\right]$	$3.2 \cdot 10^{-2}$ $\left[\frac{mN}{s}\right]$
Typical droplet size after atomization	1 μm	1 μm

3.3 Peripherals

To preform PIV measurements and collect data concerning the setup, additional equipement was used outside the constructed setup. Such as a laser and camera to obtain PIV measurements and pressure sensors to log the pressures inside the setup. This section will elaborate on this equipement.

3.3.1 Laser Equipement

In this experiment two lasers are used, both lasers are Neodymium-doped YAG lasers, which means that the active media of this laser are Yttrium Aluminum Garnet (YAG) crystals. These lasers are optically pumped using a flashlamp, pumping energy to the lasing material. Nd:YAG lasers produce a infrared-light at a wavelength of 1064 nm. Inside the laser casing this wavelength is frequency-doubled using a nonlinear crystal. After separation of this frequency-doubled portion, the light energy at a wavelength of 532 nm has reduced to a bit less than half of the original light energy. This laser is operated with a so-called Q-switch mode, which allows for the laser energy to leave the lasing medium in a very short time ($\sim$ 5 nm) at high powers ($\sim$ 60 mJ per pulse).

Initially a Quantel Brio Twins laser was used which had a repetition rate of 10 Hz and an effective pulse-energy of 60 mJ. Unfortunately this laser broke down during experiments, due to a leakage in one of the cavities, and a replacement had to be found. The replacement was a Quantel Twins BSL 50 which is based on the same principle as the Brio Twins and actually uses the same Brio ICE power supply as the Brio Twins. The Twins BSL 50 has a repetition rate of 15 Hz and an effective pulse-energy of 50 mJ. The specifications of both lasers can be found in appendix D. The laser beam was converted to a sheet using a converging lens with s focal point of 75 mm and a diverging lens with a focal point of 25 mm

3.3.2 Camera equipment

The camera used in this experiment is a CCD type Kodak ES 1.0 camera. The maximum capture rate is 15 frames per second at single exposure and 30 frames per second at double triggered exposure. The latter is used in this setup, since two laser pulses will be generated at 10 Hz. The maximum resolution of the CCD chip is 1008 (H) x 1018 (V) pixels and each pixel is 9 μm x 9 μm. The CCD chip is capable of detecting 10 bit digital images giving 1024 gray levels per pixel, resulting in high detail contrast. The camera is used in combination with a Nikon AF-Nikkor 50mm 1:1.4D lens.

3.3.3 Triggering

To sync the camera and laser a Standford DG535 Digital Delay/Pulse Generator is used. This pulse generator provides four precisely-timed logic transitions or two independent pulse outputs. The delay resolution on all channels is 5 ps. Additionally this pulse generator has a T_0 channel which is used to trigger the camera. The other 4 channels are used to trigger the two flashlamps and q-switches of the double cavity laser. The timing scheme can been seen in figure 3.6.

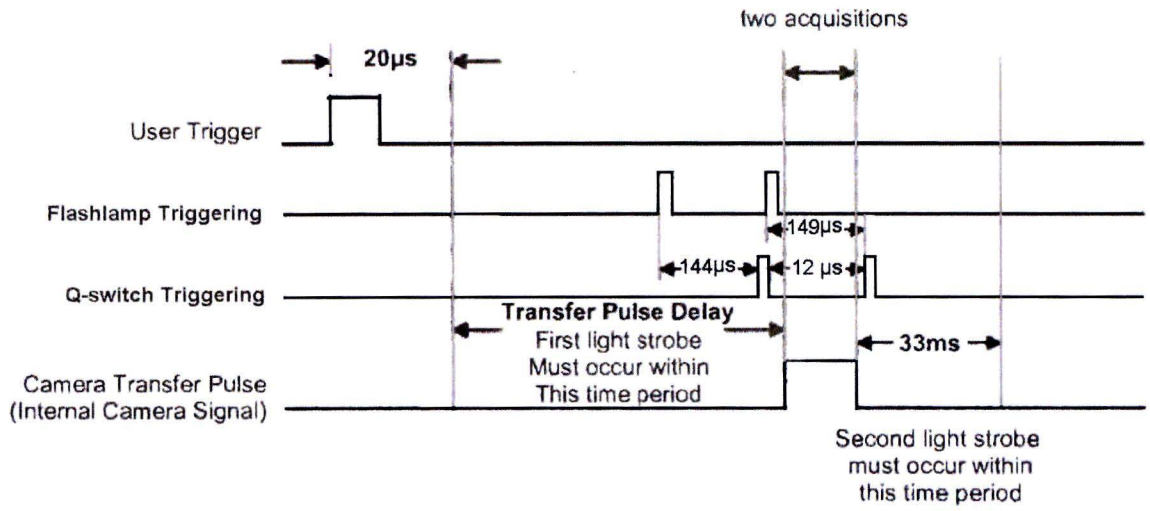

Figure 3.6: Triggering of laser and camera

3.3.4 Data acquisition

This setup also allows for pressure and mass flow measurements, these peripherals will be further elaborated in this section.

Air flow measurement

The setup contains a Micro Motion CMF200 Mass flow meter capable of measuring up to 13300 $\left[\frac{kg}{h}\right]$ or 10300 $\left[\frac{m^3}{h}\right]$. The mass flow meter uses the Coriolis effect to measure mass flow.

Pressure measurement

The setup contains two pressure meters, a Honeywell S900 pressure difference meter capable of detecting pressure difference in the range of 0 - 16 kPa. And a Cerabar T absolute pressure meter produced by Endress and Hauser which has a range of 0 - 4 bar. The absolute pressure meter is connected to the intake manifold of the cylinder-head and measures the pressure inside the piping and intake manifold. The pressure difference meter is on one side connected to the inlet manifold and on the other side to the outlet cyclone, effectively measuring the pressure difference over the cylinder-head (valves).

3.4 Data processing

During the PIV measurements 500 pairs will be taken, corresponding to 500 PIV sets. These sets will be analyzed using PIVview [36] and MATLAB. This section examines the influence of the correlating techniques and which pre- and post processing options on velocity calculations.

3.4.1 Outlier definition

To quantify the number of righteous vectors, firstly the definition for an outlier should be determined. Section 2.8.3 already mentioned the different options for outlier detection. The most widely used outlier definition is the normalized median filter with a threshold of 2 - 4 [50] [10]. This report uses the same outlier detection as well as the ratio peak 1 - peak 2 of 2. The is a very strict outlier definition it can be applied since seeding levels are high. The idea behind applying this outlier detection is that only the highly accurate (reliable) data remains. Due to the share volume of the data set enough highly reliable vectors will remain to plot the results.

Displacement are very small in the data set, due to the high out-of-plane velocity so there is no point in using maximum displacement and maximum displacement difference as an outlier definition. Although the dynamic mean filter (DMF) works well in shocks and turbulent flows, it smoothes the obtained vector field. The DMF compares the U an V component of the vector with its eight neighbors, if it differs the vector is regarded as an outlier. This implies that very small structures inside the flow (range 2 - 4 interrogation areas) will be regarded as outliers. The working principle of minimum SNR and minimum correlation detection are about equal to ratio peak 1 - peak 2 only less stringent. And finally the global histogram filter was not chosen due to the fact that this filter overlooks the entire generated vector field and regards the displacement inside this vector field to be within a certain threshold. However some velocities are higher than this threshold and are therefore incorrect labeled as outliers.

Basically three options for outlier replacement exist in PIVview: Try lower peaks, interpolation and re-evaluate with large sample (multi-grid only). Of these three options the latter is chosen, the multi-grid interrogation scheme will prove to be very competent in correlating the pixels. Try-lower peaks counters the previous outlier detection of ratio peak 1 - peak 2, and is therefore disregarded. Interpolation is a option, but the data set is large enough to disregard the outliers. It is assumed that a disregarded vector is of more value to the reliability of the generated vector fields than interpolated vectors.

3.4.2 Pre-processing

To investigate which combination of pre-processing steps should be applied, one of the better image sets was used and processed. The first step was to apply a mask to isolate region of interest as can been seen in figure 3.8. The correlation methods was set to multi-grid refinement (starting at 128 x 128) since this technique increase the dynamical spatial range [38]. Initially no outlier definition was defined. The final interrogation window was set to 64 x 64 pixels with an overlap of 75% resulting in 3600 vectors.

The mask disabled 660 vectors (19.0%). After applying the ratio peak 1 - peak 2 of 2 and normalized median filter with a threshold of 3, the disabled vectors rose to 1068 (24.2%). Different pre-process methods were tested, the table below show the results: Test 11 proved

Table 3.3: Outlier detection under different pre-process conditions

Test	**Median filter (3X3)**	**Dynamic thres-holding**	**High-pass filter (10px)**	**Binari-zation tresh=130**	**Anti-alias 3 x 3 gauss**	**Outliers**
1	No	No	No	No	No	24.2%
2	Yes	No	No	No	No	23.6%
3	No	(5% - 95%)	No	No	No	23.0%
4	No	No	Yes	No	No	25.5%
5	No	No	No	Yes	No	25.8%
6	No	No	No	No	Yes	20.1%
7	No	No	Yes	No	Yes	20.9%
8	Yes	(5% - 95%)	No	No	No	20.4%
9	No	(10% - 97%)	No	No	No	22.8%
10	No	(5% - 95%)	No	No	Yes	19.8%
11	No	(10% - 97%)	No	No	Yes	19.9%

Valve lift: 4 [mm], Distance: 90 [mm]; Mass flow: 91.6 $\left[\frac{g}{s}\right]$

to show the least outliers and therefore it was chosen to apply a dynamic thresholding filter (DTF) of (10% - 97%) to the data as well as an anti-alias filter. The DTF removes the 10% of the darker pixels and 3% of the brightest. The darker pixels are likely to be noise and the brightest particles are due to glass scattering. The anti-alias filter blends the edges of the particle, making it slightly bigger, thus obtaining better correlation.

Although test 10 gave slightly better results for this particular situation it assumed that the more stringent DTF setting of test 11 reduces more noise of darker pixels while still suppressing glass scattering.

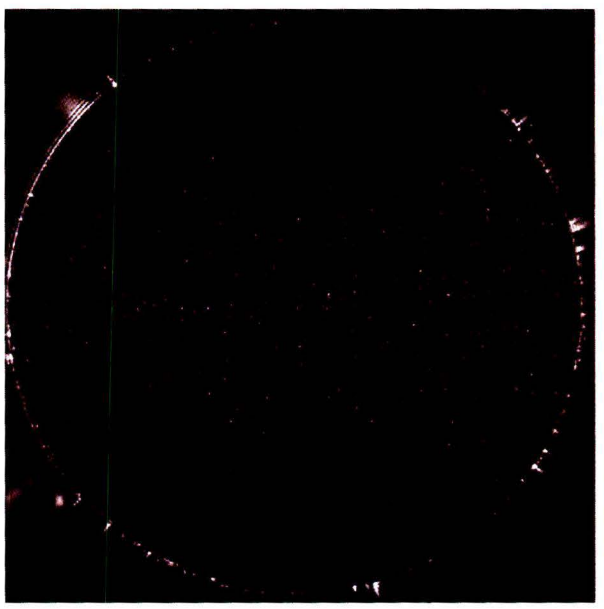

Figure 3.7: Original obtain PIV picture

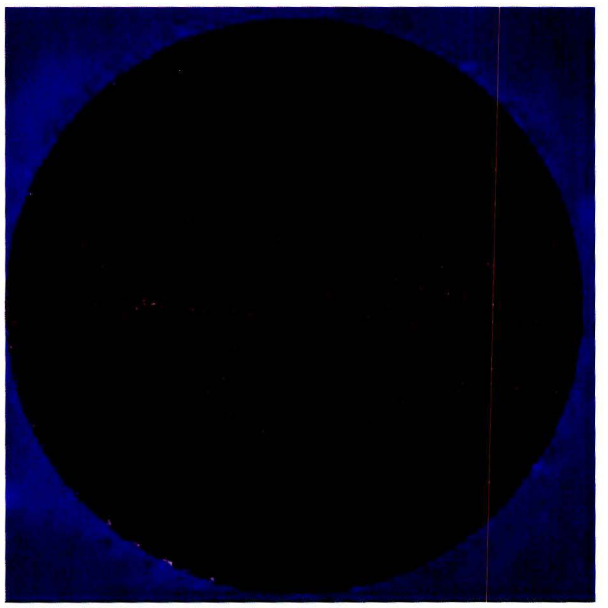

Figure 3.8: PIV picture with mask and pre-processing, dynamic thresholding filter (10% - 97%) and anti-alias

Valve lift: 4 [mm], Distance: 90 [mm]; Mass flow: 91.6 $[\frac{g}{s}]$

3.4.3 Correlation technique

By keeping the pre-processing steps constant, altering the correlation techniques, the multi-grid scheme is tested to be the most accurate scheme. Table 3.4 shows the results of the different correlation scheme investigated.

Note that grid refinement is standardly set at 128 x 128 in table 3.4 or otherwise noted. Table 3.4 confirms multi-grid refinement to be the optimum correlation algoritme. The initial sampling window does not affect the outlier outcome, but does so with the time needed to execute the correlation. However, the initial window is kept at 128 x 128, although it makes some difference in time selecting a window twice as big as the interrogation window adds to the reliability of the generated velocity field.

Although times might seem insignificant keep in mind that the correlation has to be executed 500 times for one measurement. The selected scheme (test 16) takes roughly 28 minutes to be completed, without additional time for the program to write the data to disk, using a HP xw4400 workstation with an Intel Core 2 Duo E6600 2.40 GHz (4 MB L2, 1066 MHz FSB) from the year 2006.

Note that after this pre-processing, correlation and outlier detection only 19.7% - 19% = 0.7% is considered outlier, while using stringent settings.

Table 3.4: Outlier detection under different correlation conditions

	Correlation technique	**Algorithm**	**Outlier**	**Time**
1	Phase-correlation	Single-pass interrogation	28.0%	2.06 [s]
2	Phase-correlation	Multi-pass interrogation (3)	26.9%	5.30 [s]
3	Phase-correlation	Multi-grid refinement	21.1%	11.03 [s]
4	Nyquist Frequency Filtering	Multi-grid refinement	19.7%	7.98 [s]
5	Nyquist Frequency Filtering	Multi-pass interrogation (3)	26.9%	5.17 [s]
6	Nyquist Frequency Filtering	Single-pass interrogation	27.5%	1.47 [s]
7	Multiple correlation (Multiplication)	Single-pass interrogation	23.2%	3.59 [s]
8	Multiple correlation (Multiplication)	Multi-pass interrogation (3)	22.7%	7.00 [s]
9	Multiple correlation (Multiplication)	Multi-grid refinement	19.6%	8.92 [s]
10	Multiple correlation (Averaging)	Single-pass interrogation	26.5%	3.50 [s]
11	Multiple correlation (Averaging)	Multi-pass interrogation (3)	26.1%	6.59 [s]
12	Multiple correlation (Averaging)	Multi-grid refinement	19.9%	6.63 [s]
13	Multiple correlation (Averaging) Nyquist Frequency Filtering	Multi-grid refinement	19.9%	6.14 [s]
14	Multiple correlation (Averaging) Nyquist Frequency Filtering Phase-correlation	Multi-grid refinement	20.6%	14.22 [s]
15	Multiple correlation (Multiplication) Nyquist Frequency Filtering Phase-correlation	Multi-grid refinement	20.0%	12.24 [s]
16		Multi-grid refinement	19.7%	3.34 [s]
17		Multi-grid refinement (96 x 96)	19.7%	3.09 [s]
18		Multi-grid refinement (160 x 160)	19.7%	4.31 [s]

Valve lift: 4 [mm], Distance: 90 [mm]; Mass flow: 91.6 $\left[\frac{g}{s}\right]$

3.4.4 Peak-locking

When particle images become too small, the peak-locking effect may arise. This effect means that the displacements tend to be biased towards integral values. The effect increases as the particle image diameter (d_{tau}) is reduced which is a clear indication that a better subpixel peak estimator should be chosen [38]. This effect can be observed in the actual displacement data, by plotting the displacement histogram such as given in figures 3.9 and 3.10. In general standard 3-point subpixel peak estimators do not preform well when the particle image size is smaller than 1.5 pixel, which is the case in this project. Table 2.12 shows that the particle image size is 1.9 μm, this while the pixels of the used camera are 7 μm indicating that a single particle in this experiment is smaller than the pixels of the CCD-chip. This problem is reduced during pre-processing where the anti-alias filter is used. This filter blurs the particles, which makes them bigger in size, resulting in better correlation. When figure 3.9 and 3.10 are observed no big differences appear between the chosen sub pixel peak fits. Note that the scale for horizontal displacement is slightly different. Therefore this report uses the normal 3 point gauss peak estimator.

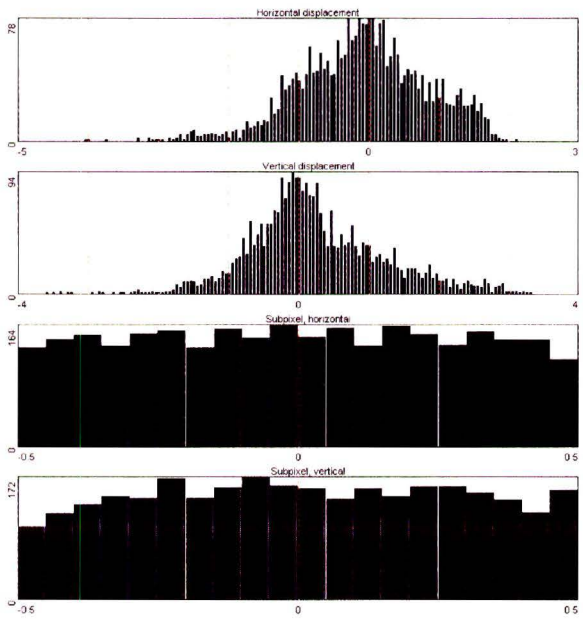

Figure 3.9: Histogram using 3 point Gauss estimator

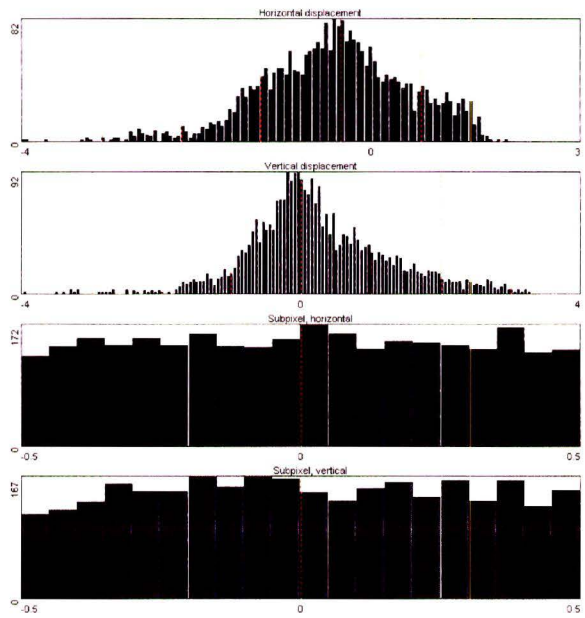

Figure 3.10: Histogram using least squares Gauss estimator

Valve lift: 4 [mm], Distance: 90 [mm]; Mass flow: 91.6 $\left[\frac{g}{s}\right]$

Chapter 4

Results

Tangential measurements were preformed at various distances from the cylinder-head and at various valve-lifts. The distances from the cylinder-head were varied between 30 and 130 millimeters and the valve-lift varied from 1 to 5 millimeters. Axial measurements were preformed at various valve-lift (1 - 5 millimeters) trough the center of the cylinder and with the laser-sheet at the axis an axis over the valves.

In all individual experiments 500 image-pairs were taken. resulting in 500 correlating pairs. These pairs were correlated using PIVview (the used settings are elaborated in section 3.4.3). The correlation by PIVview results in single data files per correlation which contain the velocity fields corresponding. For further data-analysis MATLAB is used.

This report will show the obtained from PIV as well as results obtained from the pressure and mass flow data.

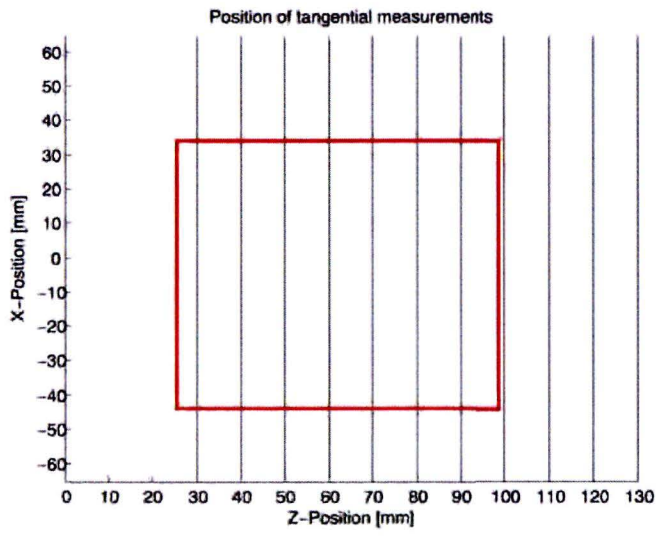

Figure 4.1: Indication of tangential measurement planes and axial measurement area. The cylinder-head is positioned at z = 0.

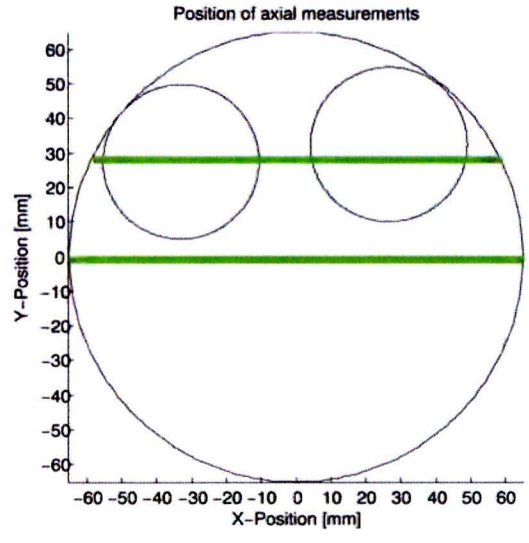

Figure 4.2: Plot indicating the heights of the axial measurements. The injector is positioned at x & y = 0.

4.1 PIV results

In PIV analyses the smallest length scale which can be measured is of importance. it determines which structures can be visualized. The correlation in PIVview was done with a 64 x 64 pixel interrogation window with 75% overlap. The results contain 60 x 60 vectors. The pixel to millimeter relation in the tangential experiments is around 7.5 pixels per millimeter. indicating that the smallest observable length scale in this experiments is 2.1 millimeter. The distance between the camera and laser-sheet is kept constant throughout the experiment resulting in a fixed length scale.

In the axial experiments the pixel to millimeter ratio is around 13.5 indicating that the spatial resolution in these measurements is 1.2 millimeter. In these measurements the camera is also kept at a fixed position. Figure 4.1 indicates the area of the axial measurements and the position of the tangential measurements. while figure 4.2 indicates the heights of the axial measurements.

4.1.1 Quality of the images

An important issue in evaluating PIV results is the quality of the recording. This starts by acquiring sharp. detailed pictures of the particles in the flow (as shown in figure 4.3). These pictures are further enhanced to optimize the correlation techniques. as explained in section 2.8. An outlier definition has been specified indicating false vectors. PIVview correlates the data accordingly. the produced data is used for analysis.

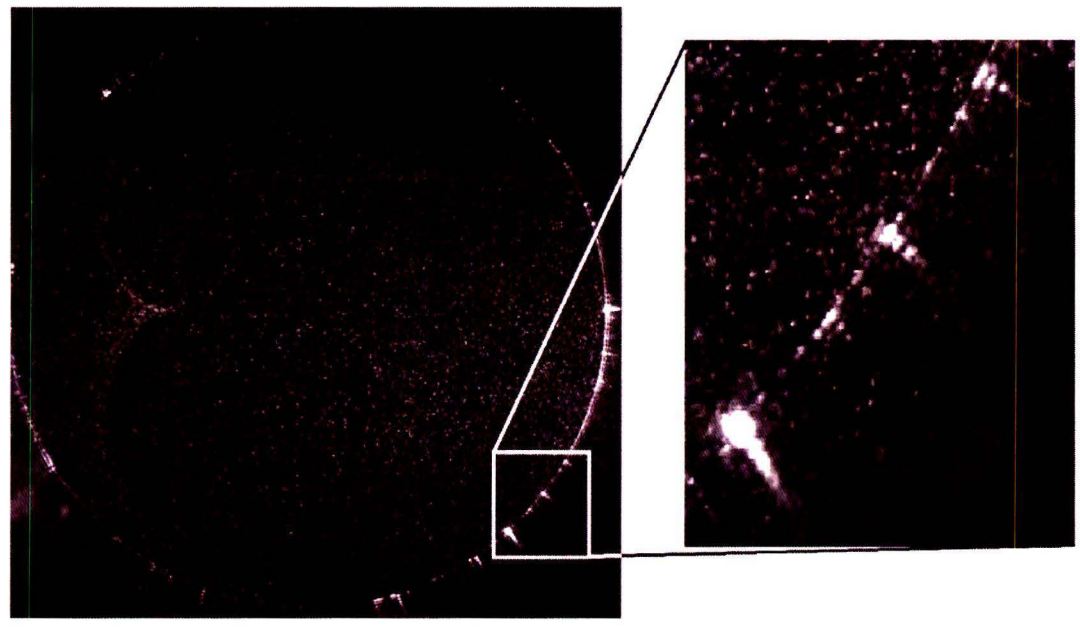

Figure 4.3: Raw PIV image obtained during measurement

Outliers

In this report the data has been judged upon its outliers. The quantity of outliers is a measure for the quality of the data. Essentially the outlier definition states what is accepted as data and what is not.

PIVview exports, among other variables, the flags of the vectors which were correlated. Each individual vector has a flag which indicates how the vectors exported should be interpreted. These flags are normalized in MATLAB, were the flag "1" indicates valid data and the flag "0" indicates an outlier. By adding all these flag a (3600 x 500) flag matrix is generated. By summing this flag matrix over all 500 measurements a grid can be specified, indicating the percentage of reliable vectors per interrogation area.

This grid can provide vital information about the quality of the correlation. Problems in the PIV evaluation can be located, for instance if in some region the amount of reliable vectors is significantly lower than the rest this can indicate a problem like a thinner laser-sheet at that position and thus more out-of-plane particles.

Figure 4.4 shows the amount of reliable vectors. This figure shows that in the section of interest on average 80% of vectors are valid vectors, the other 20% are outliers. This might seem much but one should keep in mind that the outlier definition is harsh and no interpolation is used to substitute false vectors. Although only 80% of the vectors remains these vectors are reliable, and are therefore used for further calculations. This is in contrast with the 0.8% outliers that were present in the correlation done in section 3.4.3, however the image pair used in that section was one of the better in the entire measurement.

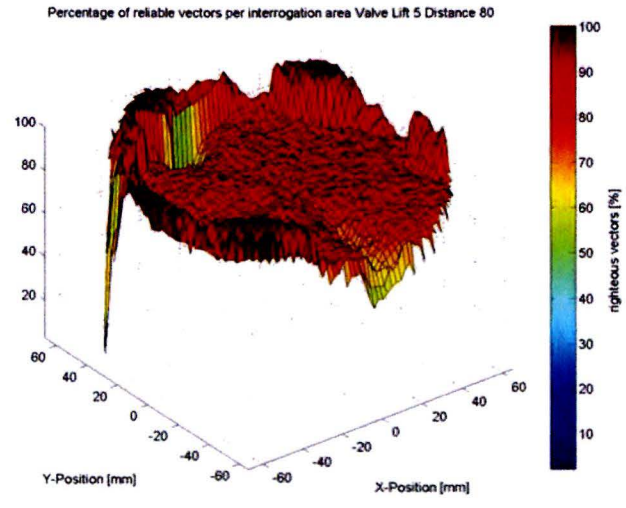

Figure 4.4: Plot of the quality of measurement
Distance from cylinder-head = 80 [mm],
Valve-lift = 5 [mm], Mass-flow = 122.3 $\left[\frac{g}{s}\right]$

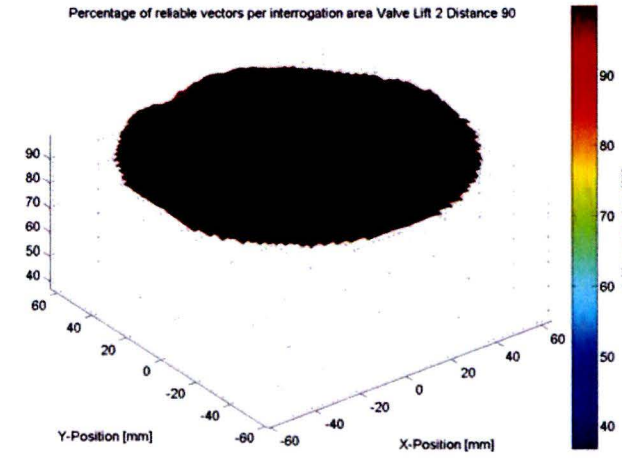

Figure 4.5: Plot of the quality of measurement
Distance from cylinder-head = 90 [mm],
Valve-lift = 2 [mm], Mass-flow = 50.5 $\left[\frac{g}{s}\right]$

In figure 4.4 the circumference of the cylinder can clearly been seen. On this circumference the quality seems to be better than in the middle. This has to do with scattering at the cylinder-wall (as can been seen in figure 4.3), either scattering is present and correlation is near 100% or it is absent and correlation is weak. The influence of this on further evaluations is negligible. Scattering occurs in both frames and therefore correlation will be 100%, but the net displacement will be 0. This indicates that around the circumference it is hard to obtain vector information due to scattering and velocities will be lower. However it is in principle very harsh to obtain good vector information with PIV in the proximity of a cylinder wall due to boundary layers and possible lift effects on the particles as elaborated in section 2.5.1.

In the case of low correlation the problem is more dominant, this is caused by actual particle scattering reflections on the wall, which is visible in figure 4.3. During measurements this "reflective scattering" was visible. A mask, placed around the circumference of the cylinder, is applied to suppress this effect. However at some positions the effect is so strong that the particle reflection will be visible within the area where the mask is not applied, or the mask does not completely enclose the measurement circumference and the reflective scattering is visible. The effect occurs occasionally over the measurements and usually only influences one or two vectors. These vectors will point out of the circumference, which is physically impossible. However these effects will be averaged out in a average velocity plot. For comparison figure 4.5 shows a better correlating experiment.

Scattering is also the cause of the strange lightening on the left side of figure 4.3, the laser light scatters back from the inside circumference of the dummy cilinder and focusses on on point in the cylinder. Although this effect is present, it does not influence the measurements, as can been seen in figures 4.4 and 4.5. The effect is present in both measurements.

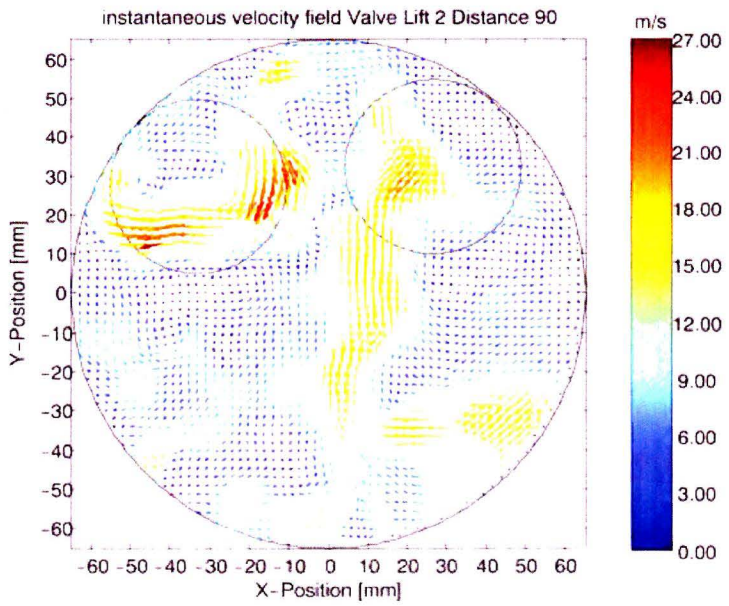

Figure 4.6: Instantaneous velocity field

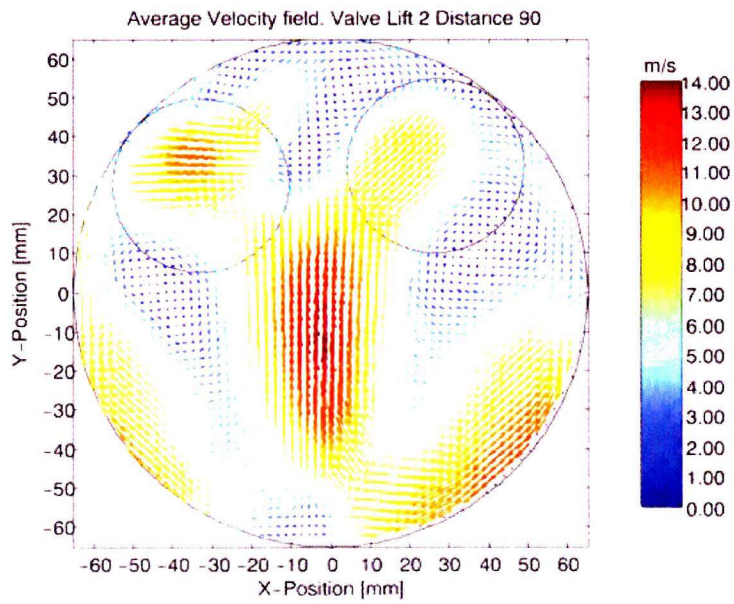

Figure 4.7: Average velocity field

Distance from cylinder-head = 90 [mm]. Valve-lift = 2 [mm]. Mass-flow = 50.5 $\left[\frac{g}{s}\right]$

4.2 Velocity field

The next step is to produce velocity fields. Two fields are of general interest the instantaneous velocity field which shows all the small structures present, and the averaged velocity field which illustrates the overall motion of the fluid.

To produce the instantaneous velocity the flag matrix is summed over the measurements, and the measurement containing the most reliable vectors is selected for representation. This measurement is cropped by the cylinder wall to obtain all vectors within the cylinder. Additional MATLAB plots the cylinder wall and inlet-ports for clarity. In figure 4.6 a specific instantaneous velocity field is shown. In this figure the eddies can clearly be distinguished, these eddies have a short lifetime than the timing between the two consecutive pairs (10 Hz) and thus fluctuate over all 500 measured pairs.

The average velocity field is constructed by summing all righteous vectors and dividing through the number of righteous vectors, in this way an average is created without the influence of absent false vectors. This is shown in figure 4.7. There are no small scale eddies in this figure, they are all averaged. The two counter-rotating vortices can be clearly seen.

4.2.1 Reynolds decomposition

Although the instantaneous field in figure 4.6 showed more small vortices than the average field in figure 4.7, not all vortices can been seen in an instantaneous velocity field; more vortices become visible after substraction of average velocity of the vortex. This method is called decomposition.

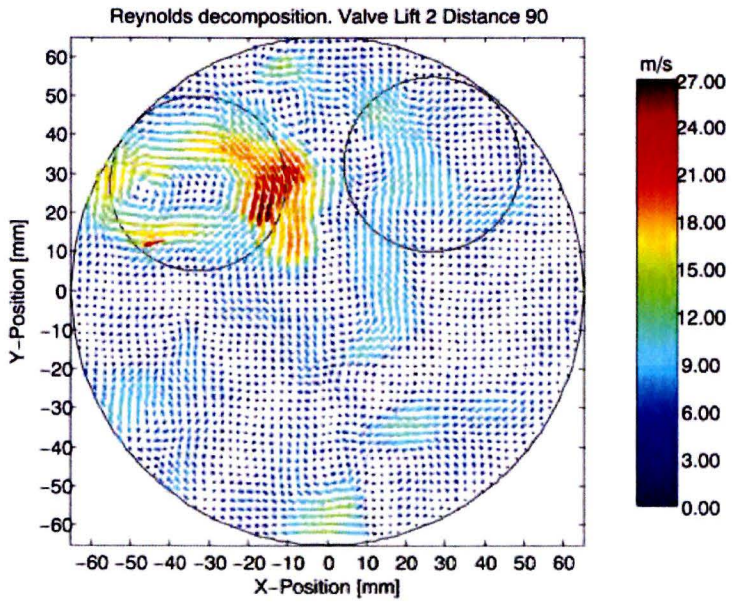

Figure 4.8: Reynolds decomposition

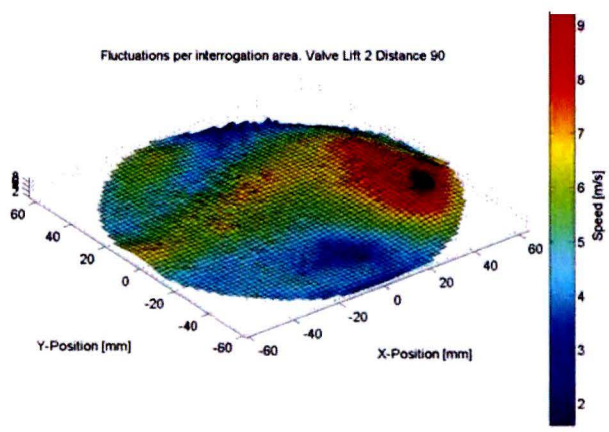

Figure 4.9: Average fluctuations

Distance from cylinder-head = 90 [mm], Valve-lift = 2 [mm], Mass-flow = 50.5 $\left[\frac{g}{s}\right]$

Decomposition by scale denotes separating the total vector field into portions having different scales of length or time. The Reynolds decomposition can be viewed as a scale decomposition in several ways, depending upon the definition of the average velocity [4]. If the average velocity is determined by long-time averaging (as is the case in this report), the decomposition separates the field into a (possible position dependent) component that has infinite time-scale and a fluctuation that contains all other components of lesser time-scale. By subtracting the average velocity field from the instantaneous velocity field these infinite time-scale components will be removed and the components of lesser time-scale will become visible. The resulting vectors are the fluctuating velocity vectors (u) as described in section 2.7

One of the strengths of Reynolds decomposition is its ability to reveal small-scale structures. The drawback of this method is that it removes large-scale features (mechanisms) that are intimately associated with the average flow. That is why the average velocity field is depicted in figure 4.7 and the Reynolds decomposition in figure 4.8.

4.2.2 Fluctuations

The fluctuating velocities extracted from the Reynolds decomposition tell how the flow fluctuates over time and space. By averaging these fluctuations over the number of measurements (500) information about the structures inside the cylinder can be extracted. The higher the fluctuations in the cylinder the more instable the flow will be at that position in the cylinder. Figure 4.9 shows these assembled fluctuations. Note that the fluctuation velocities are lower than the velocities in figures 4.6, 4.7 and 4.8, this is due to the fact that the fluctuating velocities are calculated by subtracting the average velocity and the instantaneous velocity, giving rise to smaller velocity components and this is due to the lower energy of the smaller vortexes.

With these fluctuations it is possible to determine the turbulence dissipation rate in the flow using formula 2.54. l is chosen as the valve-lift (2 mm) and u is the average fluctuation vector of the total measurement (3600x500 vectors averaged) resulting in:

$$\epsilon = \frac{u^3}{l} = \frac{5.5224^3}{0.002} = 8.4209 \cdot 10^4 \qquad \left[\frac{m^2}{s^3}\right] \tag{4.1}$$

This turbulence dissipation rate can in turn be used to find the smallest Kolmogorov length scale, using formula 2.51. The kinematic viscosity (ν) of air is $15.68 \cdot 10^{-6}$ $\left[\frac{m^2}{s}\right]$.

$$\eta = \left(\frac{\nu^3}{\epsilon}\right)^{\frac{1}{4}} = \left(\frac{(15.68 \cdot 10^-6)^3}{8.4209 \cdot 10^4}\right)^{\frac{1}{4}} = 1.4627 \cdot 10^-5 \qquad [m] \tag{4.2}$$

The Kolmogorov length scale this measurement (valve-lift = 2 mm, distance from the cylinderhead is 90 mm and mass flow = 50.5 $\left[\frac{g}{s}\right]$) is thus 14 μm. This number is in the same order as Lumley [32] states (section 2.7). Formula 4.1 indicates that as fluctuations become larger, the Kolmogorov scale decreases.

4.2.3 POD and SVD

Proper Orthogonal Decomposition (POD) extracts dominant structures from a given ensemble [21]. When the number of collected samples is smaller than the space discretization, it is more convenient to use the Sirovich approach [41] also known as method of snapshots. The ensemble can be either generated by detailed numerical simulations or collected experimentally [9].

POD provides an optimal set of basis functions for an ensemble of data. It is optimal in the sense that it is the most efficient way of extracting the most-energetic components of an infinite-dimensional process with only a few modes [21]. In POD the fluid variables are written as a linear combination of some global modes. These global modes are computed by taking snapshots of the time history data of the fluid variables, putting them in a matrix, forming a spatial correlation matrix and then computing the eigenvalues/eigenvectors of the correlation matrix. Alternatively you can computed the POD modes by performing an SVD on the matrix of snapshot data. SVD itself is just a way to decompose a matrix. Since SVD is a commando in MATLAB this will be used to determine the eigenvalues of the assembled fluctuation matrix.

If the fluctuations are given as a data set $u_k(x)$ where x is the space coordinate and k is the snapshot index. Such a set can be conveniently represented as a matrix $U = u_{jk}$ where j = 1,...,M spans the number of space positions and k = 1,...,N spans the number of snapshots u_k. Than it is possible to build a set of modi [7]:

$$\Phi = \{\varphi_1, \varphi_2, ..., \varphi_N\}, \tag{4.3}$$

of linear combinations of the snapshots:

$$\varphi_i(x) = \sum_{k=1}^{N} \psi_{ik} \cdot u_k(x), \tag{4.4}$$

where $\Psi = \psi_1, \psi_2, ..., \psi_N$ is obtained by solving the eigenvalue problem $C\Psi = \lambda\Psi$, C being the space correlation matrix:

$$C = \frac{1}{N} \cdot U^T \cdot U, \tag{4.5}$$

Then the snapshot (u_k(x)) can be approximated by a linear combination of K modes:

$$\tilde{u}_k = \sum_{i=1}^{K} c_{ik} \cdot \varphi_i(x), \tag{4.6}$$

where K is the number of vectors used in the measurement, whereas c_{ik} are POD coefficients that can be determined by projection of the data ensemble onto the POD modes [7].

The eigenvalues determined by the SVD commando (or the squares of the singular values) are sometimes referred to as 'energies' corresponding to the proper orthogonal modes. In this research, where the fluid is considered incompressible, this energy is related to the fluid's kinetic energy.

The POD coefficients that are extracted by this method can be used to plot several modes of the flow. The first four modes of the instantaneous field in figure 4.6 are depicted in figures 4.12 - 4.15. Accordingly it is possible to determine the energy per mode of the instantaneous field. This graph is represented in figure 4.10. Mode 1 carries 43% of the total energy in this instantaneous field. while mode 2, 3 and 4 respectively carry 6.18%, 4.02% and 2.84% of the total energy present in the filed. 90% of the cumulative energy is preserved within the first 60 modes.

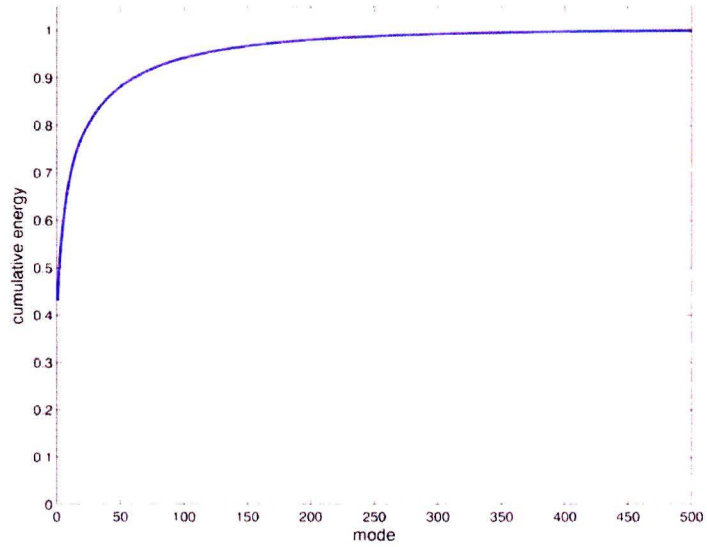

Figure 4.10: Cumulative energy per mode

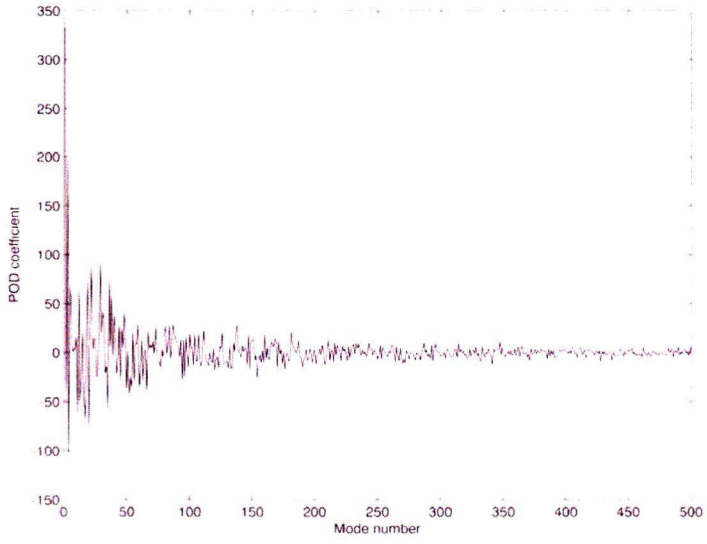

Figure 4.11: POD coefficients of the instantaneous field

Distance from cylinder-head = 90 [mm]. Valve-lift = 2 [mm]. Mass-flow = 50.5 $\left[\frac{g}{s}\right]$

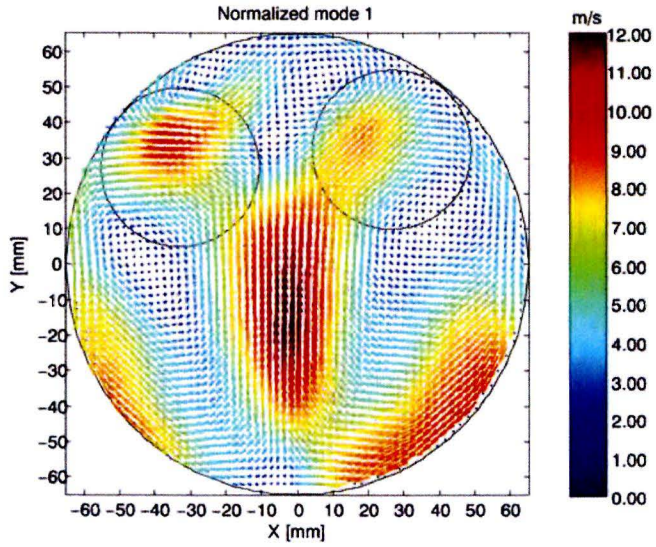

Figure 4.12: Normalized mode 1

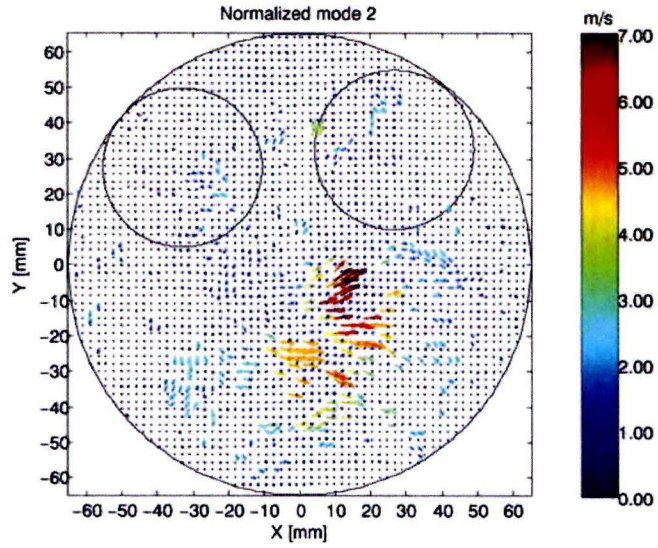

Figure 4.13: Normalized mode 2

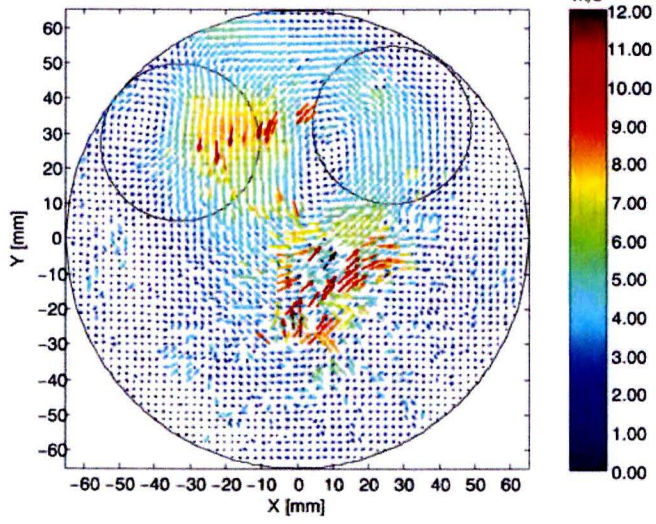

Figure 4.14: Normalized mode 3

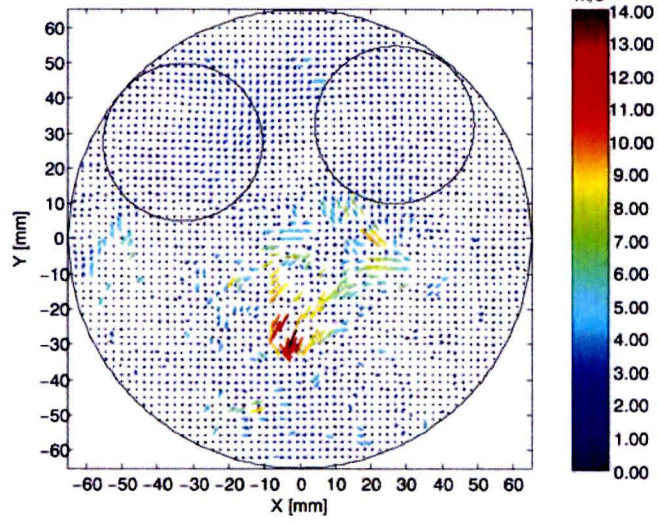

Figure 4.15: Normalized mode 4

Distance from cylinder-head = 90 [mm], Valve-lift = 2 [mm], Mass-flow = 50.5 $[\frac{g}{s}]$

4.2.4 Justification disregarding outliers

To justify the disregarding of outliers, instead of interpolating, a comparison is made. The worst measurement is selected and analyzed with and without interpolation. The results of both methods are plotted in figures 4.16 - 4.19 and differ quite severe. First the method used in this report will be explicated.

In this report the multi-grid correlation is used, which progressively scans the PIV images in decreasing interrogation windows. The method starts at a 128 x 128 pixel and progresses to 96 x 96 pixels and finally 64 x 64 pixel interrogation. Whenever this correlation technique is unable to find a correlation peak it re-evaluates the previously evaluated interrogation window and tries to find if there is a matching correlation peak. If the correlation peak matches, the vector is considered as valid data. When there is no conformity between the peaks in the small and larger interrogation window, the interrogation scheme considers the vector, inside the final interrogation window, as an outlier. In this report, these outliers are disregarded, since they are not reliable because they cannot be correlated correctly.

On the other hand there is the possibility of interpolating these outlier vectors, the multi-grid correlation technique is still used, but without re-evaluating. This interpolation applies a bi-linear interpolation over its eight neighbors to estimate the replacement vector. All correlating vectors are exported as valid data while the replacement vectors are exported as interpolated vectors. The reason for interpolation is to obtain more smooth vector fields, basically the missing data is filled in by using the neighboring vectors to estimate the missing vector. Various correlation based methods of interrogation, combined with Gaussian sub-pixel interpolation, are commonly used and with some exceptions continue to show significant effects of peaklocking [43].

To make a comparison between the two methods, the worst correlating measurement was chosen. In the case of replacing the vectors, if possible, by a re-evaluation of the previous interrogation window, all vectors flagged valid data were used. This were in total 1258924 vectors out of 1800000 vectors (3600 vectors x 500 measurements) corresponding to 69.94%. 11.17% of the vectors was considered as an outlier and 18.89% was lost due to the mask application. In this case 69.94% of the vectors (the valid data) was used to ensemble an average velocity field. The 18.89% of data lost by the mask is not used in the calculation of the average velocity field, therefore effectively 86.23% of the vectors used for average velocity calculation are valid and 13.77% are outliers. The average velocity field is thus constructed using 86.22% of the vectors in the test section (inside the mask).

In the case of replacement of outliers by interpolation 1203061 vectors out of 1800000 were considered as valid data, corresponding to 66.84%. 14.26% of the vectors was interpolated and 18.90% was lost due to the mask application. In this case 81.1% of the vectors was used to ensemble an average velocity field. However the vectors outside the mask are disregarded, this means that all vectors inside the mask 100% of the vectors are used to ensemble the average velocity field.

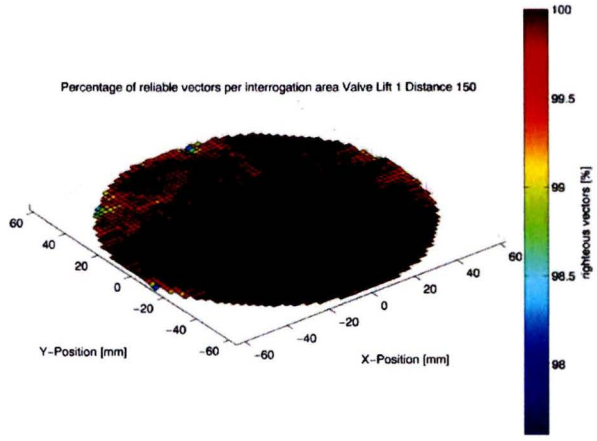

Figure 4.16: Quality plot with interpolated outliers

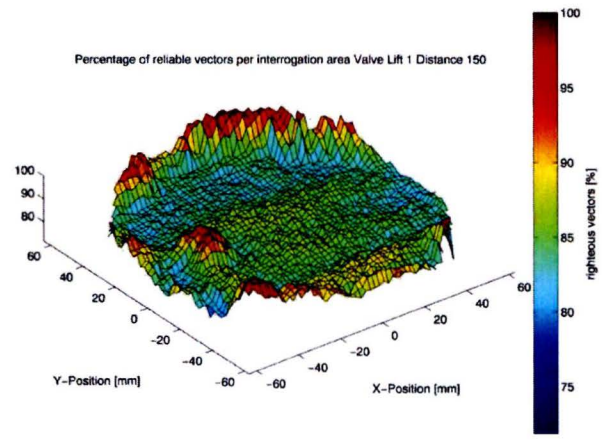

Figure 4.17: Quality plot with disregarded outliers

Distance from cylinder-head = 150 [mm], Valve-lift = 1 [mm], Mass-flow = 32.2 $\left[\frac{g}{s}\right]$

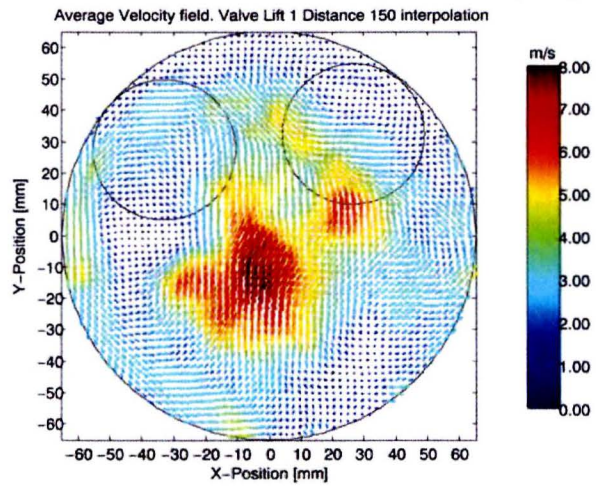

Figure 4.18: Average velocity plot with interpolated outliers

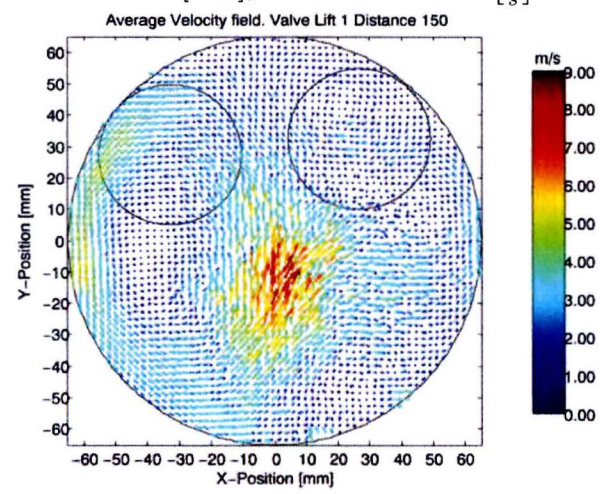

Figure 4.19: Average velocity plot with disregarded outliers

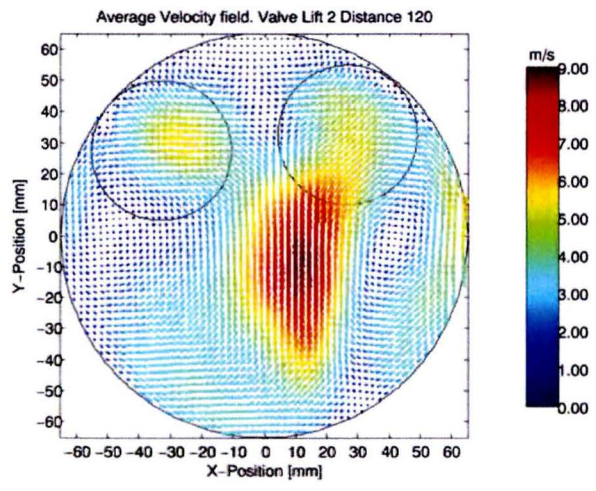

Figure 4.20: Average velocity plot with interpolated outliers

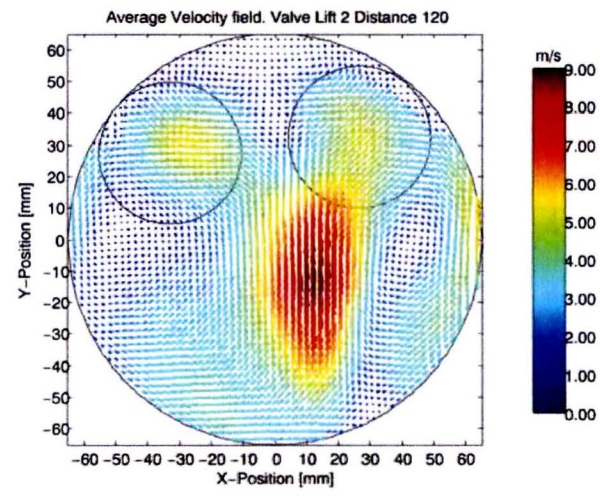

Figure 4.21: Average velocity plot with disregarded outliers

Distance from cylinder-head = 120 [mm], Valve-lift = 2 [mm], Mass-flow = 51.9 $\left[\frac{g}{s}\right]$

Figure 4.16 and 4.17 show respectively the quality of the interpolated outliers correlation and the disregarded outlier correlation. The quality of the interpolated outliers is better since the interpolated outliers are regards as reliable vectors. thus increasing the number of reliable vectors with respect to figure 4.17.

Figure 4.18 and 4.19 show respectively the average velocities of both correlations. The average velocity field of the interpolated vectors is smoother, due to the fact that 17.58% of the vectors is "smoothed" due to the interpolation. Although figure 4.19 shows a different same flow structure than figure 4.18 the averaged velocities, respectively 2.1992 $\left[\frac{m}{s}\right]$ and 2.1733 $\left[\frac{m}{s}\right]$ only differ less than 1%.

For illustration purposes the worst measurements (fluctuations are high in this measurement) in this research is shown. In other measurements the difference between quality plots and average velocity is less significant (as can been seen in figures 4.20 and 4.21. Although figure 4.18 shows a more smoothen velocity field, the vectors in figure 4.19 are actually measured and correlated, instead of interpolated. The goal of this research is to obtain good in-cylinder velocity data, and by that goal outliers are thus disregarded instead of interpolated.

4.3 General results of the tangential measurements

In this research two variables were changed, the distance from the cylinder-head and the valve-lift. The distance inwards the cylinder was measured with respect to the face of the cylinder-head and was in the range of 30 mm to 160 mm. The valve-lift was varied from 1 mm to 5 mm. In all, the changes in these variables yielded 65 velocity fields. It is beyond the scope of this report to show all the velocity fields obtained (a set for one valve-lift is shown in appendix E). Instead general characteristic variables are determined for each velocity field and they will be plotted for different valve-lifts and distances from the cylinder-head.

The variable of most interest is the average velocity in the tangential plane over the cylinder at different valve-lifts. Figure 4.22 shows the average velocity over distance from the cylinder-head for different valve-lifts. The average tangential velocity increases with distance from the cylinder-head till it peak around 60 mm from the cylinder-head. At higher valve-lifts the mass flow is higher and thus the average tangential velocities are higher as can been seen in figure 4.22.

This increase in tangential velocity can be explained by the tangential inlet ports of the Proteus cylinder-head shown in figure 2.4 and 2.5 in section 2.2.1. To accommodate the valve and valve stem the intake port is shaped rather steeply at the end of the port. A possible explanation for the increase in tangential velocity from 30 mm to 60 mm might lie in this design. The intake flow is given a tangential momentum by the intake runners, but is directed into the cylinder axially. The flow expands in the cylinder reducing in axial velocity, giving rise to the tangential momentum and starts "swirling". Apparently this momentum peaks at around 60 mm from the cylinder-head and tend to rapidly decay from there onwards.

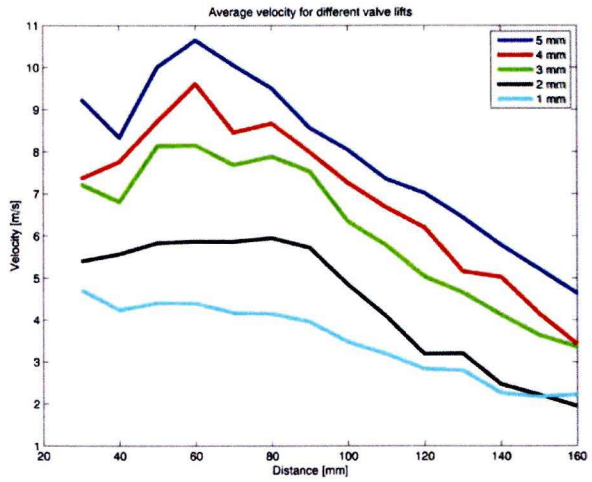

Figure 4.22: Average Velocity

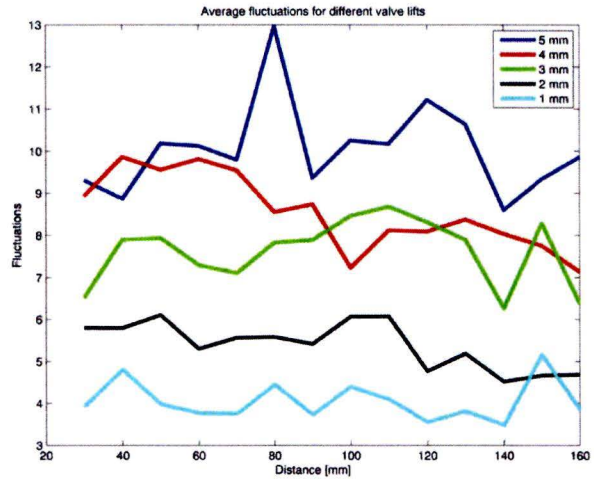

Figure 4.23: Fluctuations

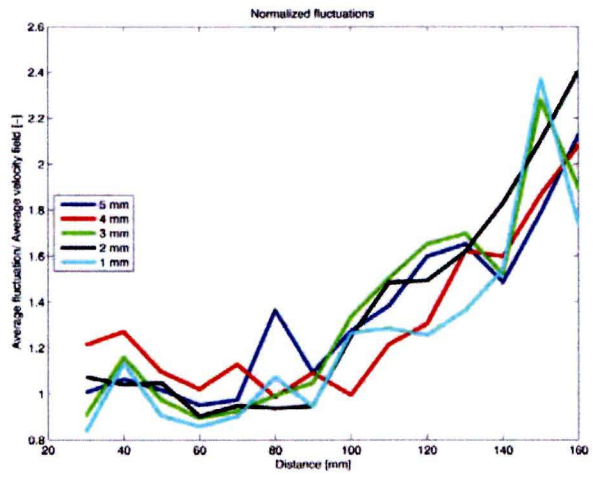

Figure 4.24: Normalized fluctuations

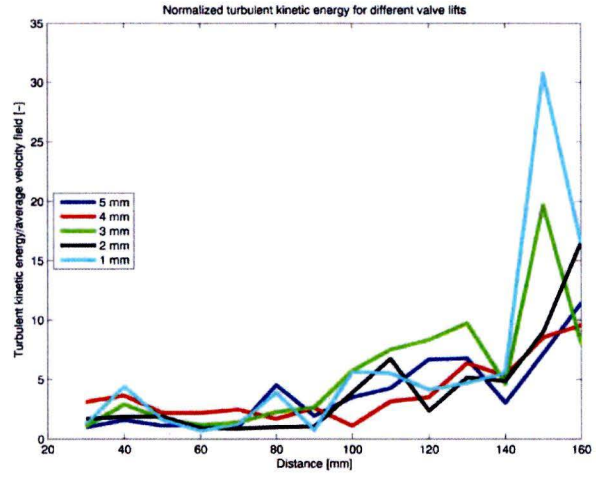

Figure 4.25: Normalized TKE

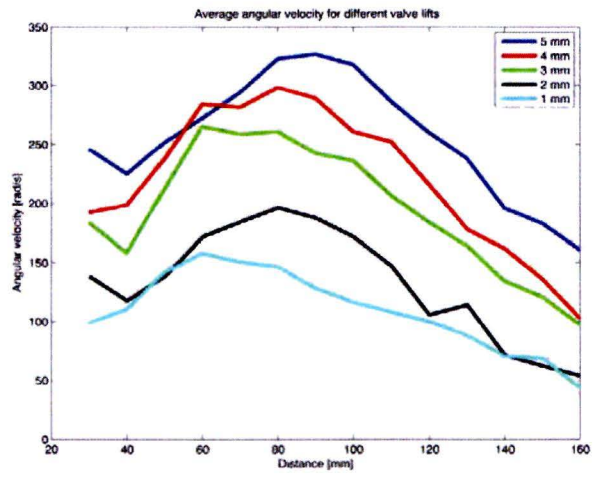

Figure 4.26: Angular velocity

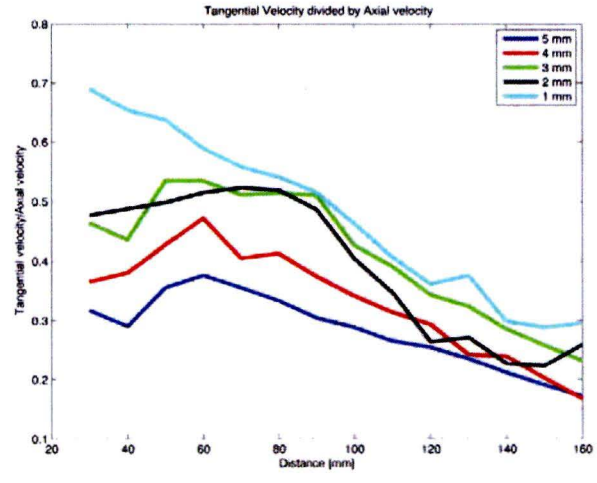

Figure 4.27: Ratio of tangential/axial velocity

Another explanation lies within the actual valve design. The valve has an angle to improve the sealing of the intake port when the valve is closed. This seat angle Ψ might direct the axial flow into the cylinder towards the cylinder walls. When the flow (jet) impacts the cylinder wall it might give rise to increased tangential velocities. However if this was the case the average velocity in figure 4.22 would show a distinct peak at a certain distance from the cylinder-head. Instead the course of the average velocity over distance seems more gradual and thus increases the credibility of the first statement. To completely disqualify the jet theory, the fluctuations over distance from the cylinder-head are plotted in figure 4.23. If the jet would impact the wall this figure would show distinct fluctuations for all valve-lifts at certain positions (the distance of the jet impact would shift with valve-lift). However the fluctuations do not evidence this theory.

Although the fluctuations in figure 4.23 do not demonstrate any trends, if these fluctuations are normalized with the average velocity, trends are appearing shown in figure 4.24. The fluctuations increase with the distance from the cylinder-head. Fluctuations are defined as the difference between the average velocity field and the instantaneous flow fields. The average velocity field describes the main vortex in the tangential plane. When fluctuations increase, instantaneous velocity fields no longer resemble the average velocity field, indicating that the structures present in the instantaneous velocity fields are highly inhomogeneous. In other words, as distance from the cylinder-head increases, resemblance between the individual instantaneous velocity fields decreases. In fluid dynamic perspective this is a strong indication that main flow structures are breaking up into smaller flow structures. Coherent structures break-up and form in-coherent structures.

In literature the term Turbulent Kinetic Energy (TKE) is frequently used to describe these fluctuations [19] [44]. Although the term TKE implies an energy its unit is $\left[\frac{m^2}{s^2}\right]$, indicating that it is just a squared velocity. This TKE should actually be measured in 3D, PIV misses one component and therefore the following definition of TKE is given:

$$TKE = \frac{1}{N}\sum_{i=1}^{N}\frac{1}{2}\left[(U-\bar{U})_i^2 + (V-\bar{V})_i^2\right] \qquad \left[\frac{m^2}{s^2}\right] \tag{4.7}$$

Note that $(U-\bar{U})^2$ was defined as the fluctuation in section 2.7.

TKE can be used to depict the cascade of vortices within a flow field. This cascade of vortices breaking up into ever-smaller vortices was elaborated in section 2.7. Although the normalized fluctuations and normalized TKE show similar results, TKE is depicted in figure 4.25 for completeness. Both variables increase from 90 mm onwards.

The average velocity as depicted in figure 4.22 is a good variable to indicated the magnitude of the velocities contained in the vector field at a certain distance from the cylinder-head. However this variable has little to no value when referring to swirl. Swirl is an axisymmetric rotation which can hardly be captured in a cartesian coordinates system. The average velocity is calculated by averaging all velocities, indicating that two opposite equally-length vectors cancel each other out in this calculation, while it is quite possible that these two vector give rise to a momentum about an axis.

To obviate this problem, the cartesian coordinates system in which the velocity vectors were obtained was converted to a polar coordinate system. Polar coordinates allow for the calculation of angular velocity, using the formula:

$$\omega = \frac{|v| \sin\theta}{|r|}, \qquad \left[\frac{rad}{s}\right] \tag{4.8}$$

with v the length (magnitude) of the vector, θ the angle between the vector and a fixed direction and r the radius from the center of the system to the base of the vector.

The angular velocity at each distance from the cylinder-head can be calculated using formula 4.8 as shown in figure 4.26. The angular velocity peaks around 80 mm from the cylinder-head and decays from that distance onwards. The difference between the average velocity and angular velocity is noticeable, although they both decay at larger distances from the cylinder-head, there peaks are different and also their magnitudes. The highest average velocity in figure 4.22 is 10.6 $\left[\frac{m}{s}\right]$ while the highest angular velocity is 326.6 $\left[\frac{rad}{s}\right]$ which at a radius of 0.065 [m] (radius of the cylinder) represents 21.2 $\left[\frac{m}{s}\right]$.

One other parameter is of interest, the relation between the average velocity in tangential direction versus the average velocity in axial direction. The average velocity in axial direction can easily be determined by dividing the mass flow through the cylinder-head by the area of the cylinder. The relation between the average axial and tangential velocity is shown in figure 4.27. Bigger valve-lift lowers the ratio of average tangential velocity compared to the average axial velocity. In other words as valve lift increases average axial velocity becomes more dominant than average tangential velocity.

4.4 Axial measurements

To visualize the axial flow structures, the camera was positioned directly above the dummy-cylinder and the laser-sheet was shot parallel to the camera (through the cyclone). This configuration was chosen since scattering tends to be higher if the camera and laser shoot though the same glass surface. This configuration also allowed for a larger area to illuminated by the laser. Unfortunately the camera was not able to record this large area and thus the area was reduced (see figures 4.1 and 4.2).

The velocity fields at two axial planes were investigated, a plane which was positioned in the middle of the cylinder and a plane which was positioned at the middle of valves. The vector fields are plotted in figures: 4.28 - 4.33 these planes are respectively called axial cylinder and axial valves. The results plotted here are representative for other valve-lifts. Note that the vectors in the average velocity plot in figures 4.30 and 4.31 are plotted with a greater scale (4 times bigger) to obtain better visualization of the flow structures. Only the length of the vector is stretched not their magnitude.

In axial direction the main flow structure is a jet. The jet induces tumbles clearly seen in figure 4.30 at the left side of the plot ([67,-15] and [62,12]). In figure 4.31 they can also be observed in the left side of the picture([80,-5] and[63,10]).

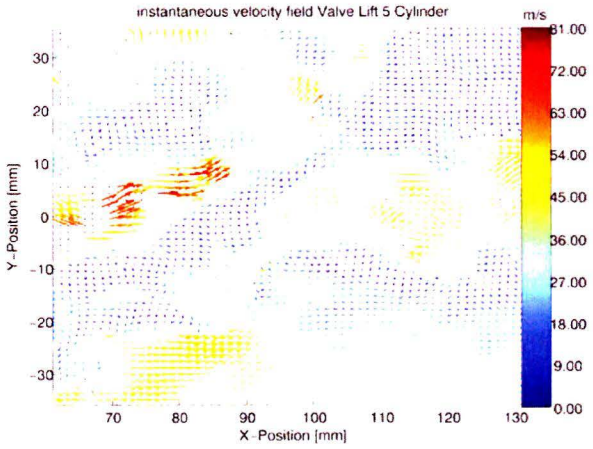

Figure 4.28: Instantaneous field axial cylinder

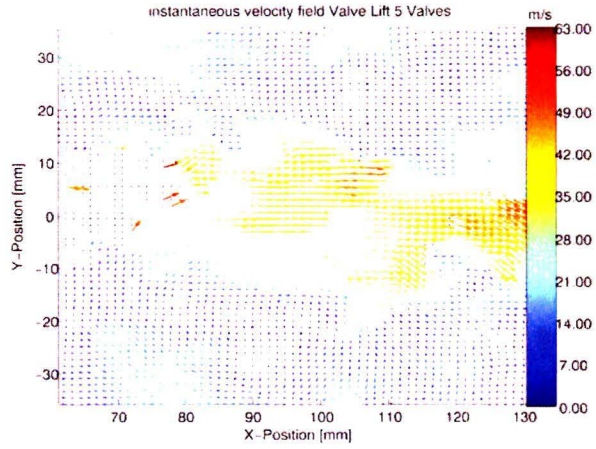

Figure 4.29: Instantaneous field axial valves

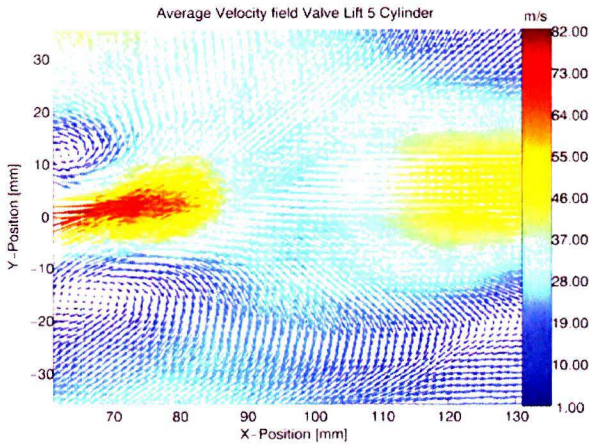

Figure 4.30: Average velocity axial cylinder

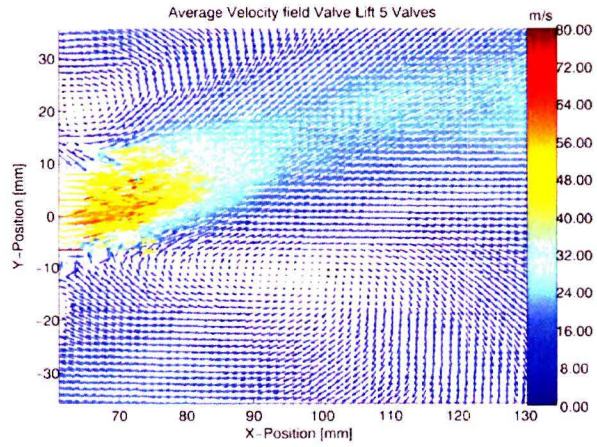

Figure 4.31: Average velocity axial valves

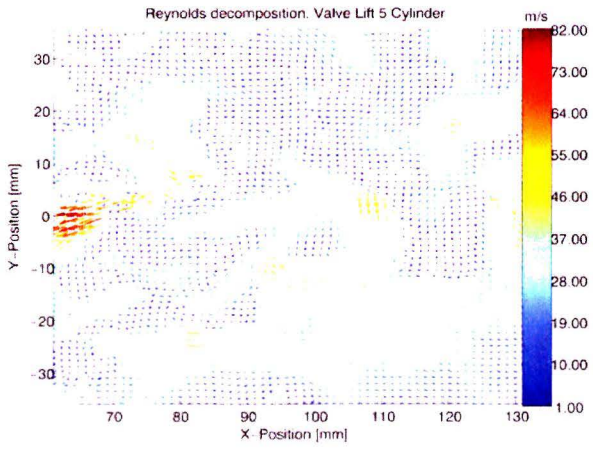

Figure 4.32: Reynolds decomposition axial cylinder

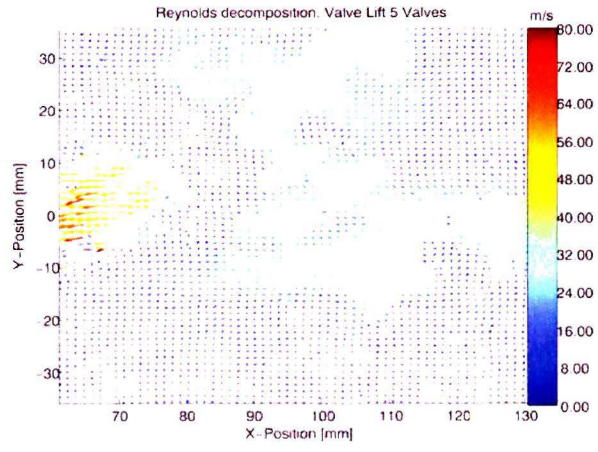

Figure 4.33: Reynolds decomposition axial valves

The jet breaks up rather quickly after it enters the cylinder, as can been seen in figures 4.28 and 4.29, where no clear jet is visible. However it should be noted that valve-lifts were small in this experiment and the distance from the cylinder-head is considerable. At higher valves lifts or/and closer to the cylinder-head a more distinctive jet might be observed.

Chapter 5

Conclusions

The constructed flowbench is well suited to preform PIV measurements of fluctuating flows with in the dummy-cylinder. The flow-structures inside the cylinder were visualized for 5 valve-lifts at 13 distances from the cylinder-head. Average velocity field, instantaneous field and Reynolds decompositions were obtained with a spatial resolution of 2.1 [mm].

The PIV pairs were correlated with PIVview using a64 x 64 pixel interrogation window with 75% overlap. A mask to isolate the area of interest. The image was enhanced using a dynamic treshold of 10% - 97% and a anti-alias filter. The pairs were correlated using the multi-grid correlation, were re-evaluation was done with a bigger interrogation window to obtain more valid vectors. Vectors that had a peak 1 - peak 2 ratio of less than 2 or had a normalized mean filter threshold lower than 3 were regarded as outliers. These outliers were not interpolated but disregarded resulting in 10% vector loss. This decision was taken, since the difference between interpolation and disregarding the outliers was less than 1%. The consensus is that disregarding the outlier produces a more reliable result than interpolation.

The obtained vector fields in PIVview were further analyzed using MATLAB, all results presented in this report are output of MATLAB. The visualizations obtained showed that initially the flow enters the cylinder axially, after which a tangential motion sets in. This tangential motion (swirl) peaks around 60 [mm] from the cylinder-head and decays from there on. At a distance of 100 [mm] the flow begins to break up and fluctuations become higher. Turbulent Kinetic Energy also rises at this state indicating that the flow structures are dissipating. A pattern of two counter-rotating vortices exists with in the flow.

Axial measurements showed that a jet was present from the valves into the cylinder. This jet induced two tumbles on both sides of the jet. Although the jet was present in the average velocity field, instantaneous fields proved that the jet broke up rather quickly.

Chapter 6

Discussion & Recommendations

To give insight into the daily practices of running PIV experiments, some of the difficulties are explained within this chapter and recommendations are given for further research.

6.1 Bleed valve

The bleed valve was installed for security reasons, to prevent the setup from overpressure. However after installation the bleed valve was checked and the setup was pressurized. The cylinder-head houses 12 inlet valves, and during the pressurized tests at 2.5 bar(g) all inlet valves started to leak. Indicating that the pressure was escaping over the inlet valves instead of over the bleed valve. This means that the setup is secured against over pressure but that the bleed valve currently installed does not have an active function and could be removed.

6.2 Scattering

Scattering is the reflection of light and although this is a wanted effect in PIV, scattering of parts other than the seeding disturb the measurement. The optical inlet tube showed extensive scattering during initial measurements. In fact scattering was so intense that no further PIV measurements were done of the inlet.

When light impinges on a glass surface, most of the light will pass through the glass, but some (5%) will reflect in arbitrary directions. The problem of the optical inlet tube, lies within its design The glass windows are rectangular and flat to fit the geometry of the tubing. In PIV the camera is positioned perpendicular to the laser-sheet, so in a rectangular array of glass, the reflections of the laser sheet are more likely to impinge on the glass at which the camera is focussed, thus deteriorating the images shot. The problem can been seen in figure 6.3.

To solve this problem, masking the glass with tape to reducing scattering (figure 6.2 was tried as well as painting some parts of the glass. However both methods reduce the measurement area, and therefore non of the solutions were practical. Another option that was tried was to dope the seeding. There are commercially available dopes that can be added to the seeding and will scatter a slightly shifted wavelength when the are illuminated by laser-light of a certain wavelength. When a filter is applied to the camera the shifted wavelength is visible

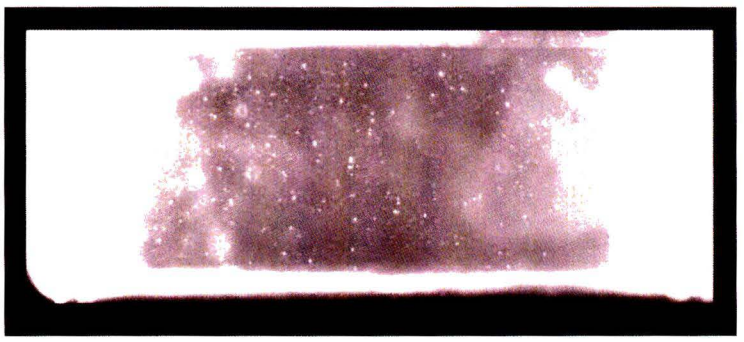

Figure 6.1: Scattering optical inlet

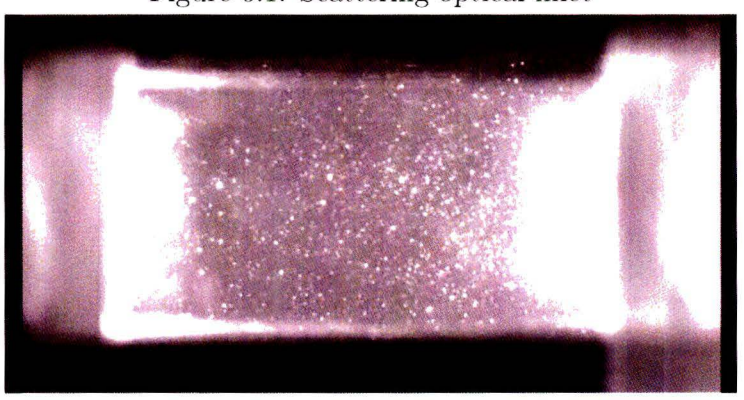

Figure 6.2: Scattering with tape

Figure 6.3: Swirl torque TU/e

while the original wavelength is suppressed and thus the scattering is suppressed. However both silicon oil and DEHS proved not to mix with the dope and therefore doping was not an option.

6.3 Leakage

Although all parts are sealed by rubber gaskets, leakage is still present in the setup. Two parts are responsible for this leakage, the optical inlet channel and the cyclone. Of these two part the optical inlet tube is the most critical one, since it is located downstream of the measurement area.

Inside the optical inlet tube, four miter glass pieces are positioned, as can been seen in figure 3.3. The windows of this part needed to be large enough to visual the entire inside length (100 mm) of the channel. This ment that the miter angles of the glass would allow for little insulation between them. Hard contact between the glass needs to be avoided to be able to position the glass inside the part and to reduce laser scattering within the glass. The gap between the glass windows was therefore chosen 1 mm and was sealed with a small liner (0.5 mm) of silicon kit. Although this kit should seal the glass from leakage, testing with soapy water proved that the optical inlet tube was leaking.

The cyclone is constructed with a plate on top of it which contains a glass window that allows optical access. When this plate is removed the dummy-cylinder is accessible, for cleaning and modification. The frequently disassembling of this plate and the bad design of it, caused it to leak. Many modifications have been made to this part to improve its sealing: the plate and cyclone were flattened to ensure better sealing, a slot was milled into the plate and filled with silicon rubber and insulation to further ensure sealing and new clamps were positioned. Although all of the methods increased the sealing, leakage is still present.

6.4 Errors in PIV acquisition

Laser

The laser provided for this research did not meet the requirements needed for these flows. The laser energy per pulse was low, to compensate this problem the laser sheet was chosen as thin as possible. This choice resulted in smaller timing between the frames, due to the fact that the out-of-plane velocity was higher than the in-plane velocity. This resulted in very small pixel displacements over the pictures. Although PIV correlation is best when pixel displacement is between 4 - 8 pixels, the laser pulse energy, high axial velocity and thin laser sheet limited this research to displacement of around 1 - 2 pixels.

The reduced laser energy imposed another problem, the f-number of the camera has to remain small to obtain enough scattering. This did not compromise the focal depth since the laser sheet itself was chosen very thin, but it did compromise the particle image diameter d_{dif}. The f-number chosen in this research is 2.0 resulting in a particle image diameter of 2.772 μm (see figure 2.12), while the pixels of the camera are only 9 μm. Thus the particles are smaller than a pixel, giving rise to peak-locking. To accommodate for this phenomena the anti-alias filter was used, this gave satisfactory results.

Video savant

To record the images the Videosavant software was used. However this program is not very convenient and it make a slight mistake every now and that resulting in outliers. This error was randomly present throughout the measurement but was suppressed by the share volume of image pairs shot (500). Although these outliers were not used in further analysis they do suppress the quality of the images.

6.5 Error in analysis

Section 4.3 shows averaged velocity, normalized fluctuation, normalized TKE, angular velocity and ratio of tangential velocity of axial velocity. However the values presented there are means obtained and derived from the initial measured velocity field. This velocity field is a 3600 by 500 matrix, which is manipulated to obtain the wanted data and consequently averaged to obtained the variables. However, this velocity field is measured 500 times, with 100 milliseconds between two consecutive pairs. The nature of the flow and the large time between the two consecutive pairs ensure that the data is statistically incoherent.

Table 6.1: Standard deviation on mean values

Valve lift	**1 [mm]**	**2 [mm]**	**3 [mm]**	**4 [mm]**	**5 [mm]**
Mean $\left[\frac{m}{s}\right]$	4.162	5.865	7.686	8.461	10.05
Standard deviation $\left[\frac{m}{s}\right]$	3.160	2.140	5.940	8.487	3.405

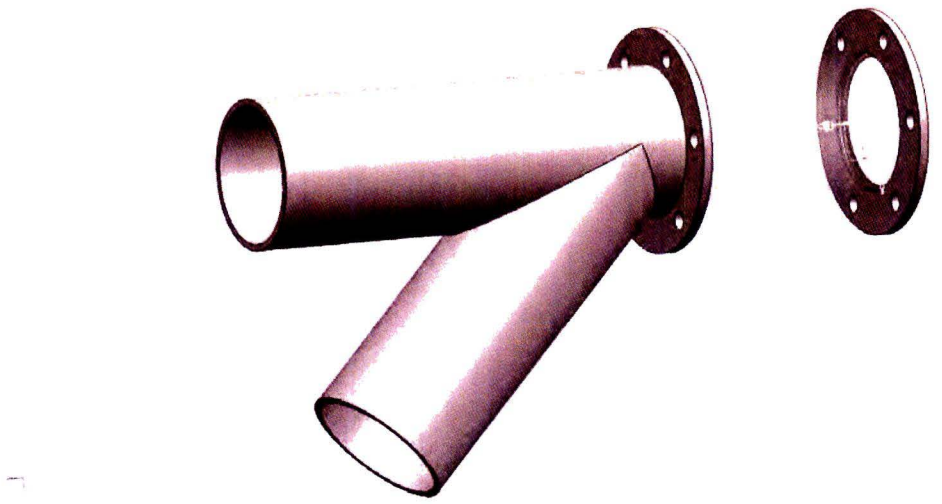

Figure 6.4: New outlet design

The average values presented in section 4.3 all have very high standard deviations table 6.1 shows an example for the velocity at several valve-lifts at 70 [mm] from the cylinder-head.

These standard deviations make the presented figures less reliable. However these standard deviations will contaminate any slow-PIV measurement. A solution could be to try high-speed PIV the time resolution would increase and thus velocities would change lesser over the measurements increasing the statistic reliability.

6.6 Outlet

A new outlet design could solve two problems which are currently present within the setup. Firstly the rubber sealing ring currently positioned between the glass dummy-cylinder and cylinder-head seals the dummy-cylinder. but could possibly disturb the flow. Secondly the cyclone is currently leaking and is not designed to work at elevated pressures. These problems could be solved with a new design. shown in figure 6.4.

The outlet is constructed of 2 plates of 10 [mm] PVC. A cavity of with the bore of the cylinder is drilled in the middle. Allow free passage of the flow. Around this cavity a second cavity will be milled. which has the same diameter as the outer diameter of the glass dummy-cylinder. This cavity will be only 8 [mm] in order for the glass to rest on the PVC instead of on the metal of the cylinder-head. The 8 [mm] edge of this second cavity will allow for an O-ring to be placed inside for sealing.

Two of these plate can be manufactured and the dummy-cylinder can be clamped between these two plates. On the exit-plate a pvc Y-piece can be attached which has roughly the same diameter as the glass cylinder (these are commercially available). Calculations by Hans van Griensven show that a round glass piece of 15 [mm] could withstand 3 bar(g) of pressure. This glass piece can be installed in the straight pipe to obtain visible access to the cylinder-head. On the oblique pipe of the y-piece a valve can be installed to throttle the pressure inside the dummy-cylinder.

This design seals better and does not disturb the flow. The design is better capable of pressure measurements due to the reduced glass surface. During this research there was sadly not enough time to finish this new design.

6.7 Stereoscopic PIV

Stereoscopic PIV is a method which allows for two camera to focus on the laser sheet. With two pais of the same particles shot at a different angle it is possible to obtain the third component. Basically stereoscopic PIV is a sort of 3D method. This could possibly allow for better swirl torque determination as well as three dimensional patterns, turbulence and fluctuations could be obtained.
Using the cameras the classical way, looking through the cyclone, would not work, the angle between the cameras would be to small. Therefore it would be preferred to elongate the dummy-cylinder and to place the cameras besides the dummy-cylinder.

Bibliography

[1] 9th International Symposium on Applications of Laser Techniques to Fluid Mechanics,. *The Elimination of Correlation Errors in PIV Processing* (Lisabon, July 1998).

[2] Adrian, R. J. Image shifting technique to resolve directional ambiguity in double-pulsed velocimetry. *Applied Optics 25*, 21 (1986), 3855–3858.

[3] Adrian, R. J. Dynamic ranges of velocity and spatial resolution of particle image velocimetry. *Measurement Science and Technology 8*, 12 (1997), 1393–1398.

[4] Adrian, R. J., Christensen, K. T., and Liu, Z.-C. Analysis and interpretation of instantaneous turbulent velocity fields. *Experiments in Fluids 29*, 3 (2000), 275–290.

[5] Adrian, R. J., and Keane, R. D. Optimization of particle image velocimeters part 1: Double pulsed systems. *Measurement Science and Technology 1*, 11 (1990), 1202–1215.

[6] Bensler, H., Kapitza, L., Raposo, J., and Reisch, U. A new experimental method for determining port generated swirl flow. *SAE Technical Paper Series*, 2002-01-2846 (2002).

[7] Bizon, K., Continillo, G., Mancaruso, E., Merola, S., and Vaglieco, B. Pod-based analysis of combustion images in optically accessible engines. *Combustion and flame 157*, 4 (2010), 632–640.

[8] Doosje, E. Piv-karakterisering van uitgaande swirlstoming bij een stationair doorgeblazen heavy-duty cilinderkop. Graduation report, Eindhoven University of Technology, December 2001. Confidential.

[9] Druault, P., and Chailloua, C. Use of proper orthogonal decomposition for reconstructing the 3d in-cylinder mean-flow field from piv data. *Comptes Rendus Mcanique 335*, 1 (2006), 42–47.

[10] Duncan, J., Dabiri, D., Hove, J., and Gharib, M. Universal outlier detection for particle image velocimetry (piv) and particle tracking velocimetry (ptv) data. *Measurement Science and Technology 21*, 5 (2010), 1–5.

[11] Epping, K., Aceves, S., Bechtold, R., and Dec, J. The potential of hcci combustion for high efficiency and low emissions. *SAE Technical Paper Series*, 2002-01-1923 (2002).

[12] Fajardo, C., and Sick, V. Development of a high-speed UV particle image velocimetry technique and application for measurements in internal combustion engines. *Experiments in fluids 46*, 1 (2008), 43–53.

[13] Filter Integrety Ltd. Plg series - laskin type nozzle liquid aerosol generators. http://www.filterintegrity.com/PTAS/PandS/Products/LiquidPartGen/plgmain.html.

[14] Flynn, P. F., Hunter, G. L., Durrett, R. P., Farrell, L. A., and Akinyemi, W. C. Minimum engine flame temperature impacts on diesel and spark-ignition engine no_x production. *SAE Technical Paper Series*, 2000-01-1177 (2000).

[15] Gray, C., Greated, C. A., McCluskey, D. R., and Easson, W. J. An analysis of the scanning beam PIV illumination system. *Measurement Science and Technology 2*, 8 (1991), 717–724.

[16] Hain, R., Khler, C. J., and Tropea, C. Comparison of ccd, cmos and intensified cameras. *Experiments in Fluids 42*, 3 (2007), 403–411.

[17] Hart, D. P. Piv error correction. *Experiments in Fluids 29*, 1 (2000), 13–22.

[18] Heywood, J. B. *Internal Combustion Engine Fundamentals*. McGraw-Hill, Singapore, 1989.

[19] Hill, P., and Zhang, D. The effects of swirl and tumble on combustion in spark-ignition engines. *Progress in energy and combustion science 20*, 1 (1994), 373–429.

[20] Hjelmfelt Jr, A. T., and Mockros, L. F. Motion of discrete particles in a turbulent fluid. *Applied scientific research 16*, 1 (1966), 149–161.

[21] Holmes, P., Lumley, J. L., and Berkooz, G. *Turbulence, Coherent Structures, Dynamical Systems and Symmetry*. Cambridge University Press, 1998.

[22] Horlock, J., and Winterbone, D. *The Thermodynamics and Gas Dynamics of Internal Combustion Engines Volume 2*. Clarendon Press, Oxford, 1986.

[23] Huang, H., Dabiri, D., and Gharib, M. On errors of digital particle image velocimetry. *Measurement Science and Technology 8*, 14 (1997), 1427–1440.

[24] Kähler, C. J., Sammler, B., and Kompenhans, J. Generation and control of tracer particles for optical flow investigations in air. *Experiments in fluids 33*, 6 (2002), 736–742.

[25] Kim, K. I., and Lee, C. H. Development of a new swirl-measurement method for an engine cylinder head by automating the swirl-measuring process. *Proceedings of the Institution of Mechanical Engineers, Part D: Journal of Automobile Engineering 223*, 375 (2009).

[26] Kucejko, B. Oil seeding apparatus for PIV and LDA method measurement. Report, Eindhoven University of Technology, June 2004.

[27] Ladommatos, N., Abdelhalim, S., and Zhao, H. The effects of exhaust gas recirculation on diesel combustion and emissions. *International Journal of Engine Research 1*, 1 (2000), 107–126.

[28] Ladommatos, N., Balian, R. A., and Stone, R. Analysis of swirl in unsteady flow and its effect on diesel combustion. *SAE Technical Paper Series*, 921643 (1992).

[29] Lee, J.-W., Kang, K.-Y., Choi, S.-H., Jeon, C.-H., and Chang, Y.-J. Flow characteristics and influence of swirl flow interactions on spray for direct injection diesel engine. *FISITA World Automotive Congress*, F2000A097 (June 2000).

[30] Li, Y., ZHao, H., Peng, Z., and Ladommatos, N. Analysis of tumble and swirl motions in a four-valve si engine. *SAE Technical Paper Series*, 2001-01-3555 (2001).

[31] Liou, T.-M., and Santavicca, D. A. Cycle resolved turbulence measurements in a ported engine with and without swirl. *SAE Technical Paper Series*, 830419 (1983).

[32] Lumley, J. L. *Engines: An introduction.* Cambridge University Press, 1999.

[33] Meijden, T. J. v. d. Crank angle resolved flow field characterization of a heavy-duty one-cylinder optical engine. Graduation report, Eindhoven University of Technology, March 2009.

[34] Partington, G. Analysis of steady flow tests on inlet and exhaust ports. *Ricardo Consulting Engineers*, Report DP 80/1123 (1980).

[35] Physorg.com. Researchers work toward spark-free, fuel-efficient engines. http://www.physorg.com/news104432768.html, July 2007.

[36] PIVTec. Pivview version 2.1 user manual. http://www.pivtec.com, 2001.

[37] Quantel. http://www.quantel.fr/en/.

[38] Raffel, M., Willert, C., Wereley, S., and Kompenhans, J. *Particle Image Velocimetry, A Practical Guide.* Springer, Berlin Heidelberg, 2007.

[39] Shuliang, L., Yufeng, L., Zhenzhong, X., Lihong, R., Haodong, X., Jie, S., and Songfang, Z. An investigation of the effects of manufacturing deviations of helical inlet port on the flow characteristics of dl diesel engines. *SAE Technical Paper Series*, 2001-01-3507 (2001).

[40] Sigma-Aldrich. Silicon oil 100 cst. http://www.sigmaaldrich.com.

[41] Sirovich, L. Turbulence and the dynamics of coherent structures. part i: Coherent structures. *Quartely of Applied Mathematics 45*, 3 (October 1987), 562–571.

[42] Stahlhofena, W., Gebharta, J., and Rotha, C. Generation and properties of a condensation aerosol of di-2-ethylhexylsebacate (desiii: Experimental investigations into the process of aerosol formation. *Journal of aerosol sience 7*, 3 (1976), 223–231.

[43] Stanislas, M., Okamoto, K., Kähler, C. J., and Westerweel, J. Main results of the second international piv challenge. *Experiments in Fluids 39*, 2 (2010), 170–191.

[44] Tabaczynski, R. J. Turbulence and tubulent combustion in spark-ignition engines. *Progress in energy and combustion science 2*, 3 (1976), 143–165.

[45] Tippelmann, G. A new method of investigation of swirl ports. *SAE Technical Paper Series*. 77040 (1977).

[46] Uzkan, T., Borgnakke, C., and Morel, T. Characterization of flow produced by a high-swirl inlet port. *SAE Technical Paper Series*. 830266 (1983).

[47] van Steenhoven, A. A., and Speetjens, M. F. M. *Syllabus Physical Measurement Methods (4P580)*. Eindhoven University of Technology. 2008.

[48] Weclas, M., Melling, A., and Durst, F. Flow separation in the inlet valve gap of piston engines. *Progress in energy and combustion science 24*. 3 (1998), 165–195.

[49] Westerweel, J. Fundamentals of digital particle image velocimetry. *Measurement Science and Technology 8*. 12 (1997), 1379–1392.

[50] Westerweel, J., and Scarano, F. Universal outlier detection for piv data. *Experiments in Fluids 39*. 6 (2005), 1096–1100.

[51] Xu, H. Some critical technical issues on the steady flow testing of cylinder heads. *SAE Technical Paper Series*. 2001-01-1308 (2001).

Appendix A

List of symbols

Table A.1: List of symbols

Symbol)	**Description**	**Unit**
Γ	Circulation	$\left[\frac{m^3}{s}\right]$
A	Flow area	$[m^2]$
A_P	Valve curtain	$[m^2]$
A_V	Reference surface	$[m^2]$
B	Cylinder-bore	[m]
C	Coefficient	[-]
C	Stokes resistance	$\left[\frac{1}{s}\right]$
C_D	Discharge coefficient	[-]
C_f	Flow coefficient	[-]
D	Inner-seat Diameter	[m]
$\vec{F}_c$	Centripetal force	[N]
$\vec{F}_g$	Gravitational force	[N]
$\vec{F}_y$	Lift force	[N]
$\vec{F}_w$	Frictional force	[N]
$\vec{g}$	Gravitational acceleration	$\left[\frac{m^2}{s}\right]$
I	Intensity	[-]
$\dot{\text{I}}$	Flow momentum torque	[Nm]
J	Angular momentum	$\left[\frac{m^2 \cdot kg}{s}\right]$
L	Valve-lift	[m]
L_V	Minimum geometric surface	[m]
M	Magnification	[-]
N_{sr}	Rig swirl number	[-]
P	Pressure	[Pa]
R	Gas constant (8.3144621)	$[\frac{J}{mol \cdot K}]$
R_x	Autocorrelation coefficient	[-]
R_t	Autocorrelation coefficient time	[-]
Re	Reynolds-number	[-]

Continued on next page

Table A.1 – continued from previous page

Symbol	Description	Unit
R_S	Engine swirl ratio	[-]
R_{SR}	Ricardo Swirl Ratio	[-]
S_k	Stokes number	[-]
T	Temperature	$[^\circ C]$
U	Instantaneous velocity	$[\frac{m}{s}]$
$\bar{U}$	Average velocity	$[\frac{m}{s}]$
$\vec{U}_g$	Gravitational induced velocity	$[\frac{m}{s}]$
$\vec{U}_p$	force	[N]
$\vec{U}_s$	Frictional force	[N]
V	Speed	$[\frac{m}{s}]$
V_{tan}	Tangential speed	$[\frac{m}{s}]$
$\alpha 1$	Inlet valve Open crank angle	$[^\circ]$
$\alpha 2$	Inlet valve close crank angle	$[^\circ]$
Δp	Pressure difference	[Pa]
γ	Ratio of specific heats	[-]
η	Kolmogorov length scale	$[\frac{m^2}{s^3}]$
ϵ	Turbulence disipation	$[\frac{m^2}{s^3}]$
ρ	Density	$[\frac{kg}{m^3}]$
λ	Wavelength	[m]
μ	Dynamic viscosity	$[Pa \cdot s]$
ν	Kinematic viscosity	$[\frac{m^2}{s}]$
ω	Rotational speed	$[\frac{rad}{s}]$
ψ	Valve seat angle	$[^\circ]$
τ_s	Relaxing time	[s]
d	Valve-stem diameter	[m]
d_p	Particle diameter	[m]
l	length scale	[m]
l_t	Turbulence time scale	[s]
$\dot{m}$	Mass flow	$[\frac{kg}{s}]$
n	Number of valves	[-]
r	Radius	[m]
u	Fluctuating velocity	$[\frac{m}{s}]$
Suffices	**Description**	
τ	Particle image	
c	Cylinder	
d	Inner-seat	
dif	diffraction	
diff	Diffusion	
D	Discharge	
F	Flow	
f	Fluid	

Continued on next page

Table A.1 – continued from previous page

Symbol	Description	Unit
in	intake	
o	Incident light	
p	Particle	
ref	Atmospheric	
s	Scattering	
th	Theoretic	
v	Valve	

Appendix B

M-file

```
1 %% Created by Pim Verdaasdonk
2 % This file will covert .dat ASCII files created into .mat files
      for easy
3 % processing by matlab.
4 % % create matrix will all fluctuating velocity components for each
       snapshot in a column
5 % Uf = speedvectors in x-direction
6 % Vf = speedvectors in y-direction
7 % X  = x-position
8 % Y  = Y-position
9 %% Defenitions
10 clear all; clc; close all;
11 DELIMITER = ' ';
12 %HEADERLINES  = input('How many headerlines are in the file?: '); %
       HEADERLINES are the lines of text above the data in the .dat
      files
13 HEADERLINES = 10;
14 %vectors  = input('How many vectors are in the file?: '); % The %
      amount of vectors depends on the interrogation window used.
15 vectors = 3600;
16 massflow1 = input('What is the massflow in [g/s]?: ');      % This
      is the massflow during the experiments,
17 massflow = massflow1/1000
18 Kleplift1 = input('What is the valvelift in [mm]?: ');      %
      Valvelift is used to indentify the data and for calculations
19 %Kleplift1 = 1;
20 Kleplift = Kleplift1/1000
21 Afstand = input('What is the distance in [mm]?: ');         %
      Distance is used for indentification of the data
22 %scale = input('What is the scale used for plotting?: '); % Scales
       the vectors in quiver plots.
23 deltaP1 = input('What is the pressure difference [kPa]?: ');
24 DeltaP = deltaP1*1000
```

```
25 scale = 2;
26 %% determination of constants
27 pos = sqrt(vectors);                          % Number of M in the MxM
       matrix
28 rcil = 65;                                    % Radius of the cylinder
29 B =0.130;                                     % Bore of cylinder
30 Pamb = 102358;                                % ambient pressure in Pa
31 Tamb = 273.15;                                % absolute temperature
32 T = 20;                                       % measurement temperature
33 R = 287.04                                    % Gasconstant
34 %% Load vector files in .dat format
35 [load_filename,load_filepath]=uigetfile('*.dat','Choose file to
       convert...', 'MultiSelect', 'on', ['D:\AFSTUDEREN\tangentiaal\',
       num2str(Kleplift1),'mm\',num2str(Afstand),'mm\DAT']); %'D:\
       afstuderen\dat is the startpath were the dat files are.
36 if (isequal(load_filename,0))
37     return;                                   %cancel selected
38 else
39 filenumbers=numel(load_filename);  %calculates how many .dat files
       will be loaded
40 end
41 i=1;
42 path;
43 %% allocation
44
45 XYUV = zeros(vectors,6);                       % allocates a matrix in
       which the data will be located.
46 Uf   = zeros(vectors,filenumbers);             % allocates the U vectors
47 Vf   = zeros(vectors,filenumbers);             % allocates the V vectors
48 Vort = zeros(vectors,filenumbers);             % allocates the vorticity
        vectors
49 Flag = zeros(vectors,filenumbers);            % allocates the Flag
       vectors
50 %%
51 k2 = 0;
52 Uu = 0;
53 Vv = 0;
54 %% loading the .dat files
55 for i = 1:filenumbers                          %loop over the .dat
       files
56     filename=load_filename(i);
57     filename2=char(filename);
58     fname=fullfile(load_filepath,filename2);
59     newdata=importdata(fname, DELIMITER, HEADERLINES);    %
           retrieves the data from the .dat file
60     vars = fieldnames(newdata);
61     load('vars.mat')
```

```
62      for j = 1:length(vars)
63          assignin('base', vars{j}, newdata.(vars{j}));
64      end
65      XYUV=data;                          % assigns the data to XYUV
66      for k = 1:vectors                   % loop over the vectors in the
            file
67              Uf(k,i) = XYUV(k,3);        % retrieves the U vector and
                    posts it in the Uf vector
68              Vf(k,i) = XYUV(k,4);        % retrieves the V vector and
                    posts it in the Vf vector
69              Flag2(k,i) = XYUV(k,5);     % retrieves the Flag vector
                    and posts it in the Flag vector
70              Vort(k,i) = XYUV(k,7);      % retrieves the Vort vector
                    and posts it in the Vort vector
71              %i
72      end
73 end
74 Flag = Flag2 == 3;          % Finds all the 3's in the flag vector, 3
       marks "valid data" and returns a 0 1 matrix, all the 3's are
       marks 1 the rest is marked zeros
75 Flag1 = Flag2 == 0;         % Returns a matrix containing 1 on all 0
       elements in the .dat file 0 represents nodata and therefore
       contains point outside the mask
76 Flag3 = Flag2 == 5;         % account for interpolated vectors
77 Flag  = Flag+Flag3;         % Build a matrix of valid data and
       interpolated data
78 Mask = sum(Flag1);          % Sums all the vectors lost through the
       mask per measurement
79 Lost_Vec = min(Mask);       % Calculates the minimum number of lost
       vectors per measurement, is used for vertifing the measurements
80 U = Flag.*Uf;               % Returns the Valid U vectors
81 V = Flag.*Vf;               % Returns the valid V vectors
82 Vorticity = Flag.*Vort;     % Returns the valid Voricity vectors
83 X = XYUV(:,1);              % Extracts the X- positions from the last
       .dat file (note that all x- positions are similar for one
       experiment)
84 Y = XYUV(:,2);              % Extracts the Y- positions from the last
       .dat file (note that all x- positions are similar for one
       experiment)
85
86 %% Processing the data
87
88 % Calculating the mean velocities for plotting
89 U_mean      = sum(U,2)./sum((U~=0),2);      % calculates the mean
       velocity in U, leaves out the 0 elements to get an accurate
       average
```

```
90 V_mean     = sum(V,2)./sum((V~=0),2);      % Calculates the mean
       velocity in V, leaves out the 0 elements to get an accurate
       average
91
92 U_velo = U_mean(~isnan(U_mean));           % trowing out the NaN
       terms in U
93 V_velo = V_mean(~isnan(V_mean));           % trowing out the NaN
       terms in V
94
95 U_velo = sum(abs(U_velo))./sum(U_velo ~= 0);    % determining the
       mean velocity in U
96 V_velo = sum(abs(V_velo))./sum(V_velo ~= 0);    % determining the
       mean velocity in V
97
98 % Calculating the mean velocities for further evaluation
99 U_mean(isnan(U_mean)) = 0;                  % removing the NaN terms
       for further evaluation
100 V_mean(isnan(V_mean)) = 0;                 % removing the NaN terms
       for further evaluation
101 U_mean = U_mean*ones(1,filenumbers);       % provides a matrix with
       the mean value of U on all the data file positions
102 V_mean = V_mean*ones(1,filenumbers);       % provides a matrix with
       the mean value of V on all the data file positions
103
104 %% determining magnitude of vectors and SVD
105 MAG = sqrt((U.^2)+(V.^2));
106 StD = std(std(MAG));
107
108
109 % searching for best measurement for Reynolds decomposition for
       plotting
110 Flag_measurement = sum(Flag,1);      % sums the Flags, returns a
       vector of the number of .dat files with the accumulated flags,
       the higher the number the better the measurement
111 Re = max(Flag_measurement);          % finds the maximum number of
       Flags
112 Rd = find(Re == Flag_measurement);   % finds the best measurements
113 Rd = Rd(1,1);                        % selects the first measurement
        of all best measurements
114 U_reynolds = (U(:,Rd)-U_mean(:,1)); % Creates a reynolds
       decomposition for the U vectors, takes the first row of the
       total U_mean matrix
115 V_reynolds = (V(:,Rd)-V_mean(:,1)); % Creates a reynolds
       decomposition for the V vectors, takes the first row of the
       total V_mean matrix
116
117 % squaring the velocities
```

```
118 U2        = U.*U;                    % squares the U velocity
119 V2        = V.*V;                    % squares the V velocity
120 U_mean2 = U_mean.*U_mean;            % squares the mean U velocity
121 V_mean2 = V_mean.*V_mean;            % squares the mean V velocity
122
123
124 %% Vertifing middle location
125
126
127 % resetting middle point
128 U_trim = find(U_mean(:,1) > 0);          % finding positive U-
        vectors
129 X_trim = X(U_trim);                      % trimming X to pos U
        vectors
130 Y_trim = Y(U_trim);                      % trimming Y to pos U-
        vectors
131 shiftY = ((max(Y_trim)+min(Y_trim))/2); % determining new Y
        middlepoint
132 shiftX = ((max(X_trim)+min(X_trim))/2); % determining new X
        middlepoint
133 X = X-shiftX;                           % Shifting X to new
        middlepoint
134 Y = Y-shiftY;                           % Shifting Y to new
        middlepoint
135
136 %%towards vector coordinates
137
138 [theta,r] = CART2POL(X,Y);              % X and Y to polarcoordinates
139 [V_theta,V_r] = CART2POL(U,V);          % U and V to polarcoordinates
140 r       = sqrt((X.^2)+(Y.^2));          % determination of cylinder
        coordinate r in mm
141 r = r./1000;                           % radius r in meters
142 r2      = r*ones(1,filenumbers);        % 3600 x 500 matrix of r.
143 omega = ((abs(V_r).*sin(V_theta))./(abs(r2)));      % determination
        of angular velocity omega
144 omega(isnan(omega)) = 0;                             % replacing nan
        elements by 0 elements
145 V_omega_mean = sum(omega,2)./sum((omega~=0),2);     % calculates the
         mean velocity in omega, leaves out the 0 elements to get an
        accurate average
146 V_omega_mean(isnan(V_omega_mean)) = 0;               % trowing out
        the NaN terms in theta
147 V_omega_total  = sum(abs(V_omega_mean))./sum(V_omega_mean ~= 0)  %
        determining the mean velocity in omega
148
149 % fluctuaties in angular velocity
150
```

```
151 V_omega_mean_tot = V_omega_mean*ones(1,filenumbers); % stretching
    Omega mean
152 V_omega_fluc      = omega - V_omega_mean_tot;          % calculate
    omega fluctuations
153 Fluctan           = abs(sum(V_omega_fluc,2)./sum((V_omega_fluc~=0)
    ,2)); % find mean fluctuations
154
155 Vth = V_r.*cos(V_theta)-V_r.*sin(V_theta);    % Tangential velocity
156 Vr  = V_r.*cos(V_theta)+V_r.*sin(V_theta);    % Radial velocity
157
158 Vth_mean     = sum(Vth,2)./sum((Vth~=0),2);    % calculates the mean
    velocity in Vth, leaves out the 0 elements to get an accurate
    average
159 Vr_mean     =  sum(Vr,2)./sum((Vr~=0),2);     % Calculates the mean
    velocity in Vr, leaves out the 0 elements to get an accurate
    average
160
161 Vth_velo = Vth_mean(~isnan(Vth_mean));        % trowing out the NaN
    terms in Vth
162 Vr_velo = Vr_mean(~isnan(Vr_mean));           % trowing out the NaN
    terms in Vr
163
164 Vth_velo = sum(abs(Vth_velo))./sum(Vth_velo ~= 0); % determining
    the mean velocity in Vth
165 Vr_velo = sum(abs(Vr_velo))./sum(Vr_velo ~= 0);    % determining
    the mean velocity in Vr
166
167
168
169
170 %% calculating different properties
171
172 %% Calculating Turbulence
173 Turb_step1 = ((sqrt(U2+V2)-sqrt(U_mean2+V_mean2)).^2);          %
    intermediate step to determine the turbulence, made for the sake
     of reproducability
174 Turb_measurement = sqrt(sum(Turb_step1)./sum(Turb_step1~=0)); %
    calculates the average turbulence per measurements
175 Turb = sum(Turb_measurement)/sum(Turb_measurement~=0);        %
    calculates the overal turbulence of the total measurement
176
177 %% calculating Turbulence intensities
178
179 Turb_ins_step1 = sqrt((sum((U-U_mean).^2))./sum(((U-U_mean).^2)~=0)
    );      % intermediate step to determine tue u component of the
    turbulence intensities
```

```
180 Turb_ins_step2 = sqrt((sum((V-V_mean).^2))./sum(((V-V_mean).^2)~=0)
    ); ;    % intermediate step to determine the v component of the
    turbulence intensities
181 Turb_ins_measurement = sqrt(((Turb_ins_step1).^2)+((Turb_ins_step2)
    .^2)); % further completing the turbulence intensity
    measurement
182 Turb_ins = sum(Turb_ins_measurement)./sum(Turb_ins_measurement~=0);
            % calculates the overal turbulence intensity of the
    total measurement
183
184 clear Turb_ins_step1 Turb_ins_step2 Turb_ins_measurement
                    % saves memory
185
186 %% calculating Turbulent kinetic energy
187
188 TKE_step1 = (U-U_mean).^2;              %intermediate step in
    calculation turbulent kinetic energy
189 TKE_step2 = (V-V_mean).^2;              %intermediate step in
    calculation turbulent kinetic energy
190 TKE_step3 = (0.5*(TKE_step1+TKE_step2));
191 TKE1 = sum(TKE_step3)./sum(TKE_step3 ~=0);%calculation of turbulent
     kinetic energy
192 TKE= mean(TKE1);
193
194 clear TKE_step1 TKE_step2 TKE_step3 TKE1 % saves memory
195
196
197 %% calculatating Fluctuations
198
199 FL_U = abs(U-U_mean);                   % matrix fluctuations U
200 FL_V = abs(V-V_mean);                   % matrix fluctuations V
201 FL_TOT = sqrt((FL_U.^2)+(FL_V.^2));  % Total fluctuations
202
203 FLUCx = sum(FL_U.1)./sum((FL_U~=0).1); % calculating mean vector
    fluc X
204 FLUCy = sum(FL_V.1)./sum((FL_V~=0).1); % calculating mean vector
    fluc Y
205
206 TOT_FLUC_X = sum(FLUCx)./sum(FLUCx ~=0); % calculating mean fluc X
207 TOT_FLUC_Y = sum(FLUCy)./sum(FLUCx ~=0); % calculating mean fluc Y
208
209 %% Calculating Swirl
210
211 % ideal gaslaw
212 rho=((Pamb+DeltaP)*1000)/(R*(T+Tamb));
213 % steps to determine swirl
214 volflow = massflow/rho;       % volumeflow
```

```
215 vax = volflow/(pi*rcil^2);  % axial velocity
216 step1_swk = r.^2;            % r squared
217 step2_swk = step1_swk*ones(1,filenumbers);  % matrix of r squared
218 step3_swk = step2_swk.*Vth;                 % Vth times R squared
219 swk=rho.*vax.*step3_swk;                    % swirl calculation
220 clear step1_swk step2_swk step3_swk        % saves maemory
221
222 V_theoretic = sqrt((2*DeltaP)/(rho));       % calculation of
        V_theoretic
223 Nsr = (8*swk)/(massflow*V_theoretic*B);     % calculation of Swirl
        Rig number
224
225 %% Saving known DATA
226 evalin('base',['save DATA_',num2str(Kleplift1),'_',num2str(Afstand)
        ]); %saves the DATA to .mat
227
228 %% analyse measurement
229 X_vec = XYUV([1:pos],1);              %gives a x-vector for surfplot
230 Y_vec = XYUV([1:pos:vectors],2);      %gives a y-vector for surfplot
231 Z = sum(Flag,2);                      %sums flag over 3600 vectors
232
233
234 Zm= [];
235 for p = 1 : pos
236     Zm(:,p)=Z(pos*(p-1)+1:pos*p);          % builds a surface of
        flags
237 end
238
239 Zm2 = Zm';                  % translates Zm
240 NAN = find (Zm2==0);        % finds NaN terms
241 Zm2(NAN) = NaN;             % removes Nan terms
242 Zm3 = (Zm2./(filenumbers)*100); % calculates percentage of valid
        vectors
243
244
245 %% Trim data for plotting
246 U_mean_plot = U_mean(:,1);  % gives the average U vectors for
        plotting
247 V_mean_plot = V_mean(:,1);  % gives the average V vectors for
        plotting
248 U_ins = U(:,Rd);            % gives the instantanious U vectors
249 V_ins = V(:,Rd);            % gives the instantanious V vectors
250
251
252 %trim data to cylinder conditions
253 cyl_trim = find(sqrt((X.^2)+(Y.^2)) < rcil);
254 X_plot = X(cyl_trim);
```

```
255 Y_plot = Y(cyl_trim);
256 U_mean_plot = U_mean_plot(cyl_trim);
257 V_mean_plot = V_mean_plot(cyl_trim);
258 U_ins = U_ins(cyl_trim);
259 V_ins = V_ins(cyl_trim);
260 U_reynolds_plot = U_reynolds(cyl_trim);
261 V_reynolds_plot = V_reynolds(cyl_trim);
262
263 swk =swk(cyl_trim);
264 Swk=1000*sum(sum(swk)) %[Nmm]
265 V_omega_total
266
267 %% single value decomposition
268 [U1,S,V1]=svd(Velocity,0);                    % Economy size
269 R=(Velocity'*Velocity);                       % Autocovariance matrix ns
      *ns dimension
270 [eV,D]=eig(R);                                % solve: eV is
      eigenvectors, D is eigenvalues in diagonal matrix
271 [L,I]=sort(diag(D));                          % sort eigenvalues in
      ascending order - I is sorted index vector
272 eValue=zeros(1,filenumbers);
273 eVec=zeros(filenumbers,filenumbers);
274 for o=1:length(D)
275     eValue(length(D)+1-o)=L(o);               % Eigenvalues sorted in
          descending order
276     eVec(:,length(D)+1-o)=eV(:,I(o));         % Eigenvectors sorted in
          the same order
277 end;
278 eValue(length(eValue))=0;                     % last eigenvalue should
      be zero
279 menergy=eValue/sum(eValue);                   % relative energy
      associated with mode m
280 tmp=zeros(vectors*2,filenumbers);
281 normtmp=zeros(vectors*2,filenumbers);
282 phi=zeros(vectors*2,filenumbers);
283 for i=1:length(D) % for i=1:10
284     tmp(:,i)=Velocity*eVec(:,i);  % find mode
285     normtmp(:,i)=norm(tmp(:,i));
286     phi(:,i)=tmp(:,i)/norm(tmp(:,i)); % normalize mode
287 end;
288 snapshotfield=Rd;
289 Mmodenumber=input('Cutoff Mode number M]: ');
290 Nmodenumber=input('Cutoff Mode number N]: ');
291 phimean=phi(:,1:Mmodenumber);
292 phicoherent=phi(:,Mmodenumber:Nmodenumber);
293 aall=Velocity(:,snapshotfield)'*phi; %column of POD coeff (a) for
      one instantaneous velocity field
```

```
294 aallsvd=Velocity(:,snapshotfield)'*U1;
295 save PODcoeff_onesnapshot aallsvd
296 aall2=Velocity'*phi;% MxM matrix containing all POD coeff(all
      mesurements)
297 aall3=aall2.^2;
298 aall4=mean(aall3);
299 aall5=aall4./sum(aall4);
300 save PODcoeff_allsnapshot aall2
301 amean=Velocity(:,snapshotfield)'*phimean;
302 acoherent=Velocity(:,snapshotfield)'*phicoherent;
303 u=zeros(vectors*2,length(aall));
304 for   i=1:length(aall)
305       u(:,i)=aall(i)*phi(:,i); % 7688 vectoren x 50 modes
306 end
307 sizeu=size(u);
308 modes=sizeu(2);
309 uall=sum(u,2);
310 %% Calculation of the "mean" part of the POD as defined by choosing
      M
311 for   i=1:length(amean)
312       u(:,i)=amean(i)*phimean(:,i); %
313 end
314 umean=sum(u,2);
315
316 %% Singular values from SVD
317 Singular1=diag(S); % Singular values from SVD
318
319 % Plotting
320
321  figure(1)
322  mag_ins = sqrt((U_ins.^2)+(V_ins.^2));  % determines magnitude of
       vectors for plotting
323  circle([-32.87,27.4],44.75/2,1000,'k')  % draws a inlet valve
324  hold on
325  circle([26.67,32.4],44.75/2,1000,'k')   % draws a inlet valve
326  hold on;
327  cx=[-65:1:65];                          % calculation for cylinder
       outline
328  cy=sqrt(65^2-cx.^2);                    % calculation for cylinder
       outline
329  plot(cx,cy,'k');                        % plots cylinder outline
330  plot(cx,-cy,'k');                       % plots cylinder outline
331  hold on
332  quiverc4([X_plot],[Y_plot],[U_ins],[V_ins],scale);hold on   %
       draws the vectors
333  set(gca,'XLim',[-65 65],'YLim',[-65 65]);                   %
       changes the x and y plot range
```

```
334 set(gca,'XTick',[-60:10:60],'YTick',[-60:10:60]);                % sets
        new ticks
335 cbar('yl',[min(mag_ins):round((max(mag_ins)/10)):round(max(mag_ins
    ))],'title','m/s','gap',.7);            % creates the colorbar
336 title(['instantaneous velocity field Valve Lift ',num2str(
    Kleplift1),' Distance ',num2str(Afstand)])     % title of the
    graph
337 ylabel('Y-Position [mm]');
338 xlabel('X-Position [mm]');
339 saveas(gcf,['Instantaneous_field_',num2str(Kleplift1),'_',num2str(
    Afstand)],'pdf');
340 saveas(gcf,['Instantaneous_field_',num2str(Kleplift1),'_',num2str(
    Afstand)],'jpg');
341 %
342 figure(2);
343 surf(X_vec,Y_vec,Zm3);
344 axis equal;
345 hold on;
346 title(['Percentage of reliable vectors per interrogation area
    Valve Lift ',num2str(Kleplift1),' Distance ',num2str(Afstand)])
    ;
347 xlabel('X-Position [mm]');
348 ylabel('Y-Position [mm]');
349 hold on;
350 t = colorbar('peer',gca);
351 set(get(t,'ylabel'),'String', 'righteous vectors [%]');
352 saveas(gcf,['Quality_',num2str(Kleplift1),'_',num2str(Afstand)],'
    pdf');
353 saveas(gcf,['Quality_',num2str(Kleplift1),'_',num2str(Afstand)],'
    jpg');
354
355 figure(3);
356 mag_mean = sqrt((U_mean_plot.^2)+(V_mean_plot.^2));
357 circle([-32.87,27.4],44.75/2,1000,'k');
358 hold on;
359 circle([26.67,32.4],44.75/2,1000,'k');
360 axis equal;
361 hold on;
362 cx=[-65:1:65];
363 cy=sqrt(65^2-cx.^2);
364 plot(cx,cy,'k');
365 plot(cx,-cy,'k');
366 quiverc4([X_plot],[Y_plot],[U_mean_plot],[V_mean_plot],scale);hold
     on;
367 cbar('yl',[round(min(mag_mean)):round((max(mag_mean)/10)):round(
    max(mag_mean))],'title','m/s')
```

```
368 set(gca,'XLim',[-65 65],'YLim',[-65 65]); % changes the x and y
      plot range
369 set(gca,'XTick',[-60:10:60],'YTick',[-60:10:60]); % sets new ticks
370 title(['Average Velocity field. Valve Lift ',num2str(Kleplift1),'
      Distance ',num2str(Afstand)]);
371 ylabel('Y-Position [mm]');
372 xlabel('X-Position [mm]');
373 hold off;
374 saveas(gcf,['Mean_velocity_',num2str(Kleplift1),'_',num2str(
      Afstand)],'pdf');
375 saveas(gcf,['Mean_velocity_',num2str(Kleplift1),'_',num2str(
      Afstand)],'jpg');
376
377 figure(4);
378 mag_rey = sqrt((U_reynolds_plot.^2)+(V_reynolds_plot.^2));
379 circle([-32.87,27.4],44.75/2,1000,'k');
380 hold on;
381 circle([26.67,32.4],44.75/2,1000,'k');
382 axis equal;
383 hold on;
384 cx=[-65:1:65];
385 cy=sqrt(65^2-cx.^2);
386 plot(cx,cy,'k');
387 plot(cx,-cy,'k');
388 quiverc4([X_plot],[Y_plot],[U_reynolds_plot],[V_reynolds_plot],
      scale);hold on;
389 cbar('yl',[min(mag_rey):round((max(mag_rey)/10)):round(max(mag_rey
      ))],'title','m/s');
390 set(gca,'XLim',[-65 65],'YLim',[-65 65]); % changes the x and y
      plot range
391 set(gca,'XTick',[-60:10:60],'YTick',[-60:10:60]); % sets new ticks
392 ylabel('Y-Position [mm]');
393 xlabel('X-Position [mm]');
394 title(['Reynolds decomposition. Valve Lift ',num2str(Kleplift1),'
      Distance ',num2str(Afstand)]);
395 saveas(gcf,['Reynolds decomposition_',num2str(Kleplift1),'_',
      num2str(Afstand)],'pdf');
396 saveas(gcf,['Reynolds decomposition_',num2str(Kleplift1),'_',
      num2str(Afstand)],'jpg');
397
398 %% plottin SVD
399
400 title(['Reconstructed snapshot ' int2str(snapshotfield) ' using all
      modes'])
401 xlabel('X [mm]');
402 ylabel('Y [mm]');
403 saveas(gcf,'Reconstructedsnaps_allmodes','fig');
```

```
saveas(gcf,'Reconstructedsnaps_allmodes','jpg');
saveas(gcf,'Reconstructedsnaps_allmodes','pdf');
print -depsc 'Reconstructedsnaps_allmodes.eps';
SnapshotU=[U(:,Rd);V(:,Rd)];
Energysnapshot=mean(SnapshotU.^2);
% Plot Reconstructed Velocity field - mean flow M=?? %
XY1=reshape(umean,vectors,2);
U1=XY1(:,1);
V1=XY1(:,2);
X1=X;
Y1=Y;
I=find(U1==0); %find all zeros in U1
U1(I)=[];%clear all cvalues on index locations
X1(I)=[];
I=find(V1==0); %find all zeros in U1
V1(I)=[];%clear all cvalues on index locations
Y1(I)=[];
ReconstrmeanU=[U1;V1];
Energyreconstrmeanflow=mean(ReconstrmeanU.^2);
Energypercentage=round((Energysnapshot/Energyreconstrmeanflow)*100)
    ;
figure
quiver(X1,Y1,U1,V1,'LineWidth',1.1);
title(['Reconstructed snapshot ' int2str(snapshotfield) ' using M='
    int2str(Mmodenumber) ' containing ' int2str(Energypercentage) '
    percent of the energy''']);
xlabel('X [mm]');
ylabel('Y [mm]');
saveas(gcf,'Reconstructedsnapshot-meanpart','fig');
saveas(gcf,'Reconstructedsnapshot-meanpart','jpg');
saveas(gcf,'Reconstructedsnapshot-meanpart','pdf');
saveas(gcf,'Reconstructedsnapshot-meanpart','eps');
print -depsc 'Reconstructedsnapshot-meanpart.eps';


% Singlar values as function of POD mode
figure
plot(Singular1,'-k');
xlabel('Mode number');
ylabel('Singular value');
saveas(gcf,'Singularvalues','fig');
saveas(gcf,'Singularvalues','jpg');
saveas(gcf,'Singularvalues','pdf');
saveas(gcf,'Singularvalues','eps');
print -depsc 'Singularvalues.eps';

% POD coefficients as function of POD mode
```

```
448 figure
449 plot(aall,'-k');
450 xlabel('Mode number');
451 ylabel('POD coefficient');
452 saveas(gcf,'PODcoeff','fig');
453 saveas(gcf,'PODcoeff','jpg');
454 saveas(gcf,'PODcoeff','pdf');
455 saveas(gcf,'PODcoeff','eps');
456 print -depsc 'PODcoeff.eps';
457
458 % Plot Normalised Mode 1
459 XY1=reshape(phi(:,1),vectors,2);
460 U1=XY1(:,1).*aall(:,1);
461 V1=XY1(:,2).*aall(:,1);
462 U1 = U1(cyl_trim);
463 V1 = V1(cyl_trim);
464 figure
465 mag1 = sqrt((U1.^2)+(V1.^2));
466 circle([-32.87,27.4],44.75/2,1000,'k')
467 hold on
468 circle([26.67,32.4],44.75/2,1000,'k')
469 hold on;
470 cx=[-65:1:65];
471 cy=sqrt(65^2-cx.^2);
472 plot(cx,cy,'k');
473 plot(cx,-cy,'k');
474 hold on
475 quiverc4(X_plot,Y_plot,U1,V1,scale);
476 set(gca,'XLim',[-65 65],'YLim',[-65 65]); % changes the x and y
      plot range
477 set(gca,'XTick',[-60:10:60],'YTick',[-60:10:60]); % sets new ticks
478 cbar('yl',[min(mag1):round((max(mag1)/10)):round(max(mag1))],'title
      ','m/s','gap',7);
479 title('Normalized mode 1');
480 xlabel('X [mm]');
481 ylabel('Y [mm]');
482 saveas(gcf,'Mode1','fig');
483 saveas(gcf,'Mode1','jpg');
484 saveas(gcf,'Mode1','pdf');
485 saveas(gcf,'Mode1','eps');
486 print -depsc 'Mode1.eps';
487
488 XY1=reshape(phi(:,2),vectors,2);
489 U1=XY1(:,1).*aall(:,2);
490 V1=XY1(:,2).*aall(:,2);
491 U1 = U1(cyl_trim);
492 V1 = V1(cyl_trim);
```

```
493 figure
494 mag1 = sqrt((U1.^2)+(V1.^2));
495 circle([-32.87,27.4],44.75/2,1000,'k')
496 hold on
497 circle([26.67,32.4],44.75/2,1000,'k')
498 hold on;
499 cx=[-65:1:65];
500 cy=sqrt(65^2-cx.^2);
501 plot(cx,cy,'k');
502 plot(cx,-cy,'k');
503 hold on
504 quiverc4(X_plot,Y_plot,U1,V1,scale);
505 set(gca,'XLim',[-65 65],'YLim',[-65 65]); % changes the x and y
      plot range
506 set(gca,'XTick',[-60:10:60],'YTick',[-60:10:60]); % sets new ticks
507 cbar('yl',[min(mag1):round((max(mag1)/10)):round(max(mag1))],'title
      ','m/s','gap',7);
508 title('Normalized mode 2');
509 xlabel('X [mm]');
510 ylabel('Y [mm]');
511 saveas(gcf,'Mode2','fig');
512 saveas(gcf,'Mode2','jpg');
513 saveas(gcf,'Mode2','pdf');
514 saveas(gcf,'Mode2','eps');
515 print -depsc 'Mode2.eps';
516
517 XY1=reshape(phi(:,3).vectors,2);
518 U1=XY1(:,1).*aall(:,3);
519 V1=XY1(:,2).*aall(:,3);
520 U1 = U1(cyl_trim);
521 V1 = V1(cyl_trim);
522 figure
523 mag1 = sqrt((U1.^2)+(V1.^2));
524 circle([-32.87,27.4],44.75/2,1000,'k')
525 hold on
526 circle([26.67,32.4],44.75/2,1000,'k')
527 hold on;
528 cx=[-65:1:65];
529 cy=sqrt(65^2-cx.^2);
530 plot(cx,cy,'k');
531 plot(cx,-cy,'k');
532 hold on
533 quiverc4(X_plot,Y_plot,U1,V1,scale);
534 set(gca,'XLim',[-65 65],'YLim',[-65 65]); % changes the x and y
      plot range
535 set(gca,'XTick',[-60:10:60],'YTick',[-60:10:60]); % sets new ticks
```

```
536 cbar('yl',[min(mag1):round((max(mag1)/10)):round(max(mag1))],'title
      ','m/s','gap',7);
537 title('Normalized mode 3');
538 xlabel('X [mm]');
539 ylabel('Y [mm]');
540 saveas(gcf,'Mode3','fig');
541 saveas(gcf,'Mode3','jpg');
542 saveas(gcf,'Mode3','pdf');
543 saveas(gcf,'Mode1','eps');
544 print -depsc 'Mode3.eps';
545
546 XY1=reshape(phi(:,4),vectors,2);
547 U1=XY1(:,1).*aall(:,4);
548 V1=XY1(:,2).*aall(:,4);
549 U1 = U1(cyl_trim);
550 V1 = V1(cyl_trim);
551 figure
552 mag1 = sqrt((U1.^2)+(V1.^2));
553 circle([-32.87,27.4],44.75/2,1000,'k')
554 hold on
555 circle([26.67,32.4],44.75/2,1000,'k')
556 hold on;
557 cx=[-65:1:65];
558 cy=sqrt(65^2-cx.^2);
559 plot(cx,cy,'k');
560 plot(cx,-cy,'k');
561 hold on
562 quiverc4(X_plot,Y_plot,U1,V1,scale);
563 set(gca,'XLim',[-65 65],'YLim',[-65 65]); % changes the x and y
      plot range
564 set(gca,'XTick',[-60:10:60],'YTick',[-60:10:60]); % sets new ticks
565 cbar('yl',[min(mag1):round((max(mag1)/10)):round(max(mag1))],'title
      ','m/s','gap',7);
566 title('Normalized mode 4');
567 xlabel('X [mm]');
568 ylabel('Y [mm]');
569 saveas(gcf,'Mode4','fig');
570 saveas(gcf,'Mode4','jpg');
571 saveas(gcf,'Mode4','pdf');
572 saveas(gcf,'Mode4','eps');
573 print -depsc 'Mode4.eps';
574
575 % Plot energy and cumulative energy
576 figure
577 plot(menergy);
578 length_e=length(menergy);
579 energy=zeros(length_e);
```

```
energy(1)=menergy(1);
for i=2:length_e % for i=1:4
energy(i)=energy(i-1)+menergy(i);
end;
figure
plot(energy(:,1),'LineWidth',2);
xlabel('mode','FontSize',12);
ylabel('cumulative energy','FontSize',12);
axis([0 filenumbers 0 1.05])
saveas(gcf,'Cumulative_energy','fig');
saveas(gcf,'Cumulative_energy','jpg');
saveas(gcf,'Cumulative_energy','pdf');
saveas(gcf,'Cumulative_energy','eps');
print -depsc 'Cumulative_energy.eps';

%% Postprocessing

cd('D:\AFSTUDEREN\DATA\')
if exist('PIM.mat')
    load PIM.mat
end

valve_range = [1:5];
dist_range = [30:10:160];

i = find(valve_range == Kleplift1);
j = find(dist_range == Afstand);

pim.valve(i).dist(j).Turb = Turb;
pim.valve(i).dist(j).Turb_ins = Turb_ins;
pim.valve(i).dist(j).TKE = TKE;
pim.valve(i).dist(j).FLUCx = TOT_FLUC_X;
pim.valve(i).dist(j).FLUCy = TOT_FLUC_Y;
pim.valve(i).dist(j).U_velo = U_velo;
pim.valve(i).dist(j).V_velo = V_velo;
pim.valve(i).dist(j).Swirl = Swk;
pim.valve(i).dist(j).massflow = massflow;
pim.valve(i).dist(j).V_omega_total = V_omega_total;
pim.valve(i).dist(j).Vth = Vth;
pim.valve(i).dist(j).Vr = Vr;
pim.valve(i).dist(j).Nsr = Nsr;
pim.valve(i).dist(j).V_theoretic = V_theoretic;
pim.valve(i).dist(j).Vth_velo = Vth_velo;
pim.valve(i).dist(j).Vr_velo = Vr_velo;
pim.valve(i).dist(j).StD = StD;


```

```
627 save PIM pim
628
629 cd('D:\AFSTUDEREN')
```

Appendix C

Seeding generation of Laskin nozzles

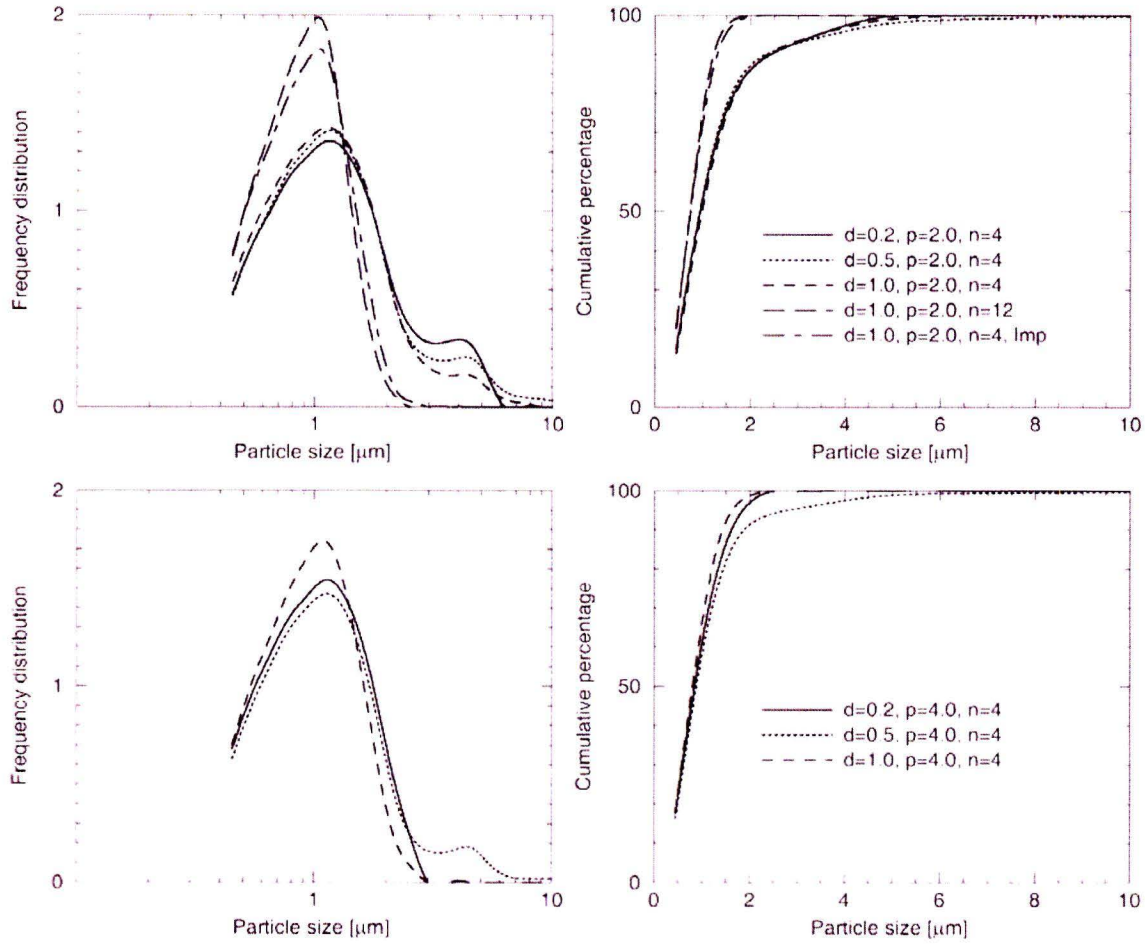

Figure C.1: Volumetric particle size distribution for various hole diameters (d = 0.2, 0.5, 1 mm), pressure (p = 2 and 4 bar), number of holes per nozzle (n = 4 and 12) and impactor plate [24]

Appendix D

Laser specifications

Table D.1: Comparison between Brio Twins and Twins BSL 50 [37]

Model	**Brio Twins**	**Twins BSL 50**
Repetition rate [Hz]	10	15
Wavelength [nm]	532	532
Energy per pulse [mJ]	60	50
Energy stability [shot-to-shot %]	+/- 5	+/- 6
Pulse duration [ns]	~ 4	7
Beam diameter [mm]	~ 4.5	4
Beam divergence [mrad]	< 5	< 7
Pointing stability [μrad]	< 50	< 100
Jitter [ns]	+/- 1	+/- 2

Appendix E

Tangential average velocity fields

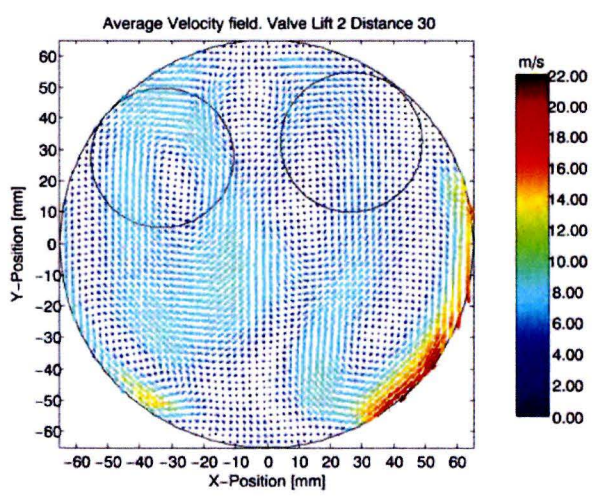

Figure E.1: Average velocity distance 30 [mm]

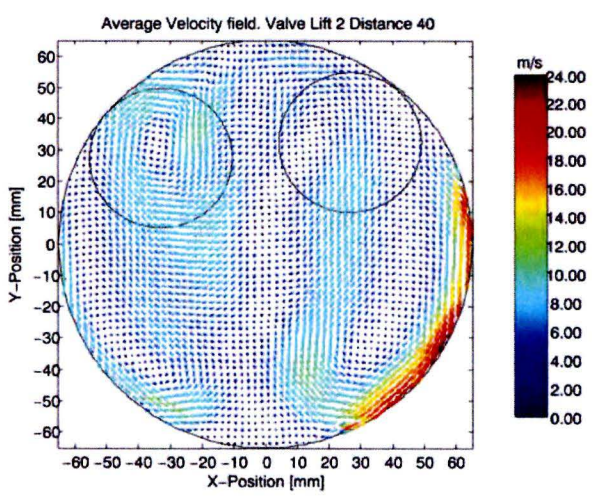

Figure E.2: Average velocity distance 40 [mm]

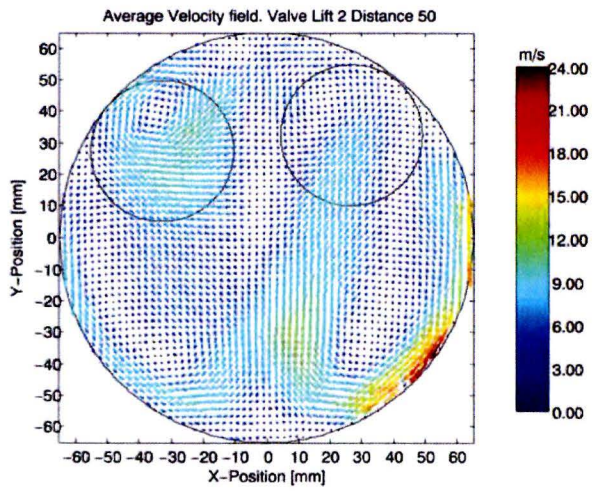

Figure E.3: Average velocity distance 50 [mm]

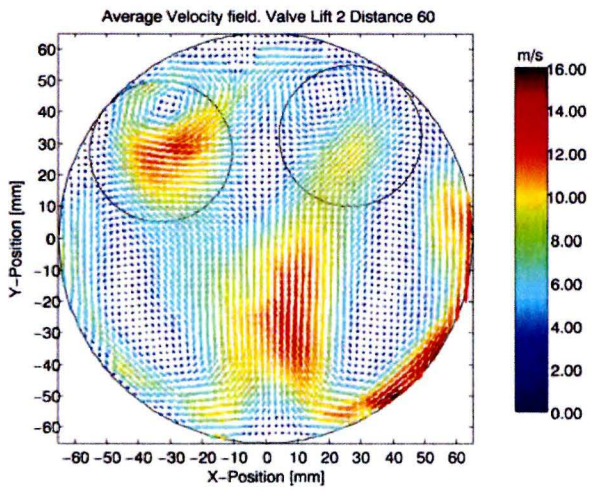

Figure E.4: Average velocity distance 60 [mm]

Valve lift = 2 [mm], Mass-flow = 50.5 $\left[\frac{g}{s}\right]$

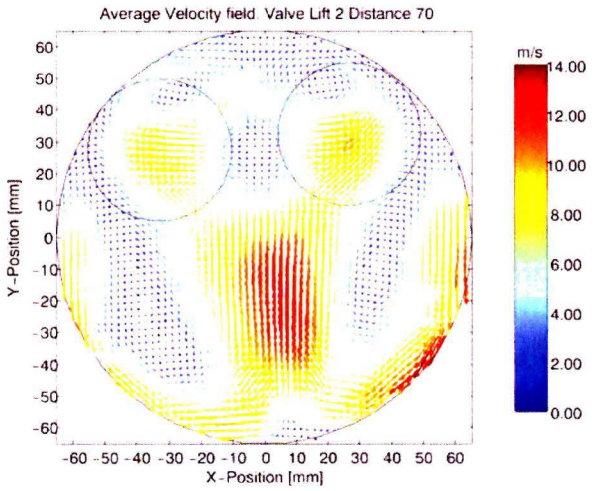

Figure E.5: Average velocity distance 70 [mm]

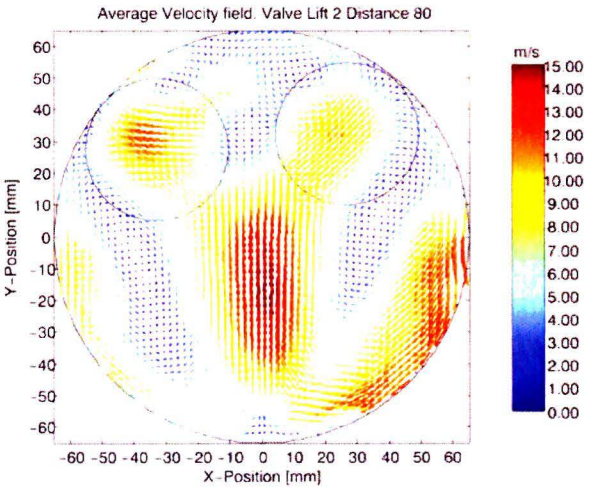

Figure E.6: Average velocity distance 80 [mm]

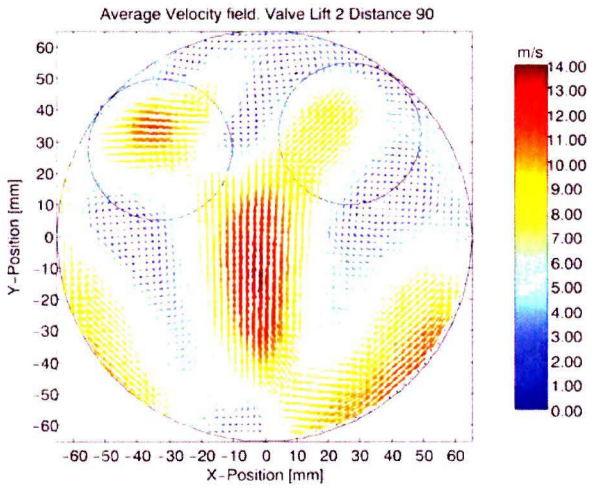

Figure E.7: Average velocity distance 90 [mm]

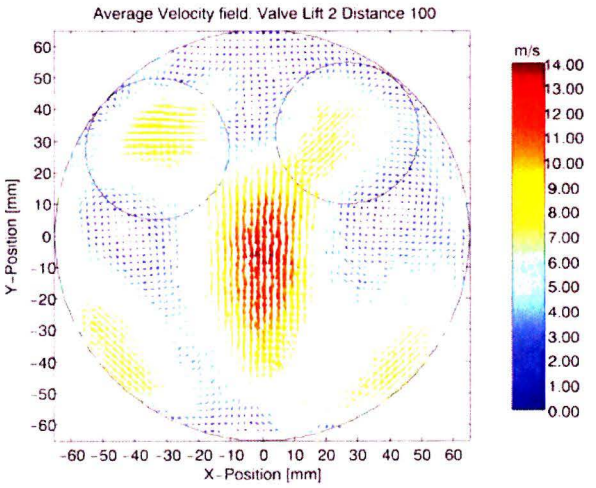

Figure E.8: Average velocity distance 100 [mm]

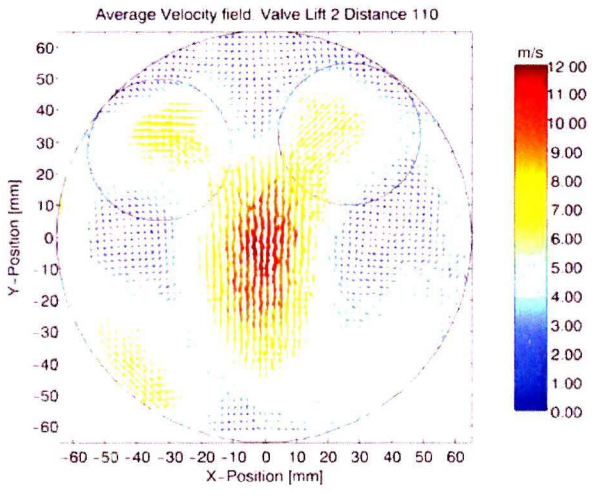

Figure E.9: Average velocity distance 110 [mm]

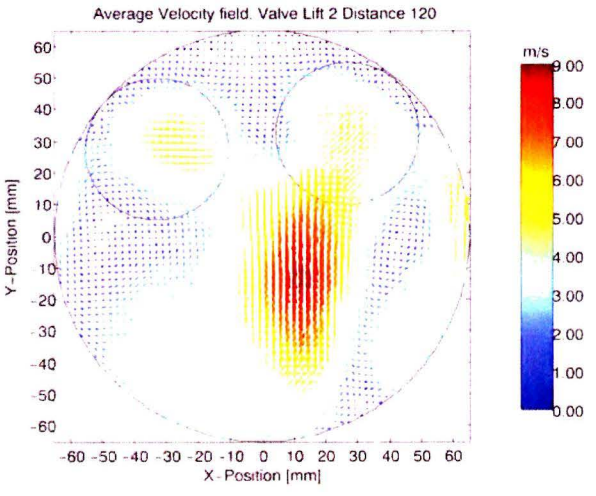

Figure E.10: Average velocity distance 120 [mm]

Valve lift = 2 [mm]. Mass-flow = 50.5 $\left[\frac{g}{s}\right]$

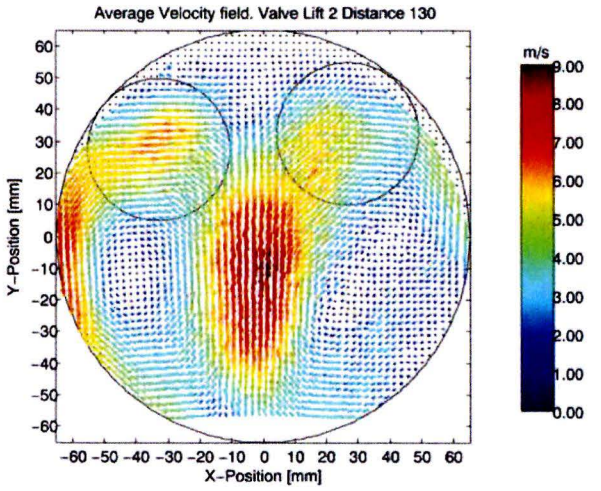

Figure E.11: Average velocity distance 130 [mm]

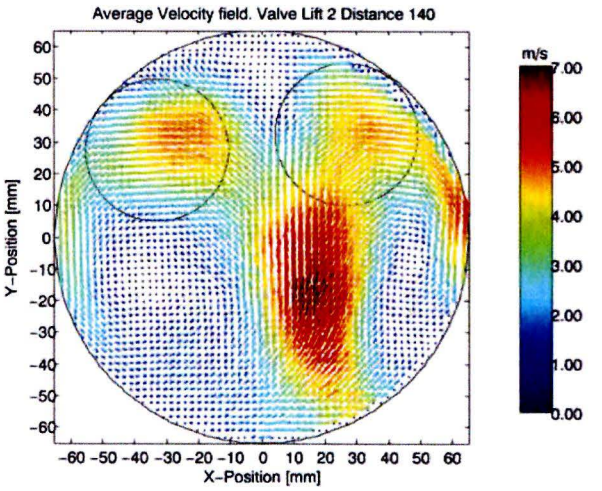

Figure E.12: Average velocity distance 140 [mm]

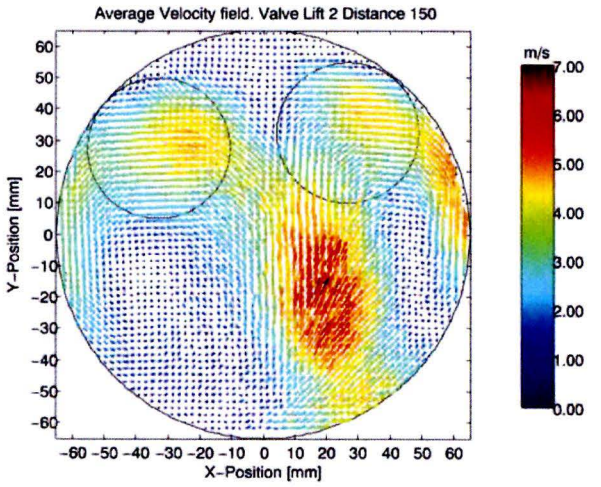

Figure E.13: Average velocity distance 150 [mm]

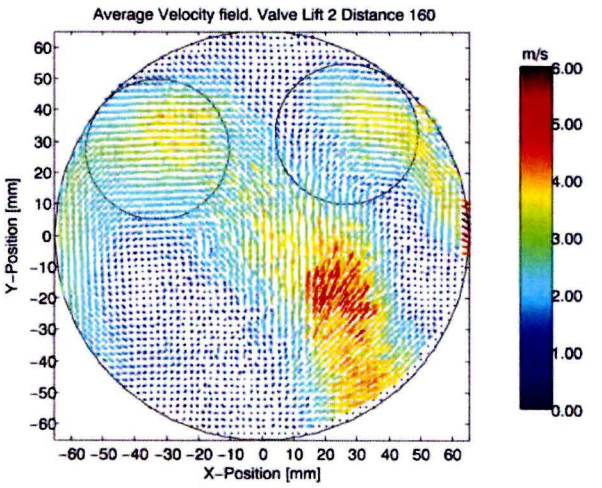

Figure E.14: Average velocity distance 160 [mm]

Valve lift = 2 [mm], Mass-flow = 50.5 $\left[\frac{g}{s}\right]$